POLYMER ARCHITECTURE EFFECTS ON MECHANOCHEMICAL REACTIONS

BY

PRESTON ANDREW MAY

DISSERTATION

Submitted in partial fulfillment of the requirements
for the degree of Doctor of Philosophy in Chemistry
in the Graduate College of the
University of Illinois at Urbana-Champaign, 2013

Urbana, Illinois

Doctoral Committee:

Professor Jeffrey S. Moore, Chair
Professor Scott K. Silverman
Professor Steven C. Zimmerman
Professor Scott R. White

Dissertation Abstract

Long chain polymers have a unique ability to become highly extended in elongational flow fields. The forces developed along the backbone give rise to scission of the chains near their center. Recently, this unique property of polymers has been adopted to explore new chemical transformations by embedding structural elements into the backbone designed to undergo site-specific bond cleavage, termed mechanophores. An overarching theme in polymer mechanochemistry is that the polymer chains are the link between macroscopic energy and the mechanophore. Therefore, polymer architecture is thought to play a significant role in influencing these types of mechanochemical reactions in polymers. This research aims to identity the governing rules of force transduction in polymer chains by studying various polymer architectures.

To achieve this goal, an efficient characterization technique that allows for *in-situ* measurement of solution-based mechanochemical reactivity through coupling of ultrasound experiments and UV-Vis spectroscopy in a flow cell was created. Using this technique we were able to perform rigorous kinetic analyses to screen the effects of multiple parameters on mechanophore activation using spiropyran mechanophores as a model. The effects of flow rate and sonication intensity are provided. Furthermore, we isolated the effects of molecular mass and chain length pertaining to polymer architecture by synthesizing a series of polymers containing chain-centered spiropyran mechanophores; poly(methyl acrylate), poly(ethyl acrylate), poly(*n*-butyl acrylate), poly(*iso*-butyl acrylate) and poly(*tert*-butyl acrylate). Results show that chain length contributes more to activation than molecular mass of the individual chains.

In addition, it was hypothesized that alternative architectures with polymers containing multiple branches and arms could transmit force to mechanophores more efficiently than their linear counterparts. Spiropyran-linked star PMA with four and eight chains were synthesized via single electron transfer living radical polymerization and were screened in the ultrasonication flow cell and in solid-state tensile tests. Experimental data show that polymers with branched architectures activate slower than linear architectures in solution, yet faster in solid-state tensile experiments. These results provide a greater understanding of mechanotransduction processes in polymers and allow us to design increasingly sensitive mechanoresponsive polymers.

Furthermore, heterogenous polymer architecuture was examined by introducing a spiropyran mechanophore at the interface of a glass fiber and PMMA matrix. Interfacial shear forces are applied to the mechanophore by a single fiber microbond testing protocol. Results suggest that covalent attachment as well as frictional force might be able to activate mechanophores at interfaces.

Acknowledgements

Graduate school has been a long road. There are many people I would like to thank for helping me along the way. First, I would like to thank Jeff, my adviser. He has given me a platform and an opportunity to mature as a scientist in his lab. I really appreciate his willingness to help me when I need it with guidance and rigorous questioning and his willingness to let me struggle through research problems when I needed to figure out solutions on my own. I have a lot of respect for the trust he puts in each group member to take control of their projects and make things happen. I have seen a lot of sides of Jeff but what I will remember most and take with me is his relentless attitude to make us think, question, characterize, and analyze scientific problems from all angles. I definitely see the world around me through a different lens after being in Jeff's group for 5 years.

I would also like to thank my thesis committee, Prof. Silverman, Prof. Zimmerman, and Prof. White. It is amazing how just a brief discussion with them can propel me forward with motivation and encouragement. During both my prelim exam and my ORP defense, they challenged me to take hold of my projects and to become a better writer. I tried very hard to improve in both of those areas.

Additionally Prof. Nancy Sottos has given me guidance and focus both directly and indirectly. It has been an incredible learning process to listen to her discuss research problems and take in her viewpoint and apply it to my own thinking about where projects are heading, why we should spend the time on a project, and, especially, how a fundamental chemical reaction could be applied in an engineering context.

I also need to especially thank my undergraduate advisor and mentor, Prof. Michael Mayer at Texas Tech. He taught me organic chemistry at Texas Tech and allowed me to learn basic chemical synthesis in his lab. I'm not sure how my life would have turned out without his encouragement. I never would have applied to a prestigious chemistry department like UIUC without his assurances that I could compete at this level.

I would also like to thank all the Moore group members, past and present, from whom I have learned a great deal. The atmosphere in the group has always been very friendly and open and I could always count on my lab mates to discuss challenges in my research projects and in life in general. I couldn't have made it this far without their encouragement and guidance. Special thanks to Dr. Doug Davis, Dr. Matt Kryger, Dr. Charles Diesendruck, Dr. Brian Steinberg, Dr. Koushik Ghosh, and Dr. Tomohiro Shiraki. These guys helped me tremendously in mechanochemistry research and I will forever consider them friends for life. Thank you to all the Beckman Crew for making the labs and offices at Beckman a place worth working at: Dr. Mary Caruso, Dr. Elizabeth Glogowski, Dr. Aaron Esser-Kahn,

Dr. Susan Odom, Dr. Gerald Wilson (old school BC), Windy Santa Cruz, Hefei Dong, Mike Yang, Catherine Possanza, Yang Song, Andy Li, Ian Robertson, Shijia Tang, Josh Grolman and Dr. Kelly Wiggins (new school BC). The RAL posse: Dr. Phil Janowicz, Dr. Mike Evans, Dr. Aaron Finke, Dr. Josh Ritchey, Nina Sekerak, James Herbison, Scott Sisco, Josh Kaitz, Dr. Bora Inci, Dr. Nag Gavvalapallie, Dr. Pin-Nan Cheng, Yi Ren, Anna Yang, and Marissa Giovino. A special thanks to Dr. Zheng Xue whom I had the pleasure to work with during my undergrad research and during graduate school. Although the AMS group is much too large to list, I need to give a special thanks to Dr. Cassandra Degen, Dr. Brett Beiermann, Dr. Corissa Lee, and Asha-Dee Celestine for their support and ideas to move projects in new directions I would have never thought of. I learned a great deal from and would gladly work with them in the future if the opportunity presented itself. All of the people in the preceding paragraph have directly helped to shape me as a scientist and a person and they are the type of people that I try to model myself after.

I am also grateful to have worked with four undergraduates and a high school student during my time here: Mike Hamoy, Nick Munaretto, Alex Munaretto, Kate Wlodarczyk, and Audrey White. I couldn't have asked for better people to work with. I am really proud of everything they were able to accomplish in and out of the lab.

I would like to personally thank Ashley Trimmel and Erica Malloch. They keep the train on the track. They do so much for all of us that it is almost incomprehensible to not have them associated with the group. I need to thank the tremendous support staff that has helped me along the way: Stacy Olson, Becky Duffield, Susan Lighty, Lori Johnson, and Krista Smith.

My parents, my brother, and my sister are a major reason why I have made it this far in life. Without their encouragement I wouldn't have had the guts to make it this far. I hope I can make them proud.

Finally I would like to thank my wife, Chrissy. She is my best friend and has been with me since my 2nd year in grad school. She has been my biggest supporter and kept me sane throughout the stress of grad school. I'm looking forward to many years with her by my side. I love you.

Table of Contents

Chapter 1 – Introduction*

1.1 Introduction

Although the elemental composition of macromolecules and small molecules are similar, the chain-like character of macromolecules gives them special properties, such as strength, toughness, and elasticity, which can be utilized for light weight, high strength engineering application. Their behavior in flow fields is also unique and in recent years this has been exploited from the standpoint of force-induced reactivity. In 1985 Keller and Odell wrote,[1] "*It appears self evident that the ability to become extended and/or aligned is a reflection of the most intrinsic properties of long chains, possibly more so than some static property. In other words, by taking a random tangle of string we may learn more about it, or at least with greater ease, by trying to disentangle and straighten the string than by investigating it in its tangled form*." This disentangling and straightening, also known as the coil to stretch transition, has been studied for a variety of purposes, most notably in polymer scission. Perhaps more interesting from a mechanochemical standpoint, these studies have evolved over time to selective reactions of individual mechanically sensitive molecules within polymers, called mechanophores.[2-4] This new class of materials has fundamentally changed the landscape of chemical design and intuition by unveiling chemical reaction pathways previously hidden. The roadmap to modern-day polymer mechanochemistry has been aided by the evolution of experimental techniques designed to apply force on polymers and study the behavior of these deformed macromolecules. This tutorial review will highlight accomplishments in the field that have led to our current, yet still incomplete, knowledge of macromolecular mechanochemistry. Additionally, a summary of solution-based techniques used to generate molecular force via elongational flows will be presented. A particular emphasis is placed on acoustic fields generated by ultrasonication which has become the most widely adopted method for screening mechanophore reactivity in solution. While the study of mechanochemical reactions in polymers is not limited to solution-based techniques, these types of experiments often only require milligram quantities of material and can easily be coupled to traditional characterization methods such as solution-based spectroscopy, both *in-situ* and *ex-situ*. Mechanochemical reactions in bulk polymers and single-molecule force spectroscopy are considered outside the scope of this article. However, the interested reader is referred to several reviews that discuss these topics.[2-5]

---

*Material contained within this chapter has previously been published in the following reference:
May, P. A.; Moore, J. S. Chem. Soc. Rev. 2013. DOI:10.1039/C2CS35463B.

1.2 Historical Perspective

Polymer mechanochemistry can be traced back to the 1930's when Staudinger reported the molecular weight reduction of polymers subjected to mastication.[6] Kauzmann and Erying attributed this observation to a mechanical cleavage of covalent bonds within the polymer.[7] Experimentally, this degradation event has been demonstrated many times by various solution-based techniques that create elongational flow fields. Size exclusion chromatography (SEC) has offered very useful insights into the phenomenon of mechanically induced chain scission. Polydisperse polymers have been shown to have a narrowed polydispersity index (PDI) when subjected to elongational flow fields (Figure 1.1).[8] Molecular weight changes cease when the polymers reach a lower molecular weight threshold (M_{lim}), below which no further scission is observed.[8,9] M_{lim} is a unique property that is highly dependent on the experimental conditions and technique used. These types of observations have been attributed to a non-random scission event occurring near the center of the polymer chain since random scission would produce a much wider distribution of products. While it was not directly observed, significant elongation of the polymer chains was believed to be occurring. Collectively, it has been concluded that the process of chain scission is a mechanically activated process and, in fact, is the result of mechanical forces acting on the polymer and being greatest near the middle 15% of the polymer chain.[2]

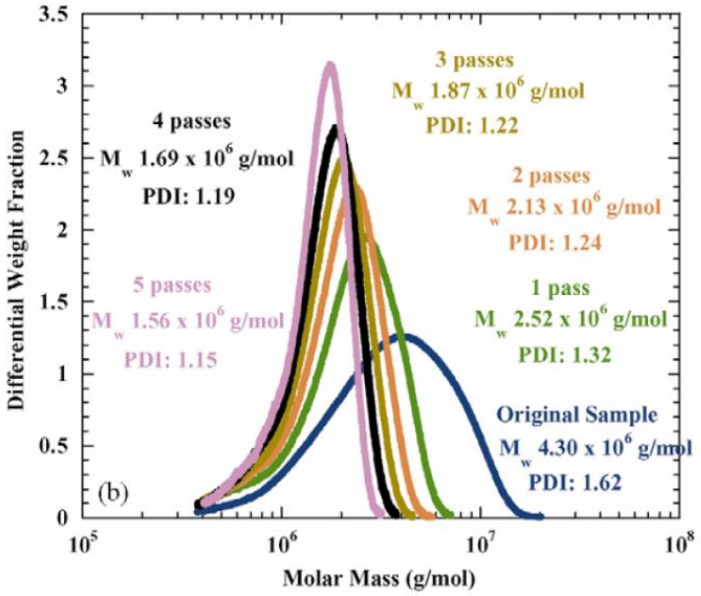

Figure 1.1. Polydimethacrylamide in water subjected to multiple passes through a contraction flow apparatus. M_w and PDI are both lowered. M_w is lowered until M_{lim} is reached.[8]

Figure 1.2 shows a particular interesting example from Keller and Odell where they subjected a polystyrene sample of initial molecular weight (M_i) 20×10^6 Da to a complex strain rate cycle in an elongational flow field.[1] The polymer chains clearly show molecular weight reductions indicating, unequivocally, near midchain scission of both the starting material and the subsequent daughter fragments. Considering the thousands of covalent bonds macromolecules contain, the selectivity of this chemical event is truly remarkable.

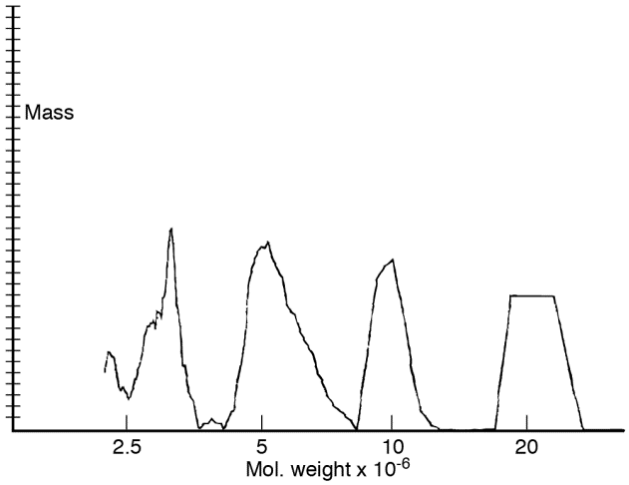

Figure 1.2. Polystyrene of M_w 20×10^6 Da subjected to an opposing jets apparatus with a complex strain rate cycle. Peaks at one half, one quarter, and one eighth of the initial M_w give evidence of progressive midchain scission.[1]

Concerning the nature of the bond breakage event, Kauzmann and Eyring proposed that the scission event within the mechanically stressed polymer was homolytic in nature.[7] Indeed, polymers subjected to ultrasonication in the presence of radical traps have provided evidence of homolytic bond scission.[10] While sonication of a solvent or small molecule can generate radicals,[11] the high amount of radicals present when polymer solutions are sonicated was used as evidence of the homolytic nature of chain scission. Electron spin resonance (ESR) has also been used to support the existence of macroradicals as a consequence of ultrasonication.[12] Computational and theoretical models of the force-induced scission of a variety of covalent bonds have recently been reviewed by Marx et al.[5] Given the nature of the homolytic bond scission and the generation of macroradicals, experimentalists have utilized these macroradicals to initiate polymerizations. Block copolymers have been synthesized by sonicating a solution of two different polymers which induces cleavage, followed by recombination of two chemically different polymer macroradicals which forms a block copolymer. Additionally, polymers have been

sonicated in a monomer solution which generates macroradicals, followed by initiation of polymerization of the monomer solvent.[11]

Mechanochemical design and intuition progressed when the introduction of 'weak links' into the polymer backbone was demonstrated by Encina and co-workers.[13] By inserting peroxide linkages randomly along the backbone of a polymer, Encina and coworkers demonstrated the weak-link hypothesis for influencing polymer mechanochemistry. The experimental evidence confirmed that the polymers with peroxide links degraded faster than control polymers when irradiated with ultrasound. The seminal report of true mechanochemical selectivity came from Berkowski et al. where a single azo linkage was installed in the center of a PEG chain and subjected to degradation via ultrasonication (Figure 1.3).[14] Experimentally, this polymer was shown to degrade faster than a control polymer through kinetic analysis of molecular weight reduction similar to the study of the peroxide linked polymers. Even more interestingly, the azo polymer was shown to cleave almost perfectly in half compared to the cleavage profile of the control polymer indicating scission directly at the azo group. These experiments, together with ^{13}C labelling, unambiguously showed for the first time the ability to enhance the rate of reactivity mechanochemically as well as the selectivity. Importantly, these experiments were conducted in conjunction with control experiments that showed different reaction products from thermolysis. This report set the stage for modern polymer mechanochemistry and literature reports began to shift away from demonstrating polymer mechanochemistry in terms of the chain scission of macromolecules and, instead, shifted to studies harnessing the mechanical energy for productive bond scission events with specific force-sensitive units embedded in polymer chains.

While most early reports of polymer mechanochemistry demonstrated chain scission in response to tensile stress, Hickenboth et al. explored a novel chemical reaction without the requirement of chain scission.[15] By inserting a benzocyclobutene mechanophore into the backbone of a PEG chain, they were able to demonstrate a mechanically induced electrocyclic ring opening to produce an orthoquinodimethide (Figure 1.3).

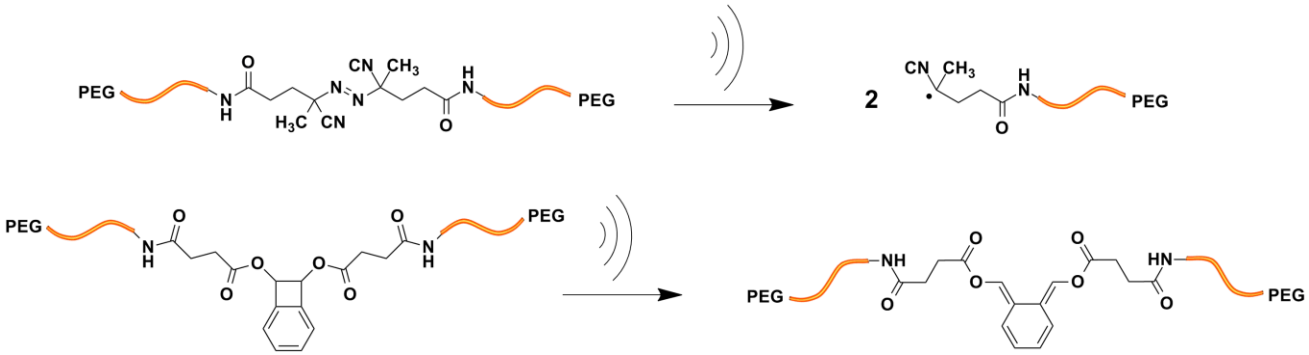

Figure 1.3. Site-specific reactivity of polymers containing azo and benzocyclobutene mechanophores subjected to an acoustic field generated by ultrasonication.[14,15]

A striking revelation in this work was the possibility of using mechanical force to promote a formally disallowed electrocyclic ring opening, according to the well-established Woodward-Hoffman rules. Since these seminal reports a diverse set of force-induced chemical responses within polymers has been developed by using specifically designed mechanophores and they are summarized in a recent review by Bielawski and coworkers.[4] With the birth of the mechanophore concept (Figure 1.4), the field of polymer mechanochemistry is now poised to explore unprecedented reactivity in polymeric materials, potentially offering new properties such as self-sensing and regenerative abilities to sustain synthetic materials far beyond their current service lifecycles. To this end, there is much excitement for the potential applications of synthetic polymers with embedded

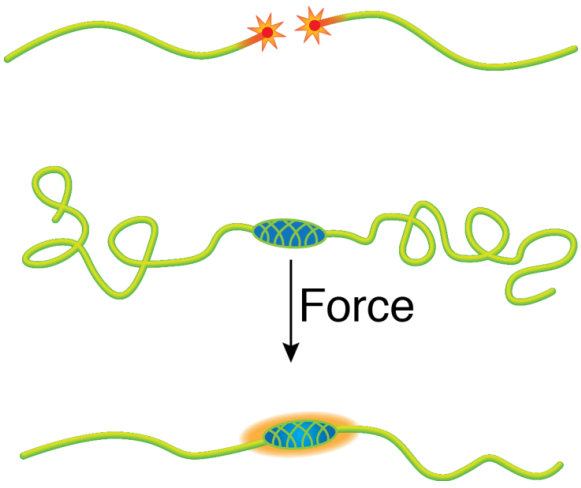

Figure 1.4. Evolution of polymer mechanochemistry from chain scission reactions to selective reactions of mechanophore units. In this new context, force concentrated at the center of a chain induces productive, rather than degradative, chemistry.

mechanochemical triggers. Synthetically mimicking mechanically responsive biological materials, such as bone, is now conceivable based on mechanochemical activation. The mechanophore concept has prompted new questions to be raised: How does one design a mechanically sensitive molecule? Are all chemical bonds inherently sensitive to mechanical force? Can this method be adopted by the bench chemist as an added toolbox to synthetic chemistry? Answers to these questions will rely not only on the creativity of the chemist but on the techniques at the disposal of the chemist to test reactivity concepts. The most prevalent techniques used to generate molecular strain for polymer solutions will be summarized in the following sections.

1.3 Turbulent Flow

Of all the techniques to generate elongational flow, turbulent flow provides the least ideal conditions for experimentation. However, researchers have been interested in the phenomenon of drag reduction for quite some time.[16] Drag reduction corresponds to the decrease in friction of a flowing liquid by the addition of small amounts of foreign substances, mainly long chain high molecular weight polymers. Drag reduction allows the velocity of a fluid to be increased while maintaining constant energy input and this effect has many implications in areas such as oil pipelines, flood water disposal, and even blood flow in the human body.[17] The drag reduction phenomenon is frustrated by the effect of polymer degradation due to the turbulent conditions. In turbulent flow, polymers are exposed to elongational straining as well as high shear forces which leads to chain scission.[18] Therefore, researchers have invested significant effort to understand polymer degradation in turbulent flow in the hopes to enhance polymer stability and prolong the drag reduction effect. Early studies of polymer chain scission were conducted in pipe flows, which is most closely associated with industrial applications.[19] Alternatively, geometries using Taylor-Couette flow and rotating disks have been investigated.[20,21]

The shear field in turbulent flow is inhomogeneous and not well-defined; therefore it is difficult to conduct precise kinetic analyses of mechanochemical activation and understand the fundamental mechanisms of chain scission. The residence time in the high strain rate zone is insufficient to fully stretch the molecule. This indicates that scission takes place in a partially coiled state. The majority of studies have used analytical methods such as changes in friction factor and intrinsic viscosity to indirectly assess polymer degradation. SEC with refractive index detection has also been used to measure changes in molecular weight and PDI. SEC has also been used to confirm near midchain scission in monodisperse polymers subjected to turbulent flow.[22] More recently, Vanapalli et al. have used light scattering measurements to attain absolute molar mass distributions and have developed a universal scaling theory

for polymer chain scission in turbulent flow.[23]

A number of parameters have been identified as being able to influence the rate of chain scission. Solvent quality has been shown to be important. Polymers have been found to degrade faster in poor solvents at low Reynolds numbers. In higher Reynolds numbers fluids, polymers have been observed to degrade faster in poor solvents. However, near-midpoint scission is approached in both good and poor solvents.[24] Additionally, the limiting molecular weight has been shown to be lower in poor solvents.[20] The scission rate increases or remains the same as the concentration is decreased[17] and as the molecular weight of the polymer is increased the rate of scission increases.[19] Furthermore, as the intensity of turbulence increases, the degree of scission increases.[19] Solvent viscosity was shown to have little effect on chain scission.[17] Finally, temperature plays a complicated role in mechanochemical reactions which can accelerate or retard the rate of reaction depending on the range of temperature studied.[25]

One of the main disadvantages of studying mechanochemical reactions in turbulent flow is the need for very high molecular weight polymers, generally in the range of 10^6 Da. It is difficult to synthetically produce extremely high molecular weight polymers with mechanophores bound in the center of the chain. Another significant drawback is the lack of a standardized apparatus for conducting turbulent flow experiments. Geometrical differences such as entrance effects are known to cause discrepancies in the outcome of the experiment[26] which frustrates reproducibility. This uncertainty has a significant impact on studying selective, mechanochemical reactions. Improvements in the technique as well as a unified mechanism of chain scission are needed. However, it is possible that mechanophores could offer a route to experimentally study the mechanism of chain scission in turbulent flow.

1.4 Opposed Jets and Cross Slots

A widely used technique to generate elongational flow with a stagnation point is opposed jets or cross slots which were extensively used by Odell and Keller.[1] This technique creates two opposing orifices through which a polymer solution flows. A region of zero velocity, called the stagnation point, is created by the geometry of the flow field (Figure 1.5).

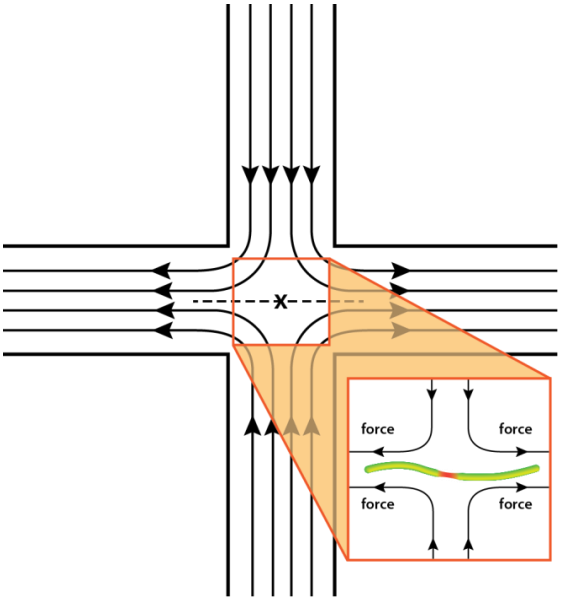

Figure 1.5. Flow field created in a cross slot apparatus. The direction of flow is shown by the arrows and the stagnation point is marked with an X. A representative polymer chain with tension (red region) developing near the center is shown.[27]

Polymers that get trapped in the stagnation point experience a high velocity gradient which causes elongation and, ultimately, chain rupture. Typically, chain scission has been reported to occur primarily near the midpoint.[27] However, only a small portion of polymers get caught in the stagnation point. Estimates of scission rate on a per pass basis from these types of flow fields have not been consistent.[28,29] A key parameter that can be controlled with these techniques is the strain rate. By changing the velocity of the flowing solution with a pump, the experimentalist can control the shear exhibited upon the polymers in solution. Another method with similar geometry that generates this type of flow field with a stagnation point is the 4-roller mill, although it is less commonly used.[30] With the 4 roller mills the strain rate and fluid velocity are controlled by adjusting the speed of the rollers. Two important strain rates identified in these experiments are the critical strain rate to elongation, $\dot{\varepsilon}_c$, and the fracture strain rate, $\dot{\varepsilon}_f$. The critical strain rate to elongation is characterized by alignment of the polymers in the stagnation point through the use of *in-situ* birefringence measurements. This experimental technique has a unique advantage because it can be used to apply controlled strain to polymers, allows visualization of alignment at $\dot{\varepsilon}_c$, and allows characterization of the fracture products after $\dot{\varepsilon}_f$ is attained.[1] Experimentally, it was shown that higher molecular weight polymers have lower values of $\dot{\varepsilon}_c$ and $\dot{\varepsilon}_f$.[27]

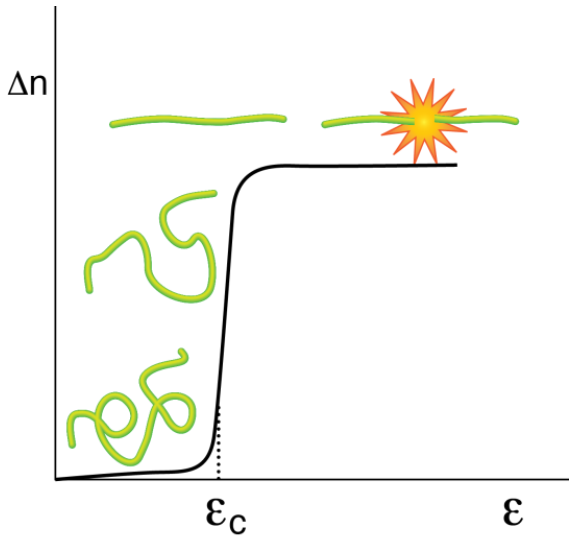

Figure 1.6. Plot of elongational flow-induced birefringence versus strain rate. Representative polymer conformations at various strain rates are shown.[27]

Representative data that can be collected from a typical experiment is shown in Figure 1.6, demonstrating birefringence as a function of strain rate. If the strain rate is reduced to zero by stopping the flow and the scan is repeated a new birefringence vs strain rate curve can identify fracture products. Two steps can be identified, $\dot{\varepsilon}_1$ and $\dot{\varepsilon}_2$ (Figure 1.7). Since it is known that higher molecular weight polymers have lower critical strain rates, $\dot{\varepsilon}_1$ can be assigned to the starting material. As the strain rate is increased, a new step, $\dot{\varepsilon}_2$, can be attributed to the fractured material. Differentiation can then yield chain length distributions. The ability to control strain rates between $\dot{\varepsilon}_c$ and $\dot{\varepsilon}_f$ presents a unique opportunity of studying reactivity of mechanophore-linked polymers while minimizing chain scission pathways. It would be very interesting to probe various mechanophores that do not require chain scission for activation. For example, benzocyclobutene, spiropyran, and *gem*-dihalocyclopropane mechanophores[4] only break a covalent bond within the mechanophore itself, without the need for chain scission. Therefore, this technique could be used to identify strain rates required for activation amongst different mechanophores. Additionally, the relative activation energies of mechanophores such as dicyanocyclobutanes and triazoles,[4] which result in chain fracture after activation, could be directly compared.

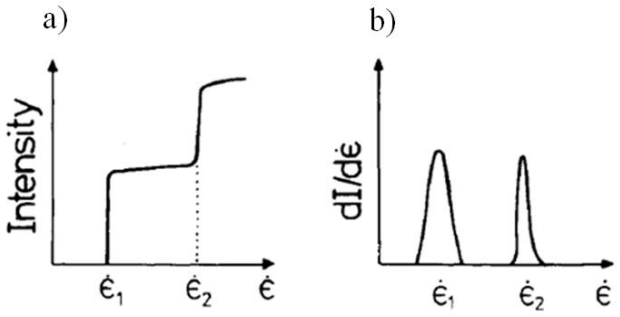

Figure 1. 7. a) Representation of birefringence intensity vs. strain rate of two monodisperse polymer fractions b) Differentiated with respect to strain rate showing two peaks corresponding to the two fractions.[27]

Additional factors affecting rates of degradation have been identified. As temperature is increased $\dot{\varepsilon}_f$ decreases.[29] As the concentration is increased scission becomes less chain-centered and more random in nature.[31] As the strain rate is increased, the number of polymers cleaved per pass increases.[29]

This technique requires very high molecular weight polymers to be used (typically 10^5-10^6 Da). This characteristic is a consequence of the fact that lower molecular weight polymers need increasingly higher strain rates to rupture. Therefore, the limiting molecular weight threshold is significantly higher than in techniques such as ultrasound, which will be discussed later. Another unusual drawback is that as polymers become increasing larger in size a condition where $\dot{\varepsilon}_c = \dot{\varepsilon}_f$ is reached. This sets a theoretical upper limit to the chain length which can be stretched without fracture. Chains above this upper limit would fracture without fully elongating. For polystyrene this limit is thought to be 30×10^6 Da.[1] Additionally, multiple passes through the apparatus are needed to induce scission in all polymer chains. If the chains are long enough and the strain rate is not carefully controlled, secondary cleavage events could proceed at the same rate as primary cleavage, complicating kinetic analyses (See Figure 1.2). Finally, the experimental setup is more complex than other techniques available.

1.5 Contraction Flows

Another technique for generating strain within polymers is a simple contraction flow. This technique was widely studied by Nguyen and Kausch.[32] A pressure differential drives a fluid across a narrow contraction as shown in Figure 1.8.[33] The sudden acceleration of the fluid across the contraction creates a flow field of high strain rate without a stagnation point and has been termed transient

elongational flow. Polymers experience a strong flow for only a short residence time which is less than the characteristic relaxation time of the polymer and scission occurs while the individual polymer chains are partially stretched.[32] However, polymers still demonstrate a distinct propensity for midchain scission.

Analysis is typically performed by measuring molecular weight distributions with SEC. Nguyen and Kausch determined $\dot{\varepsilon}_f$ by collecting plots of scission yield vs. strain rate and extrapolating the scission yield to zero. The scission yield was calculated from the ratios of the areas corresponding to the degraded polymer to the total area under the SEC trace.[34] Birefringence measurements have also been used to measure polymer orientation in the contraction flows. However, the polymers are continually flowing past the optical path resulting in a non-uniform distribution of the change in birefringence, unlike the stagnation point of a cross slot, significantly complicating the measurement.[33,35]

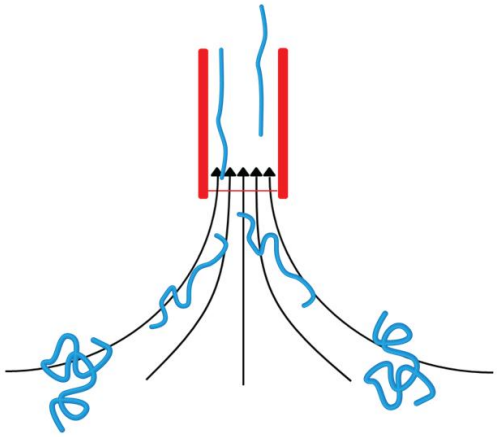

Figure 1.8. Representative flow field generated in a simple contraction apparatus. Polymer elongation begins near the entrance of the contraction.

The degree of molecular stretching is largely controlled by the flow rate and the polymer relaxation time. Polymers subjected to contraction flows show chain fracture above a critical strain rate that scales with initial polymer molecular weight. Fracture strain rate is weakly dependent on solvent viscosity.[32] The geometry of the contraction has been shown have a significant effect on the observed results. Specifically, increases in the orifice diameter in the contraction have led to a decrease in $\dot{\varepsilon}_f$.[36] Solvent quality was found to have little effect on the fracture strain rate.[37] Finally, the rate of scission increases in concentrated solutions.[38]

The main advantage of this technique is the simple experimental setup. However, geometrical design

must be carefully considered in order to obtain reproducible results. Up to 90% scission yield has been reported in a single pass in contraction flow which is significantly higher than opposed jets and cross slots.[37] While the strain rate can be controlled in contraction flows, only critical fracture rates have been adequately identified. Along with previously discussed techniques, high molecular weight polymers are needed for investigation. M_{lim} has been reported to be about 300 kDa while operating the apparatus at maximum fluid velocity.[32] To date, no mechanophore linked polymers have been studied with this technique.

1.6 Ultrasound

A fundamentally different technique that has been used to study polymer degradation since as early as 1933 is an acoustic field.[39] Sound is the compression and expansion of waves passing through a medium. Sound waves with frequencies of approximately 1-18 kHz, or vibrations per second, can be sensed by humans. However, sound waves with frequencies greater than ~20 kHz are out of the range of human hearing and are called ultrasound. Ultrasonication, the act of applying ultrasound to a medium can been applied to solutions in the form of an ultrasonic bath or an ultrasonic probe.[40] For an ultrasonic bath, typically, a solution is placed in a vessel and the vessel is lowered into the liquid bath. No direct contact between the sample and apparatus is necessary, as the ultrasound waves travel through the liquid bath and into the liquid sample. Ultrasonic probes, on the other hand, are submerged directly into the sample (Figure 1.9).[40]

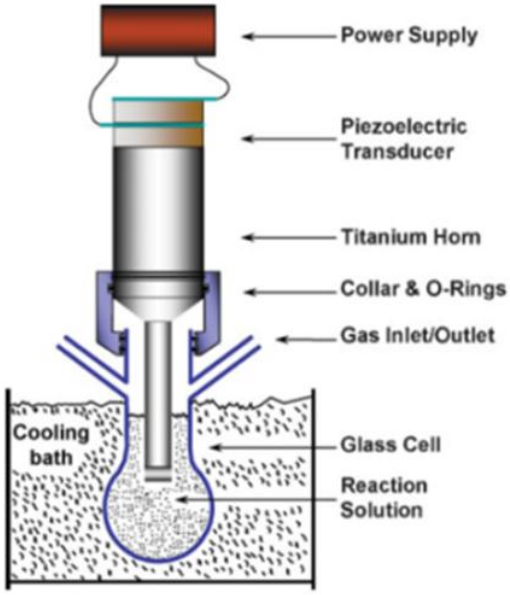

Figure 1.9. Ultrasonic probe experimental set up.[40]

Ultrasonic probes are useful because they offer higher power intensities and more control to the user and have become the method of choice for screening mechanophore reactivity.[4] Additionally, the power that can be delivered by the probe can be calibrated which facilitates reproducibility of experiments.[41] The vibrating probe contains a point of no activity, called the nodal point, to which the collar is threaded. Glass reaction vessels that have been designed to connect to the probe via the collar are called Suslick cells.[42] Suslick cells allow for inert gases to be introduced to the sample, temperature monitoring, and aliquot removal. Furthermore, a cooling mechanism is applied to either apparatus due to the heat generated from sonication. For an ultrasonic bath, cold water can be circulated in the bath and for the probe the vessel can simply be lowered into a cooling bath.

The mechanism of converting ultrasound waves to energy in the form of force on a polymer chain is through a process called cavitation (Figure 1.10).[2]

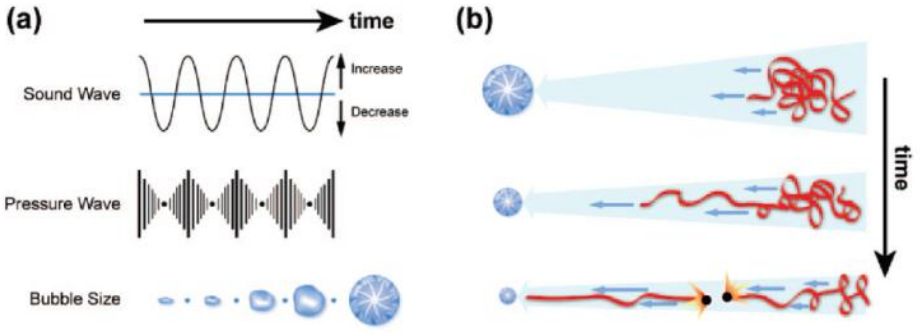

Figure 1.10 a) Process of acoustic cavitation b) Representation of polymer chain cleavage in response to acoustic cavitation.[2]

Cavitation is defined as the nucleation, growth, and collapse of bubbles in a liquid.[10,11,43] Polymer chains near a collapsing bubble experience solvodynamic shear forces as the proximal chain end is pulled toward the void creating by the imploding bubble. The forces that develop along the backbone result in irreversible cleavage through the scission of a covalent bond. The cleavage event is non-random and occurs within 15% of the center of the polymer chain,[11] although there is currently no direct evidence of full elongation of the chains. Chain scission induced by ultrasonic cavitation fits the criteria of transient elongational flow; however, macroscopically the solution is not flowing, which differentiates this technique from those previously discussed. Unlike opposed jets and contraction flows, where a precise strain rate, $\dot{\varepsilon}_c$ or $\dot{\varepsilon}_f$, can be used to study the deformation of polymers in solution, a distribution of strain rates is operative during acoustic cavitation.[44] Thus, in ultrasonication the scission rate and M_{lim} are dictated by an effective strain rate, $\dot{\varepsilon}_{eff}$, that is determined by the dynamics of microbubble collapse. An approximate equation describing the bubble wall velocity (υ_R) during bubble collapse is given by[44]

$$\upsilon_R = dR/dt = (2P_h/3\rho)^{0.5}(R_m^3/R^3 - 1)^{0.5} \quad (1)$$

In this equation, ρ is the solvent density, P_h is the external pressure, R_m is the initial radius and R is the instantaneous radius of the imploding void space. By neglecting solution compressibility, the strain rate distribution has been calculated according to the following equation[44]

$$\dot{\varepsilon}_{rr}(r) = -2\upsilon_R R^2 r^{-3} \quad (2)$$

At various time intervals during bubble collapse, the strain rate distribution is plotted in Figure 1.11.[44]

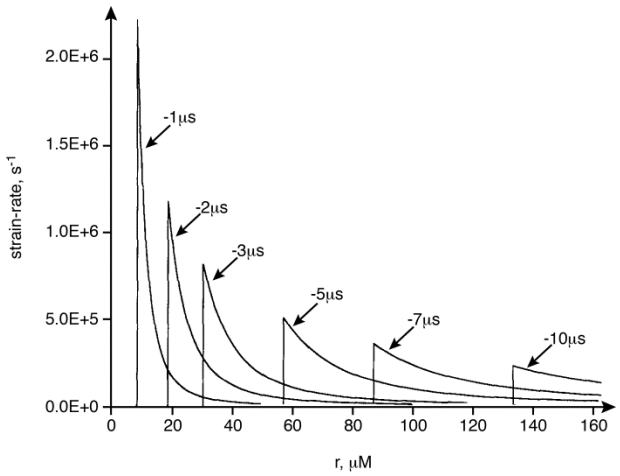

Figure 1.11. Strain rate distribution during bubble collapse plotted for various implosion times. The distance from the cavity center is *r*.[44]

A clear time dependence of the strain rate on the radius of the imploding bubble is observed. Due to the strain rate gradient, an individual chain can experience a range of strain rates, even during a single implosion event. Therefore it is possible that chains could be cleaved multiple times during a single implosion if the daughter fragments are larger than M_{lim} of $\dot{\varepsilon}_{eff}$ under the given conditions of the experiment. Using scission kinetics obtained in both contraction flow devices as well as M_{lim} values measured for ultrasonication experiments, Nguyen et al. have determined that $\dot{\varepsilon}_{eff}$ during acoustic cavitation is $\geq 3 \times 10^6$ s^{-1} (Figure 1.12).[44]

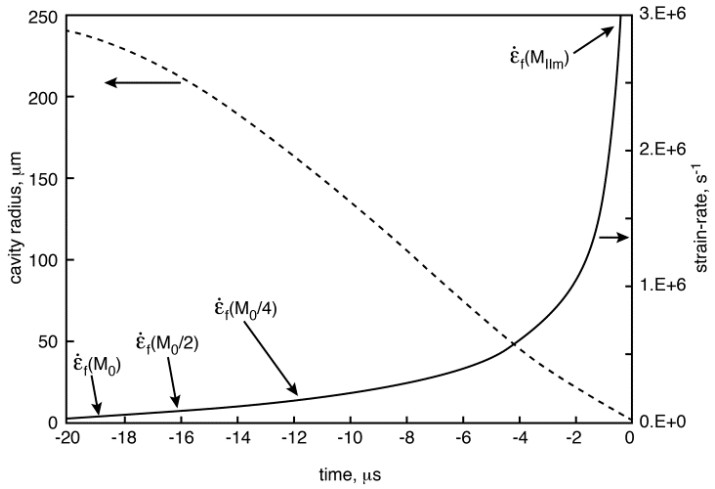

Figure 1.12. Temporal evolution of bubble radius (left axis) and strain rate maximum (right axis) during bubble collapse.[44]

Comparatively, strain rates on the order of 10^3 - 10^6 s^{-1} are achievable in opposed jets and contraction flows.[2] Therefore, acoustic cavitation allows the highest strain rates of all flow fields discussed, and, ultimately, accommodates lower molecular weight polymers to be studied with this technique. Additionally, significant effort has been put forth to preclude thermal effects of cavitation as the source of energy for mechanochemical activation, especially for mechanophore linked polymers.[2-4]

Chain scission analysis is typically performed by monitoring molecular weight distributions during the course of an experiment with SEC. With the recent creation of novel mechanophore containing polymers, additional analytical techniques such as UV-Vis spectroscopy, ^{1}H and ^{13}C NMR spectroscopy, and circular dichroism spectroscopy have been required to characterize these selective, mechanochemical transformations.[2-4]

The parameters effecting chain scission have been studied extensively and are summarized in Table 1.[10,45-47] Ultrasound power intensity has been shown to have a clear effect on the rate of scission which has been mainly attributed to more cavitation events per unit of volume. However, many reports do show a slight lowering of M_{lim} with increasing power intensity, although there are conflicting reports on this matter.[10,46] A lower M_{lim} for a given set of conditions suggests an increase in $\dot{\varepsilon}_{eff}$ due to increased bubble size resulting in higher forces experienced by the polymer chains. Increasing power intensity increases the temperature of the solution which is a factor that should be accounted for. Additionally, sonication time should be taken into account when measuring M_{lim} values of various intensities, as a slower reaction rate will take longer to reach a true M_{lim}. Overall, it seems the main effect of increased power intensity is a higher frequency of cavitation with a minor contribution of increasing $\dot{\varepsilon}_{eff}$ on the polymers. Furthermore, sonication frequency has been shown to have little effect on the degradation rate below 500 kHz.[10]

Most of the parameters in Table 1.1 have been explored in polymer degradation studies and are thought to extrapolate to mechanophore activation. Currently, few studies have investigated the effects of these fundamental parameters on selective mechanophore activation. An elegant example of controlling mechanochemical reactivity by altering the parameters of the ultrasonication technique was demonstrated by Bielawski and co-workers.[48] In their work they used a power setting of 10.1 W/cm^2 (setting of 23% amplitude on the instrument) to induce an isomerisation reaction of a binol mechanophore. At a higher power intensity of 13.2 W/cm^2 (28% amplitude) significant chain scission was observed. At a lower power setting of 8.30 W/cm^2 (20% amplitude), no reaction occurred. By identifying these conditions they were able to exclude chain scission while promoting the mechanochemical isomerisation. Analogous to the cross slot and opposed jets technique where controlled strain rates of $\dot{\varepsilon}_c$ can stretch a polymer without fracture, Bielawski and co-workers have demonstrated a set of conditions that can apply controlled forces throughout the entire ensemble of polymers with ultrasound.

Table 1.1. Parameters affecting the rate of ultrasonic induced chain scission.

Parameter	Relationship to rate	Rationale
Ultrasound power intensity	As intensity increases, rate increases	Increasing intensity causes more cavitation events per unit volume
Concentration	As concentration increases, rate decreases	Increasing concentration increases chain entanglements, decreasing effective MW
Vapor pressure of solvent	As vapor pressure increases, rate decreases	Cushioning of bubble collapse by increased vapor within bubble
Temperature	As temperature increases, rate decreases	Increasing temperature increases vapor pressure
Gas solubility of solvent	As gas solubility increases, rate decreases	Increasing solubility increases gas in cavity, which cushions collapse
Polymer MW	As MW increases, rate increases	Increasing MW increases solvodynamic forces on polymer
Viscosity	As viscosity increases, rate decreases	Increased viscosity suppresses cavitation

Moreover, recent studies have identified electronic and steric effects of the mechanophore itself as well as polymer type to be important factors that influences mechanophores activation. [49-51] There have been many attempts to extract rates of cleavage through kinetic analysis of the molecular weight changes of sonicated polymers. The mathematical models used can be divided into two categories: those that include a limiting molecular weight term and those that do not include this term. These models have been recently summarized by Giz et al.[52] Reaction rate analysis has been fundamentally important to quantify reactivity differences in both chain scission studies and mechanophore activation studies. If sonication parameters are carefully controlled, it becomes possible to analyze and quantify differences in reactivity among polymers as well as directly compare mechanophore reactivity. Figure 1.13 shows an example of a rate constant vs. molecular weight plot of dicyanocyclobutane mechanophore-linked poly(methylacrylates) of differing stereochemistry.[49] Two important attributes in these types of plots can give information about reactivity differences: the slope and the threshold molecular weight (i.e. x-axis intercept, or elevation). Statistical analyses can been used to compare the slope or molecular weight threshold difference in each curve.[49]

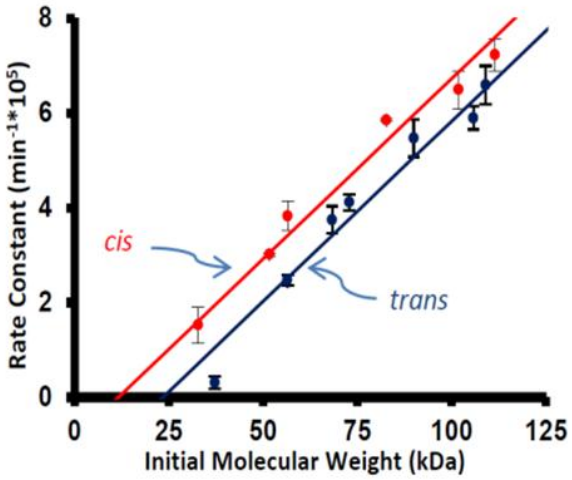

Figure 1.13. Experimentally determined reactivity differences of dicyanocyclobutane mechanophores with cis and trans stereochemistry. Lower M_{lim} of the cis stereoisomer was attributed to higher reactivity of this derivative.[49]

The primary advantages for using ultrasonication for studying mechanophore reactivity as opposed to the previous techniques described are the ease of experimental setup and the fact that much lower molecular weight polymers are susceptible to activation by acoustic cavitation. Typically, the limiting molecular weight for polymers subjected to ultrasonication is around 30 kDa.[32] Most recent mechanophore screening studies have used living radical polymerization techniques to generate polymers with chain centered mechanophores of sufficient molecular weight to readily study within an acoustic field.[2,4] The main disadvantages in using this technique have come from the need to exhaustively rule out thermal contributions to mechanophore activation through the synthesis and study of control polymers. However, considering the number of reports demonstrating that proper connectivity of mechanophores is required it is generally considered to be a purely mechanical phenomenon.

1.7 Conclusion

While several techniques have been used to study polymer chain scission in elongational flow fields, ultrasonication has become the primary tool for screening mechanophore reactivity in solution. It is particularly well suited for studying mechanically facilitated reactions due to the simple experimental setup and the synthetically accessible lower molecular weight polymers. A standardized experimental apparatus and set of experimental conditions is easiest to achieve with ultrasonication. Most parameters for ultrasonication are readily controlled while complex geometrical considerations are very important for

turbulent flows, opposing jets, cross slots, and contraction flows. However, very few reports have utilized *in-situ* measurement techniques for the analysis of ultrasound induced polymer chain scission[52,53] and no reports have demonstrated this for mechanophore activation studies. Considering this is one of the primary attributes of the opposed jets and cross slots techniques it would be worthwhile to pursue, potentially with flow cell geometry, to further improve the ultrasonication technique for polymer mechanochemistry studies.

With techniques available and a growing portfolio of known mechanophores, chemists are now in a position to break ground discovering new mechanically facilitated reactions. Particularly promising areas are force-activated catalysis as well as self-reporting and self-healing materials. Directly creating new chemical bonds with mechanical force is another challenging frontier that will surely come into fruition in the future. To this end, there is almost no foreseeable upper limit to the functionality that can be embedded into synthetic materials with judiciously designed mechanophores.

1.8 References

(1) A. Keller and J. A. Odell, *Coll. Polym. Sci.* **1985**, *263*, 181.

(2) M. M. Caruso, D. A. Davis, Q. Shen, S. A. Odom, N. R. Sottos, S. R. White and J. S. Moore, *Chem. Rev*. **2009**, *109*, 5755 and references therein.

(3) Z. S. Kean and S.L. Craig, *Polymer* **2012**, *53*, 1035.

(4) J. N. Brantley, K. M. Wiggins and C. W. Bielawski, *Polym. Int.* **2012**, *62*, 2 and and references therin.

(5) J. Ribas-Arino and D. Marx, *Chem. Rev.* **2012**, *112*, 5412.

(6) H. Staudinger and H. F Bondy, *Ber. Dtsch. Chem. Ges.* **1930**, *63***,** 734.

(7) W. Kauzmann and H. J. Eyring, *J. Am. Chem. Soc.* **1940**, *62*, 3113.

(8) B. A. Buchholz, J. M. Zahn, M. Kenward, G. W. Slater and A. E. Barron, *Polymer* **2004**, *45*, 1223.

(9) R. S. Porter, J. F. Johnson, *J. Phys. Chem.* **1959**, *63*, 202.

(10) A. M. Basedow and K. H. Ebert, *Adv. Polym. Sci*. **1977**, *22*, 83.

(11) K. S. Suslick and G. J. Price, *Annu. Rev. Mater. Sci*. **1999**, *29*, 295.

(12) M. Tababta, T. Miyazawa, O. Kobayashi, and J. Sohma, *J. Chem. Phys. Lett.* **1980**, *73*, 178.

(13) M. V. Encina, E. Lissi, M. Sarasúa, L. Garagallo and D. J. Radic, *Polym. Sci. Polym. Lett. Ed.* **1980**, *18*, 757.

(14) K. L. Berkowski, S. L. Potisek, C. R. Hickenboth and J. S. Moore, *Macromolecules* **2005**, *38*, 8975.

(15) C. R. Hickenboth, J. S. Moore, S. R. White, N. R. Sottos, J. Baudry and S. R. Wilson, *Nature* **2007**, *446*, 423.

(16) R. W. Patterson and F. H. Abernathy, *J. Fluid. Mech.* **1970**, *43*, 689.

(17) W. Brostow, *J. Ind. Eng. Chem.* **2008**, *14*, 409.

(18) J. Culter, J. L. Zakin and G. K. Patterson, *J. Appl. Polym. Sci*. **1975**, *19*, 3235.

(19) T. Moussa and C. Tiu, *Chem. Eng. Sci*. **1994**, *29*, 1681.

(20) C. A. Kim, J. T. Kim, K. Lee, H. J. Choi and M. S. Jhon, *Polymer* **2000**, *41*, 7611.

(21) T. Nakken, M. Tande and A. Elgsaeter, *J. Non-Newt. Fluid Mech.* **2001**, *97*, 1.

(22) A. F. Horn and E. W. Merrill, *Nature* **1984**, *312*, 140.

(23) S. A. Vanapalli, S. L. Ceccio and M. J. Solomon, *PNAS* **2006**, *103*, 16660.

(24) T. Moussa, C. Tiu and T. Scridhar, *J. Non-Newt Fluid Mech.* **1993**, *48*, 261.

(25) F. Hadri, A. Besq, S. Guillou and R. Makhlouf, *J. Non-Newt. Fluid Mech.* **2011**, *166*, 326.

(26) S. A. Vanapalli, and M. T. Islam, *Phys. Fluids* **2005**, *17*, 095108.

(27) J. A. Odell and A. Keller, *J. Polym. Sci. Part B Polym. Phys*. **1986**, *24*, 1889.

(28) D. Hunkeler, T. Q. Nguyen and H. H. Kausch, *Polymer* **1996**, *37*, 4257.

(29) J. A. Odell, A. J. Muller, K. A. Narh and A. Keller, *Macromolecules* **1990**, *23*, 3092.

(30) D. P. Pope and A. Keller, *Coll. Polym. Sci*.,**1977**, *255*, 633.

(31) J. A. Odell and M. J. Miles, *Polymer* **1985**, *26*, 1219.

(32) T. Q. Nguyen and H. H. Kausch, *Adv. Polym. Sci.* **1992**, *100*, 74.

(33) G. Yu, T. Q. Nguyen and H. H. Kausch, *J. Polym. Sci. Part B: Polym. Phys*. **1998**, *36*, 1483.

(34) T. Q. Nguyen and H. H. Kausch, *J. Non-Newt. Fluid Mech*. **1988**, *30*, 125.

(35) T. Q. Nguyen, *Chimia* **2001**, *55*, 147.

(36) T. Q. Nguyen and H. H. Kausch, *Coll. Polym. Sci* **1991**, *269*, 1099.

(37) T. Q. Nguyen and H. H. Kausch, *Polymer* **1992,** *33*, 2611.

(38) J. D. Clay and K. W. Koelling, *Polym. Eng. Sci.* **1997**, *37*, 789.

(39) E. W. Flosdorf and L. A. Chambers, *J. Am. Chem. Soc*. **1933**, *55*, 3051.

(40) J. H. Bang and K. S. Suslick, *Adv. Mater*. **2010**, *22*, 1039.

(41) T. J. Mason, J. P. Lorimer and D. M. Bates, *Ultrasonics* **1992**, *30*, 40.

(42) K. S. Suslick, J. W. Goodale, P. F. Schubert and H. H. Wang, *J. Am. Chem. Soc*. **1983**, *105*, 5781.

(43) K. S. Suslick, *Science* **1990**, *247*, 1439.

(44) T. Q. Nguyen, Q. Z. Liang and H H. Kausch, *Polymer* **1997**, *38*, 3783.

(45) G. J. Price and P. F. Smith, *Polym. Int*. **1991**, *24*, 159.

(46) G. J. Price and P. F. Smith, *Polymer* **1993**, *34*, 4111.

(47) G. J. Price and P. F. Smith, *Eur. Polym. J*. **1993**, *29*, 419.

(48) K. M. Wiggins, Todd. H. Hudnall, Q. Shen, M. J. Kryger, J. S. Moore and C. W. Bielawski, *J. Am. Chem. Soc.* **2010**, *132*, 3256.

(49) M. J. Kryger, A. M. Munaretto and J. S. Moore, *J. Am. Chem. Soc*., **2011**, *133*, 18992.

(50) J. N. Brantley, S. S. M. Konda, D. E. Makarov and C. W. Bielawski, *J. Am. Chem. Soc*. **2012**, *134*, 9882.

(51) H. M. Klukovich, Z. S. Kean, A. L. Black Ramirez, J. M. Lenhardt, J. Lin, X. Hu and S. L. Craig, *J. Am. Chem. Soc*. **2012**, *134*, 9577.

(52) A. Akyüz, H. Catalgil-Giz, A. Giz, *Macromol. Chem. Phys.* **2008**, *209*, 801.

(53) A. Akyüz, H. Catalgil-Giz, A. Giz, *Macromol. Chem. Phys.* **2009**, *210*, 1331.

Chapter 2 - Mechanophore Synthesis

2.1 Introduction

Spiropyrans were first demonstrated as successful mechanophores by Potisek et. al with solution based experiments[1] and have since been utilized as mechanophores for a variety of investigations. Davis et. al used spiropyrans as color-generating mechanophores for the first report of solid-state mechanophore activation.[2] Spiropyrans have been used to investigate chain mobility,[3] cross-linker length effects,[4] mechanical reorientation,[5,6] and mechanically biased reactivity.[7] Unpublished works have also looked at linking geometry,[8] polymer chain orientation,[9] creep activation.[10]

From a synthetic standpoint, a common theme to all of the successful studies of spiropyrans has been the linking geometry at the 5′ and 8 positions. Here, the overarching goal is to study the polymer architecture effects on the mechanophore. Therefore, the linking geometry (Figure 2.1) was kept constant throughout the works presented herein. The primary reaction studied is the electrocyclic ring-opening of spiropyran to merocyanine. This reaction is influenced by light, thermal energy, pH, solvent, and mechanical force.[2,11,12] In the context of mechanically-induced reactivity this work aimed to elucidate the influence of the polymer chains in force transduction to the mechanophore in hopes of gaining knowledge toward materials with higher mechanical sensitivity.

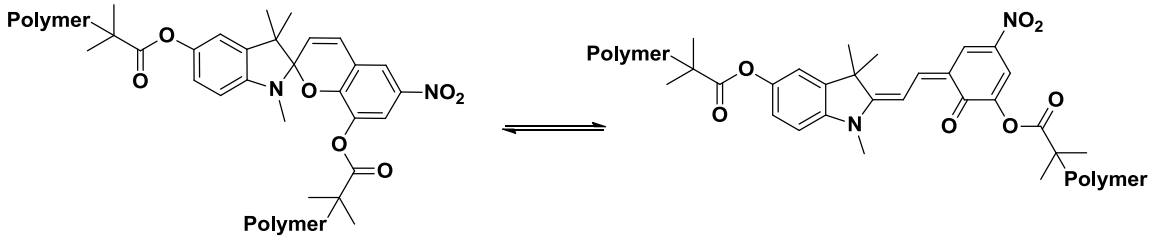

Figure 2.1. The primary reaction studied in this thesis. The effect of various polymer chain chemistries and topologies are the focus.

2.2 Branched Initiators

Spiropyrans functionalized with α-bromo esters have been successfully integrated in poly(methyl methacrylate) (PMMA) and poly(methyl acrylate) (PMA) and their mechanochemical activation has been thoroughly characterized and reported.[1-3, 5] Spiropyrans containing this functional group are amenable to living radical polymerizations that allow control over mechanophore position, molecular weight, and PDI. These three characteristics are crucial to comparing various systems containing the same mechanophore.

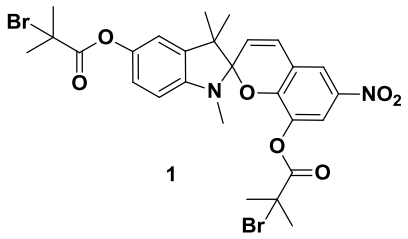

Figure 2.2. Structure of the established spiropyran mechanophore used as an initiator for living radical polymerizations.[1-3,5]

A major goal of the works presented herein was to compare linear polymer architectures to branched polymer architectures. Spiropyrans functionalized with additional α-bromo esters (i.e. > 2) would give additional polymerization sites to grow additional polymer chains from a single spiropyran. Ideally, this investigation would probe only a single change to the previously studied linear polymers: the effect of additional polymer chains. Therefore, consideration was taken to mimic structure (**1**) as closely as possible. Major concerns with the synthesis of new spiropyrans were potential changes to the electronics and the effect of different connections of the polymer to the mechanophore. While a reasonable prediction can be made with many small molecules regarding the electronic ramifications of synthesizing derivatives (e.g. addition or removal of electron donating or withdrawing groups), spiropyrans are unusual compounds that can be sensitive to even slight changes in structure.[8] Therefore, electronic differences between the compounds could only be known with the compounds in hand. Regarding the connectivity, the original spiropyran is connected to the polymer chains via an ester linkage. Beyond the ester linkage, C-C bonds connect the polymer backbone together. Therefore for a synthetic scheme to develop multiple initiators on the spiropyran using only esters and C-C bonds was targeted. Regarding the number of additional chains to add to the spiropyran, any number greater than two could potentially be targeted. However, multiples of two were targeted as the most reasonable systematic approach for branched polymers.

2.2.1 Tetra-Functionalized Initiator

To obtain a spiropyran functionalized with four α-bromo esters, specifically two on the indole half and two on the benzopyran half, 2,2-bis(hydroxymethyl)propionic acid (bis-HMPA) was first esterified with 2-bromo-propionyl bromide using a modified literature procedure[13] to achieve difunctional dendron **2**. Purification of this compound was achieved by column chromatography and crystallization as opposed to the hot extraction outlined in ref. 13. Esterification of compound **2** and dihydroxy spiropyran[1,2,7] was achieved by first converting **2** to an acid chloride. Compound **2** was added to

dichloromethane, followed by drop wise addition of fresh oxalyl chloride. A catalytic amount of dimethylformamide was added (one drop) which immediately caused evolution of bubbles. Over the course of 4 h the clear solution became yellow. Excess oxalyl chloride was removed by successive evaporation cycles where the reaction mixture was rotovapped to dryness and redissolved in 1,2-dichloroethane multiple times and evaporated, repeatedly. The compound was then placed under high vacuum to remove the remaining 1,2-dichloroethane. Esterification of **2** with dihydroxy spiropyran was achieved in the presence of DMAP and pyridine in dry THF. Pyridine was chosen as the base due to the fact that it dissolved the dihydroxy spiropyran better than triethylamine, presumably because it is a heteroaromatic compound more similar in structure to the spiropyran. After purification by column chromatography, crystallization was attempted multiple times but the compound always precipitated from solution giving an amorphous solid in 30% overall yield.

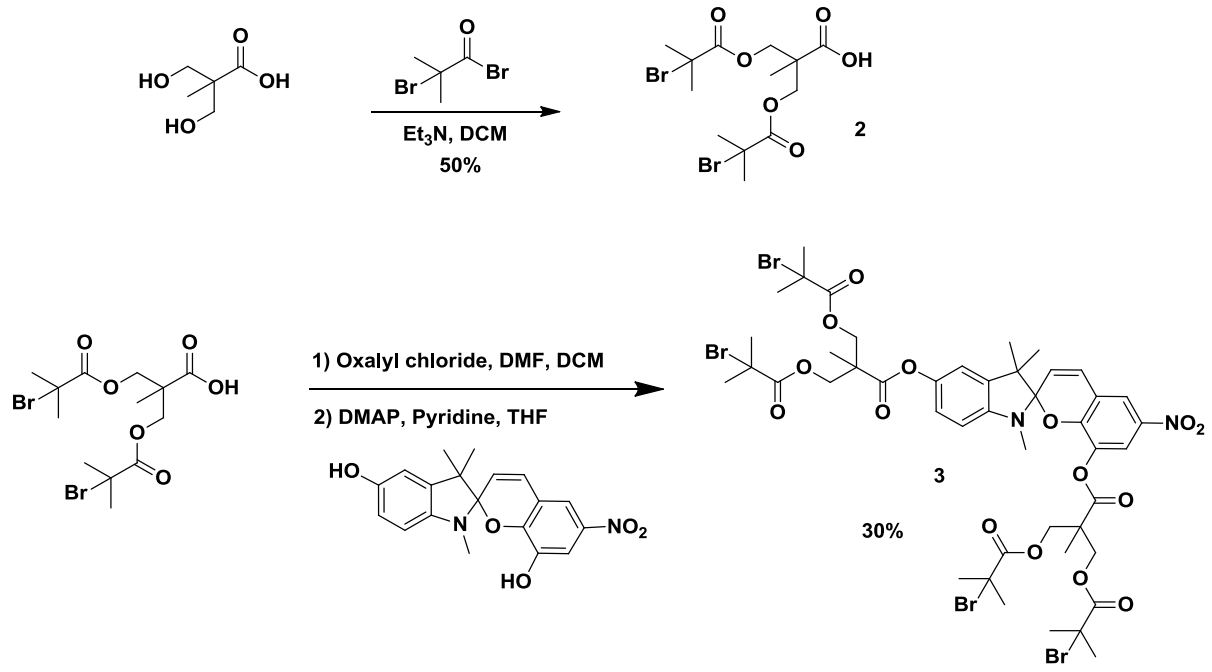

Scheme 2.1 Synthetic route to tetra-functional initiator **3.**

2.2.2 Octa-Functionalized Initiator

Attempts were made to react **2** directly with bis-HMPA, both by converting **2** to an acid chloride and under carbodiimide conditions to achieve an octafunctional dendron, but these attempts were unsuccessful. Alternatively, high generation dendrimer have also been reported based on bis-HMPA as the repeating unit.[14,15] Utilizing benzylidene-protected anhydride (compound **5)** couplings and hydrogenolysis reactions, high generation polyester dendrimers can be achieved in good yields with no means of purification other than solvent extraction and precipitation.[17-19] Thus, literature procedures were

followed to acquire compounds **4** and **5** as shown in scheme 2.[17] Acquisition of the carboxylic acid **4** was achieved by the reaction of 2,2-bis(hydroxymethyl)-propionic acid and benzaldehyde dimethyl acetal in the presence of a catalytic amount of *p*-toluenesulfonic acid in acetone. After acid catalyzed protection of the diol group on the carboxylic acid, the product was obtained via simple vacuum filtration and washing with cold acetone to produce a white fragrant crystalline material in 60 % yield. Compound **4** was then reacted with N,N'-dicyclohexylcarbodiimide (DCC) via carbodiimide coupling in which a large amount of dicyclohexylurea (DCU) byproduct was formed. The byproduct was removed by two filtrations. Literature citation notes only one filtration resulting in a mostly pure product. To obtain greater purity a second vacuum filtration using a fritted filter was performed to remove residual DCU. The resulting filtrate was then precipitated into hexanes. After filtration and washing with hexanes compound **5** was recovered as a white solid in 87% yield.

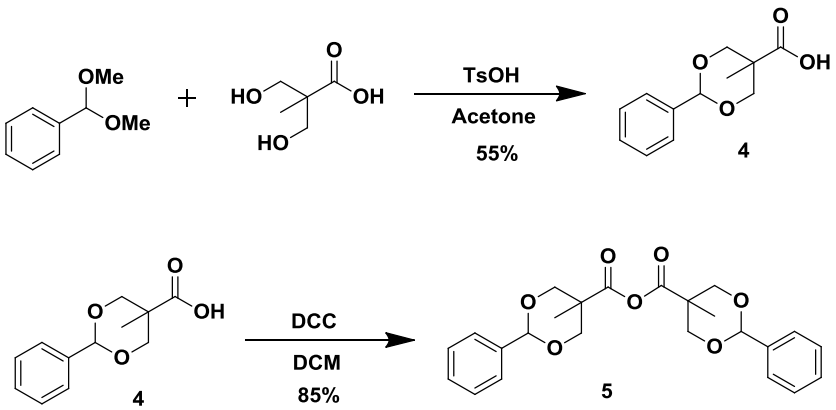

Scheme 2.2 Synthesis of dendron building blocks **4** and **5**.[17-19]

Parrott et. al reported the use of a protecting group for the focal point of the dendron that is easily removable by base to expose the carboxylic acid functionality at the focal point when desired.[19] Since esterification reactions of the dihyroxy spiropyran and carboxylic acid derivatives had been successful in previous syntheses, the synthetic method was modified to achieve the desired compounds in this work.

Polyeester dendrons were grown in sequential generations beginning with the reaction of the p-toluene sulfonyl ethanol with compound **5** in the presence of pyridine and DMAP in dichloromethane as shown in scheme 2.3. After 24 hours water was introduced to hydrolyze excess **5**. The reaction mixture was then washed with acid, base and brine and evaporated to dryness to yield **6** in 95% yield.[19]

Compound **6** was then deprotected via hydrogenation to facilitate further generational growth by reaction of H_2 in an equal part mixture of dichloromethane and methanol in the presence of a $Pd(OH)_2/C$ catalyst. The solvent was first sparged with H_2 for 30 minutes before the reactants and catalyst were added to the reaction flask to saturate the solvent mixture with as much H_2 as possible. After addition of

all the reaction components, the reaction flask was vented back filled with H_2 three time and kept under balloon pressure (slightly higher than atm pressure). After 24 h the reaction mixture was diluted with methanol and the catalyst was filtered off. The byproduct, toluene was easily removed by evaporation. Compound **7** was achieved in 95% yield. Compounds **8** and **9** were achieved by similar reaction conditions of esterification followed by hydrogenolysis.

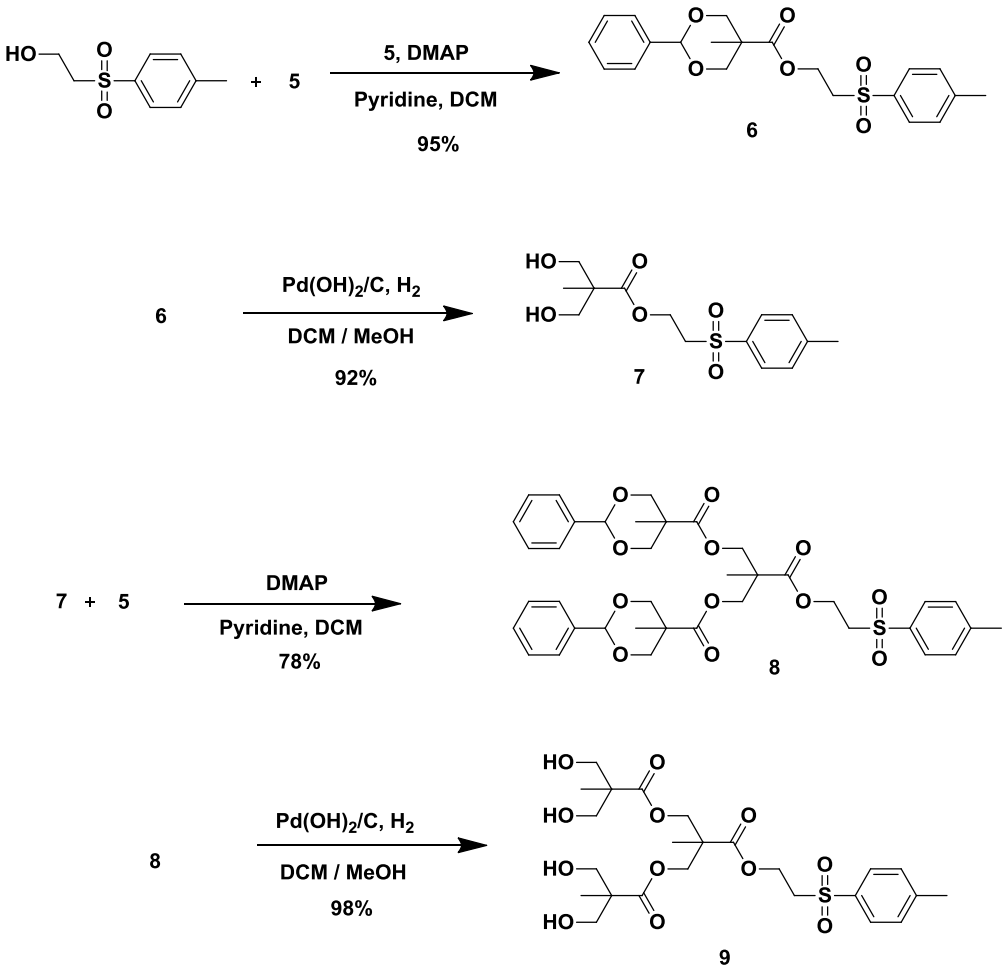

Scheme 2.3. Introduction of the protecting group at the focal point and generational growth.

Compound **9** was reacted with 2-bromo-propionyl bromide to intall four α-bromo esters on building block **10**. Importantly, this step in the synthetic sequence was the first to require column chromatography for purification. Removal of the carboxylic acid focal point protecting group was easily achieved by reacting compounded **10** with 1,8-diazabicycloundec-7-ene for 10 minutes while monitoring by TLC. The methylene protons beta to the ester focal point and alpha to the sulfonyl group are very acidic. DBU deprotonates **10** and initiates an elimination reaction creating an alkene and eliminating the

carboxylate. Crude NMR showed the formation of new alkene protons and disappearance of the methylene protons. Column chromatography was used to separate the byproduct from **11**. No elimination was observed on the α-bromo esters on compound **11** for short reaction times, however longer reactions (24 hours) did show evidence of elimination at the α-bromo esters. The target compound, **12**, was achieved by converting to **11** to an acid chloride with the previous conditions and esterification to dihydroxyspiropyran. Purification by column chromatography of **12** proved to be the most difficult of initiators **1**, **3**, and **12**. Monofunctionalized spiropyrans are always present in these esterfications reactions and column chromatography has proved to be the best method for separating the products from monofunctionalized intermediates. However, the R_f value of the product **12** and monofunctionalized by-intermediate and even **11** (which is present after aqueous work up) are close enough to pose a challenge in purification. Any small impurities in the initiator result in bimodal peaks as evidenced by GPC when used in polymerization reactions. Additionally, GPC was a useful source to determine if the monofunctionalized by-product or **11** were present in the sample as these peaks were almost fully resolved from **12** due to the different sizes of the structures.

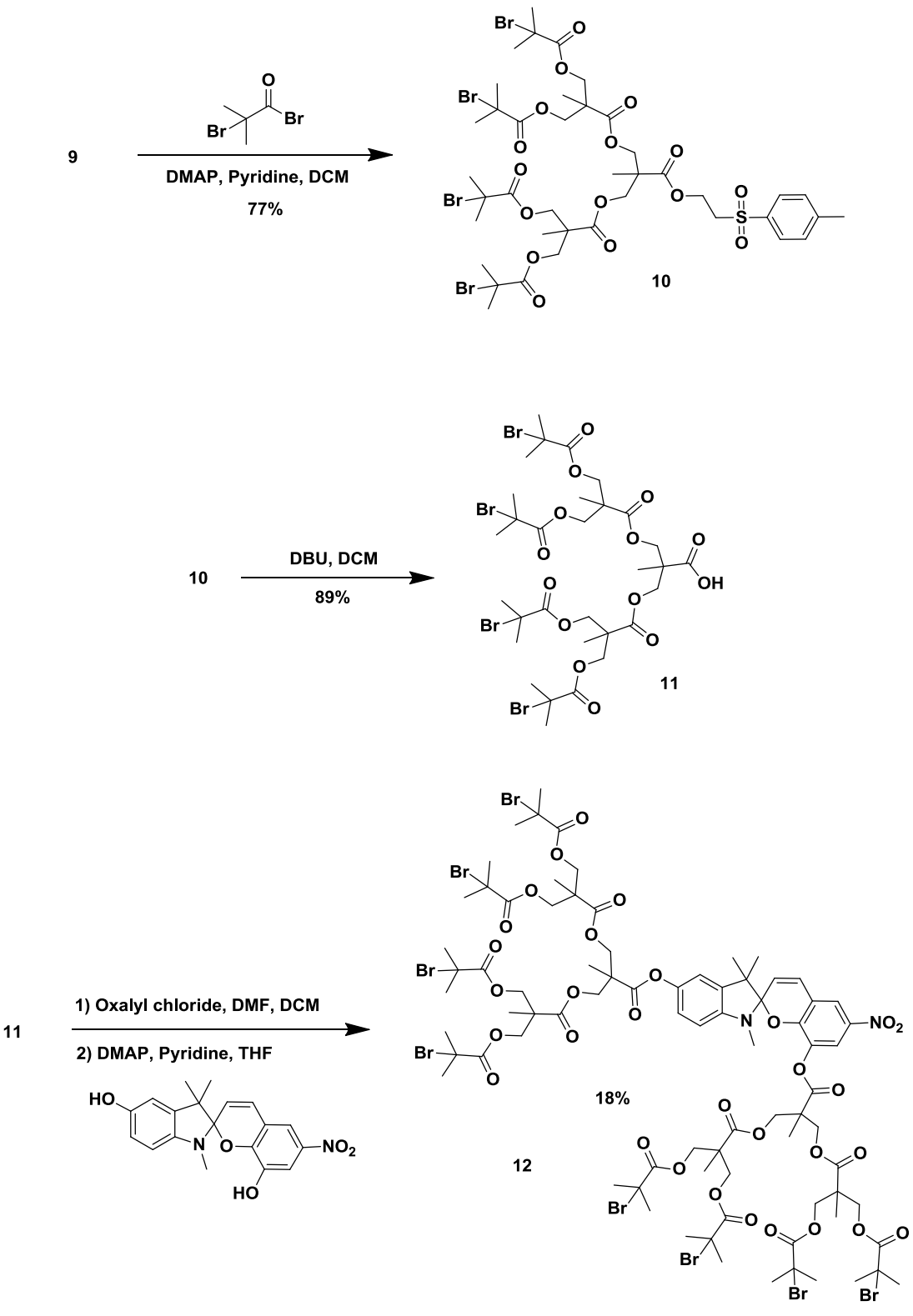

Scheme 2.4 Synthetic steps to introduce α-bromo esters, remove the protecting group, and functionalization of the spiropyran.

2.2.3 Branched Control Initiator

A control polymer with a branched structure was also desired for subsequent testing. The initiator to create this type of control polymer was achieved by esterification of a monohydroxy spiropyran[1.2.7] and **11** under standard conditions.

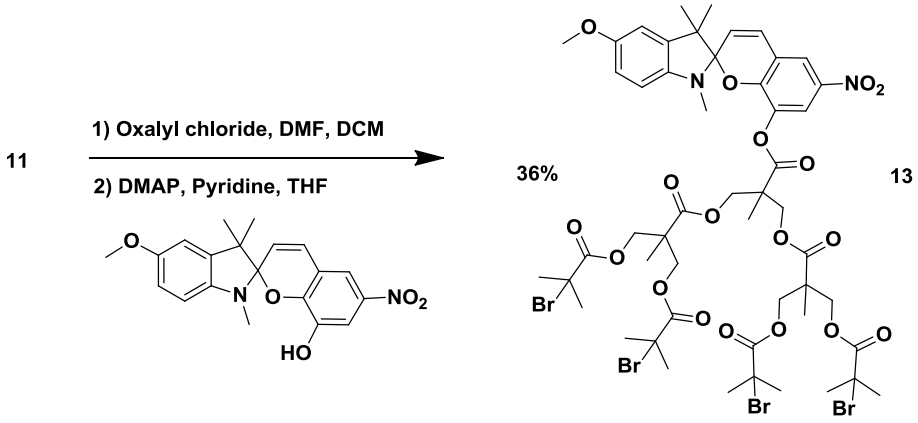

Scheme 2.5 Synthesis of branched control **13**.

2.3 Carboxylic acid functionalized spiropyrans

2.3.1 Mechanophore

Spiropyrans containing carboxylic acid functionality were targeted as they are amenable to surface functionalization of amine-functionalized silica.[20-22] Furthermore, a functional group capable of polymerization was targeted to embed a spiropyran at the interface between glass fiber and matrix. Here, a spiropyran containing carboxylic acid and methacrylate functional groups with identical attachment points (5′ and 8 positions) was desired. Spiropyrans with carboxylic acids at the 5′ position are known,[23,24] therefore a methacrylate was chosen to be placed at the 8 position. The 8 position has previously been functionalized with methacrylates by our group.[2,4] Starting from 4-hydrazinylbenzoic acid hydrochloride, **14** was prepared under standard indole synthesis.[23] Methylation of **14** was achieved by similar procedure reported by Potisek.[1] Condensation of **15** with 2,3-dihydroxy-5-nitrobenzaldehyde[1,2,7] gave spiropyran **16** in 58% yield. An unusual method of esterification was adopted to selectively functionalize the hydroxyl group at position 8. **16** was stirred in the presence of methacrylic anhydride for 24 hours which, presumably, formed and ester at position 8 and an anhydride at the 5′ position (as evidenced by TLC). The polar functional groups (hydroxyl and carboxylic acid) cause the compounds to run much slower on

silica and after the first step the major spot on the TLC plate was a non-polar compound, giving evidence that both sites had been functionalized. After 24 hours, de-ionized H_2O and DMAP were introduced to hydrolyze the presumed anhydride at the 5′ position which resulted in disappearance of the non-polar spot on TLC and a new spot of higher polarity which ran slower on the TLC plate. After work up and column chromatography **17** was achieved in 33% yield.

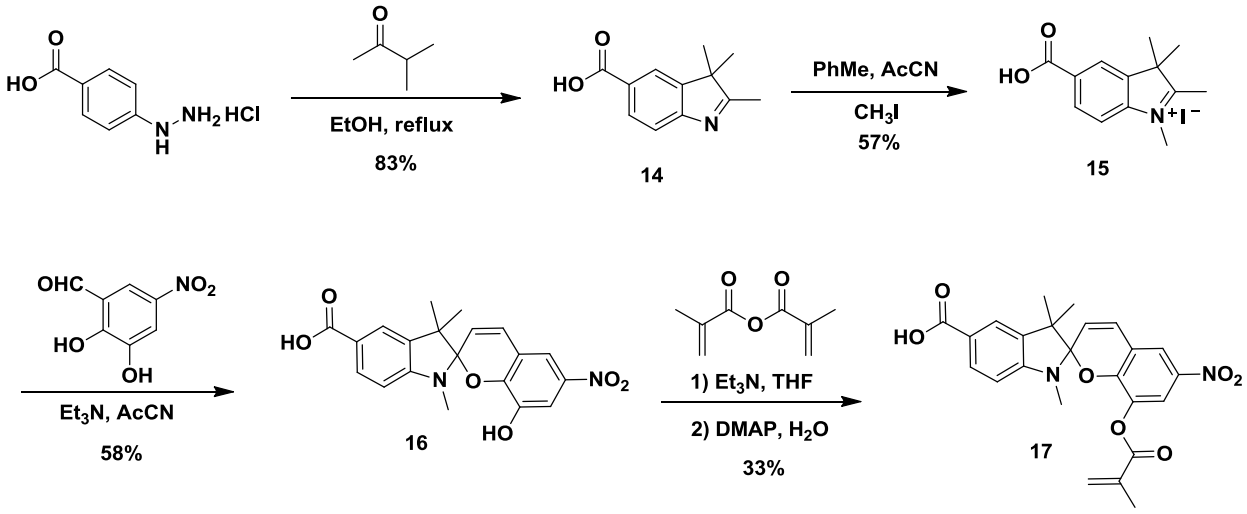

Scheme 2.6. Synthesis of spiropyran **17** which contains a contains a carboxylic acid for fiber functionalization and a methacrylate for incorporation into PMMA.

2.3.2 Control

A control compound was also targeted to be amenable for solid state testing. Here, a spiropyran capable of covalently attaching to the surface of a glass fiber but lacking the functionality to covalently bond to the matrix was targeted. Accordingly, the methacrylate functional group was deleted from the structure to achieve **18**.[23,24]

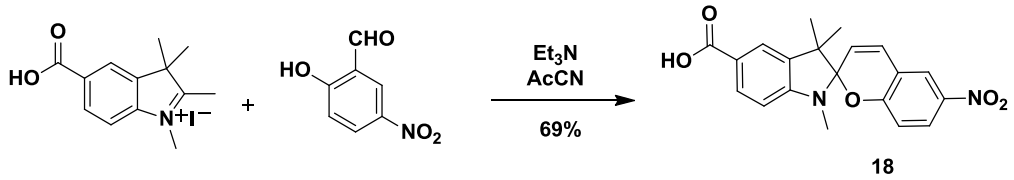

Scheme 2.7. Synthesis of control spiropyran **18** which contains a carboxylic acid for fiber functionalization but lacks a methacrylate group for excluding incorporation into PMMA.

2.4 Conclusions

All targeted spiropyrans were achieved for incorporation into polymers. The tetra-functional initiator was achieved in significantly fewer steps (2) than the octafunctional initiator (9). However, only three of the nine synthetic steps in the octa-functional initiator required column chromatography purification.

Carboxylic acid functionalized spiropyrans containing a polymerizable methacrylate were achieved for use in interfacial activation studies.

2.5 Synthetic procedures

2.5.1 General Procedures

Unless otherwise stated, all starting materials were obtained from commercial suppliers and used without purification.. Dry dichloromethane and THF were obtained from an Anhydrous Engineering Solvent Delivery System (SDS) equipped with activated alumina columns. All reactions were performed under a N2 atmosphere unless otherwise specified.

Flash column chromatography was conducted with silica gel 60 (230-400 mesh) from Silicycle. Melting points were obtained using an electrothermal melting temperature apparatus (Mel-Temp, Model 1001). 1H and 13C NMR spectra were obtained using either a Varian 400 or 500 MHz spectrometer in the VOICE NMR laboratory at the University of Illinois; the residual solvent
protons were used to reference the chemical shift. Coupling constants (*J*) are reported in Hertz (Hz), and splitting patterns are designated as s (singlet), d (doublet), t (triplet), q (quartet), m (multiplet), and br (broad).

Mass spectra were obtained through the Mass Spectrometry Facility, SCS, University of Illinois and elemental analyses were performed by the University of Illinois MicroAnalytical services.

2.5.2 Synthetic Details

Synthesis of 3-((2-bromo-2-methylpropanoyl)oxy)-2-(((2-bromo-2-methylpropanoyl)oxy)methyl)-2-methylpropanoic acid[13]

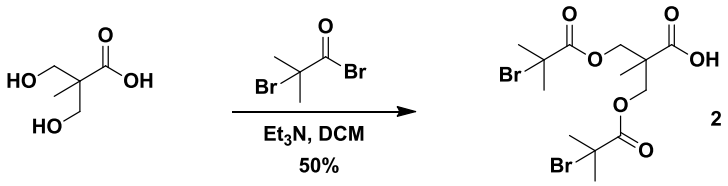

Bis(hydroxymethyl)propionic acid (bis-MPA) (5.00 g, 37.3 mmol, 1 equiv), and triethylamine (13.0 mL, 91.0 mmol) was added to 125 mL of dry CH_2Cl_2 at 0 °C under a nitrogen atmosphere. 2-Bromo-2-methylpropionyl bromide (11.0 mL, 89.0 mmol, 2.39 equiv) was added dropwise via a syringe pump over 30 min. After stirring at 0 °C for 1 h, the reaction turned from colorless to yellow. The reaction was allowed to warm to rt and stir overnight. After evaporation of the solvent, the residue was dissolved in 100 mL of diethyl ether and the triethylamine hydrochloride was filtered off. The filtrate was then extracted with 2 N hydrochloride (3 x 100 mL). The ether layer was dried with $MgSO_4$, filtered and evaporated to dryness. The crude product was purified by column chromatography eluting with 10% MeOH in CH_2Cl_2. The crude product was recrystallized from hexane to give the product as a white solid: 7.24 g (49%).

^{1}H NMR (400 MHz, $CDCl_3$): **δ** 4.40 (m, 4H). 1.92 (s, 12H), 1.39 (s, 3H).

$^{13}C\{^1H\}$ NMR (125 MHz, $CDCl_3$): **δ** 178.57, 170.96, 65.97, 55.21, 46.6, 30.6, 17.8.

LRMS-ESI (*m*/*z*): $[M]^-$ calcd for $C_{13}H_{19}Br_2O_6$, 431.09; found, 431.1.

MP: 96-97 °C.

Synthesis of (((1',3',3'-trimethyl-6-nitrospiro[chromene-2,2'-indoline]-5',8-diyl)bis(oxy))bis(carbonyl))bis(2-methylpropane-3,2,1-triyl) tetrakis(2-bromo-2-methylpropanoate)

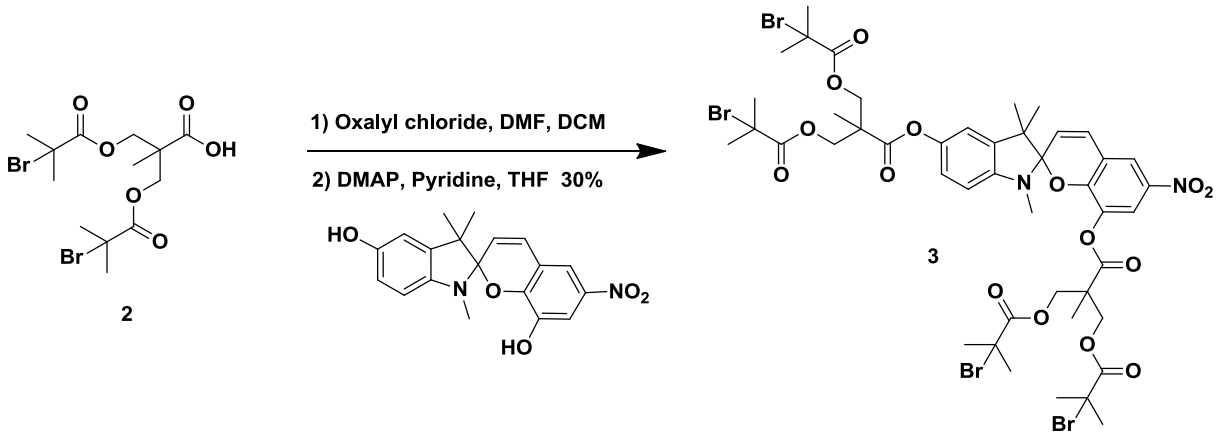

The carboxylic acid (750 mg, 1.74 mmol, 1 equiv) was dissolved in 7 mL of dry CH_2Cl_2. Oxalyl chloride (303µL, 3.47 mmol, 2 equiv) was added dropwise to the solution. One drop of DMF was added to the solution which initiated the evolution of bubbles. The solution stirred at rt for 4 h. The solution was evaporated by rotary evaporation followed by successive additions of 7 mL of 1,2-dichloroethane and evaporation to remove excess oxalyl chloride. In a separate flask, the dihydroxy spiropyran (204 mg, 0.577 mmol, 0.33 equiv) was first partially dissolved in 2.5 mL of pyridine then diluted with 3 mL of dry THF. 4-dimethylaminopyridine (DMAP) (33 mg, 0.251 mmol, 0.15 equiv) was added and the mixture was cooled to 0 °C. The acid chloride was dissolved in 5 mL of dry THF and added dropwise to the solution which caused a color change from blue to purple. The rxn was allowed to warm to rt and stir overnight. The solution was evaporated and dissolved in 75 mL of CH_2Cl_2. The solution was washed with 1 M $NaHSO_4$ (3 x 75 mL), followed by sat. aqueous Na_2CO_3 (2 x 75 mL), and finally with brine (1 x 75 mL). The organic layer was dried with Na_2SO_4, filtered, and evaporated to dryness. The product was purified by column chromatography eluting with 1% MeOH in CH_2Cl_2. The product was obtained as a purple foam with turned yellow over time: 321 mg (36%).

^{1}H NMR (400 MHz, $CDCl_3$): **δ** 7.97 (d, J = 2.7 Hz, 1H), 7.88 (d, J = 2.7 Hz, 1H), 7.00 (d, J = 10.5 Hz, 1H), 6.85 (dd, J = 2.4 Hz, J = 8.3 Hz, 1H), 6.81 (d, J = 2.4 Hz, 1H), 6.51 (d, J = 8.3 Hz, 1H), 5.92 (d, J = 10.5 Hz, 1H), 4.5-4.0 (m, 8H), 2.68 (s, 3H)**,** 1.93 (m, 24 H), 1.47 (s, 3H), 1.25(s, 3H), 1.20 (s, 3H), 1.15 (s, 3H)**,** 0.76 (s, 3H).

^{13}C{^{1}H} NMR (125 MHz, $CDCl_3$): **δ** 171.56, 171.19, 171.07, 169.81, 150.93, 145.68, 144.30, 140.47, 137.58, 136.91, 128.84, 121.12, 120.63, 120.62, 199.74, 199.46, 155.68, 108.04, 107.66, 66.61,65.76, 65.54, 55.68, 55.58, 55.49, 52.08, 47.16, 46.79, 30.93, 30.88, 30.86, 30.84 29.00, 25.98, 19.59, 18.14, 17.29.

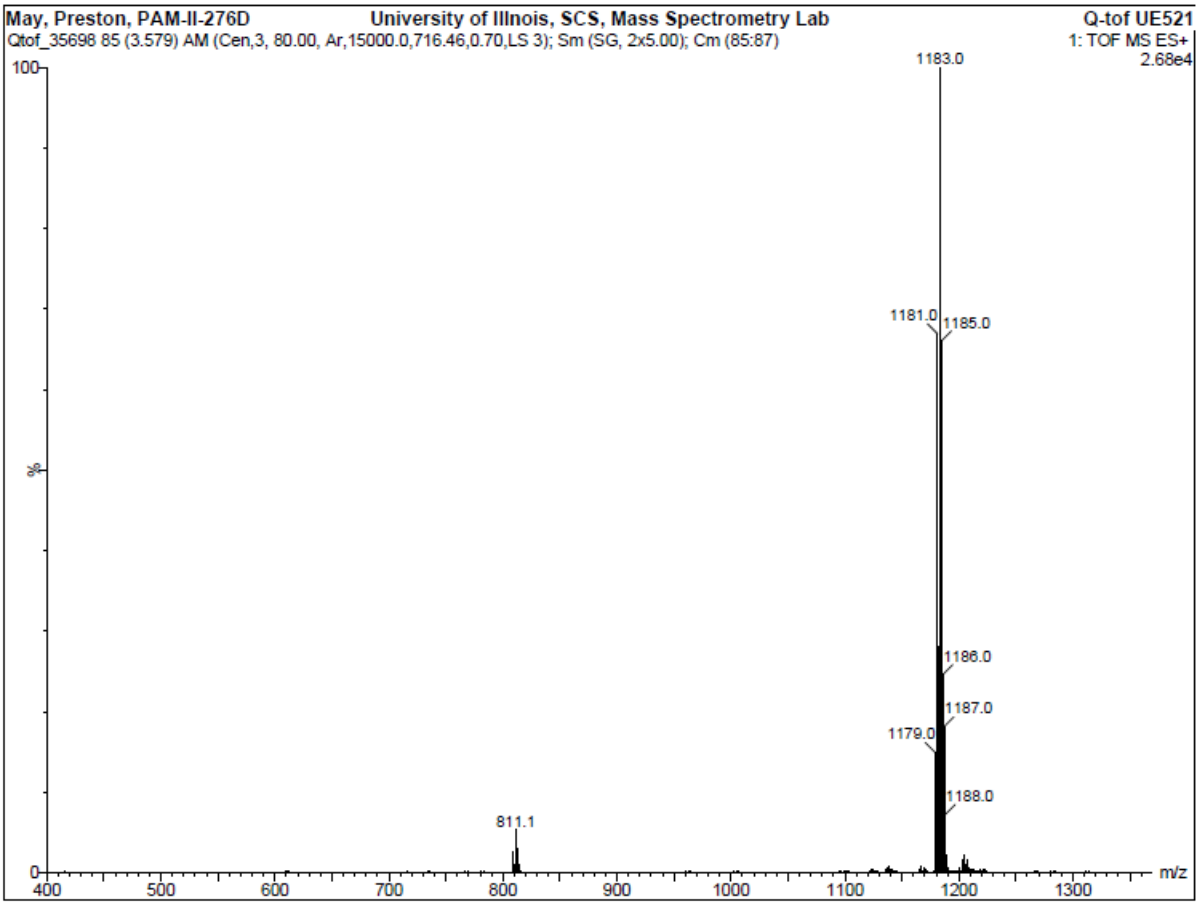

Figure 2.3. LRMS-ESI (*m*/*z*): $[M + H]^+$ calcd for $C_{45}H_{55}Br_4N_2O_{15}$,1183.03.

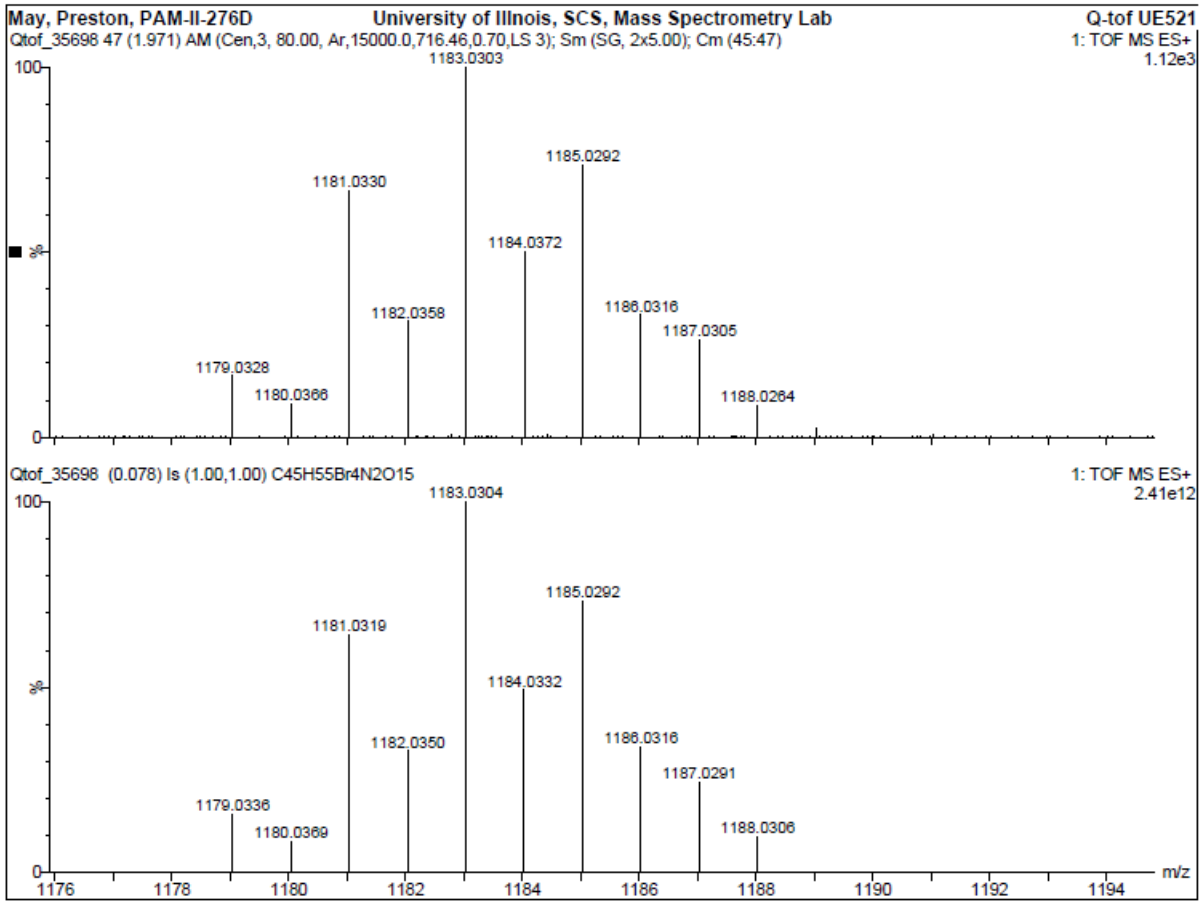

Figure 2.4. HRMS-ESI (*m*/*z*): $[M + H]^+$ calcd for $C_{45}H_{55}Br_4N_2O_{15}$,1183.0290.

Synthesis of 5-methyl-2-phenyl-1,3-dioxane-5-carboxylic acid[17]

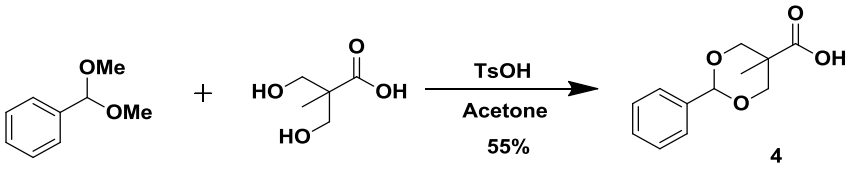

4

2,2-Bis(hydroxymethyl)-propionic acid (10.0 g, 74.5 mmol, 1 equiv), benzaldehyde dimethyl acetal (16.7 mL, 111 mmol, 1.5 equiv), and *p*-toluenesulfonic acid monohydrate (TsOH) (703 mg, 3.7 mmol, 0.05 equiv) were mixed in 75 mL of acetone. The reaction mixture was stirred for 4 h at room temperature. After storage of the reaction mixture in the refrigerator overnight, the solids were filtered off and washed with cold acetone to give the product as white crystals: 8.70 g (52%).

^{1}H NMR (400 MHz, $CDCl_3$): **δ** 7.47 (m, 2H), 7.35 (m, 3H), 5.49 (s, 1H), 4.63 (d, *J* = 11.4 Hz, 2H), 3.70 (d, *J* = 11.4 Hz, 2H), 1.11 (s, 3H).
^{13}C{^{1}H} NMR (125 MHz, $CDCl_3$): **δ** 175.58, 138.39, 128.70, 128.01, 126.10, 100.37, 72.65, 41.58, 17.58.
LRMS-FD (*m*/*z*): [M]+ calcd for $C_{12}H_{14}O_4$, 222.09; found, 222.2.

Synthesis of 5-methyl-2-phenyl-1,3-dioxane-5-carboxylic anhydride[17]

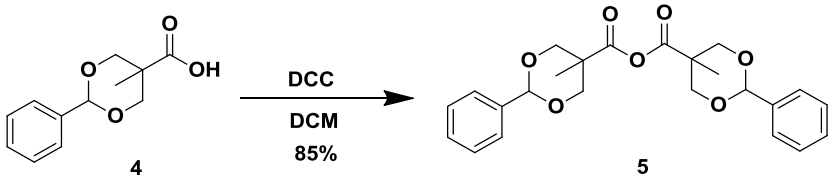

The carboxylic acid (8.70 g, 39.2 mmol, 1 equiv) and *N*,*N*¢-dicyclohexylcarbodiimide (DCC) (4.04 g, 19.6 mmol, 0.5 equiv) of were mixed in 150 mL of CH_2Cl_2. The reaction mixture was stirred overnight at room temperature. The dicyclohexyl urea byproduct (DCU) was filtered off and washed with a small volume of CH_2Cl_2. The crude product was purified by precipitating the filtrate into 500 mL of hexane under vigorous stirring. After filtration, the product was isolated as a white solid: 7.55 g (90%).
^{1}H NMR (400 MHz, $CDCl_3$): **δ** 7.45 (m, 4H), 7.33 (m, 6H), 5.47 (s, 2H), 4.66 (d, *J* = 11.4 Hz, 4H), 3.69 (d, *J* = 11.4 Hz, 4H), 1.12 (s, 6H).
^{13}C{^{1}H} NMR (125 MHz, $CDCl_3$): **δ** 169.12, 137.56, 129.09, 128.22, 126.27, 102.11, 73.17, 44.18, 16.85.
LRMS-FD (*m*/*z*): [M]+ calcd for $C_{24}H_{26}O_7$, 426.17; found, 426.3.

Synthesis of 2-tosylethyl 5-methyl-2-phenyl-1,3-dioxane-5-carboxylate[19]

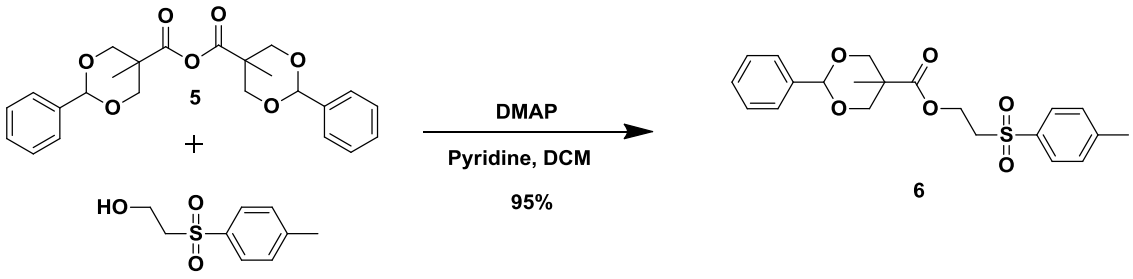

To a flame-dried round-bottom flask equipped with a magnetic stir bar (under nitrogen atmosphere), the benzylidene protected anhydride (7.31 g, 17.15 mmol, 2 equiv), para-toluene sulfonyl ethanol (1.71 g, 8.57 mmol, 1 equiv) and DMAP (548 mg, 4.29 mmol, 0.5 equiv) were all dissolved in 22

mL of pyridine and 45 mL CH_2Cl_2. After stirring at rt overnight approximately 2 mL of water was added and the reaction was stirred for an additional 24 h in order to quench the excess anhydride. The product was isolated by diluting the mixture with CH_2Cl_2 (150 mL) and washing with 1 M NaHSO4 (3x 150 mL), followed by saturated aqueous Na_2CO_3 (2 × 150 mL), and finally with brine (1 x 150 mL). The organic layer was evaporated to dryness and the product was then precipitated three times from 10 % ethyl acetate in hexanes. The precipitate was filtered to yield a white solid 3.46 g, (95%).

^{1}H NMR (400 MHz, $CDCl_3$): **δ** 7.80 (d, *J* = 8.0 Hz, 2H), 7.40 (m, 2H), 7.33 (m, 5H), 5.42 (s, 1H), 4.53 (d, *J* = 11.4 Hz, 2H), 4.48 (t, *J* = 6.3 Hz, 2H), 3.60 (d, *J* = 11.4 Hz, 2H), 3.46 (t, *J* = 6.3 Hz, 2H), 2.43 (s, 3H), 0.96 (s, 3H).

^{13}C{^{1}H} NMR (125 MHz, $CDCl_3$): **δ** 173.03. 144.63, 137.27, 135.55, 129.61, 128.53, 127.75, 127.72, 125.67, 101.25, 72.85, 57.72, 54.66, 41.98, 21.15, 17.04.

LRMS-FD (*m*/*z*): [M]+ calcd for $C_{21}H_{24}O_6S$, 404.13; found, 404.1.

Synthesis of 2-tosylethyl 3-hydroxy-2-(hydroxymethyl)-2-methylpropanoate[19]

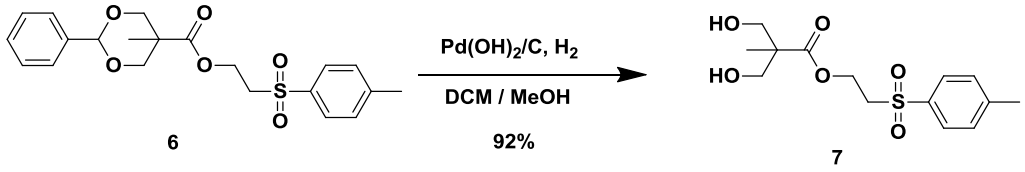

To a schlenk flask equipped with a balloon in the neck, the benzylidene protected starting material (3.30 g, 8.16 mmol) was dissolved in 125 mL of a 1:1 mixture of CH_2Cl_2 : MeOH (v/v). Pd(OH)2 on Carbon (20%) (300 mg) was added and the flask was evacuated and back-filled with hydrogen three times. After vigorous stirring for 24 h under balloon pressure, the reaction mixture was filtered through a celite plug in a fritted glass funnel and the filtrate was evaporated to dryness on a rotary evaporator to yield a white solid: 2.31 g (91%).

^{1}H NMR (400 MHz, CD_3OD): **δ** 7.82 (d, J = 8.4 Hz, 2H), 7.47 (d, J = 8.4 Hz, 2H), 4.39 (t, *J* = 5.8 Hz, 2H), 3.59 (t, *J* = 5.8 Hz, 2H), 3.50 (dd, *J* = 11.0 Hz, J = 31.9, 4H), 2.46 (s, 3H), 1.01 (s, 3H),

^{13}C{^{1}H} NMR (125 MHz, CD_3OD): δ 175.86, 146.68, 137.74, 131.19, 129.27, 65.65, 58.90, 55.88, 51.55, 21.57, 17.04.

LRMS-FD (*m*/*z*): [M]+ calcd for $C_{14}H_{20}O_6S$, 316.10; found, 316.1.

Synthesis of 2-methyl-2-((2-tosylethoxy)carbonyl)propane-1,3-diyl bis(5-methyl-2-phenyl-1,3-dioxane-5-carboxylate)[19]

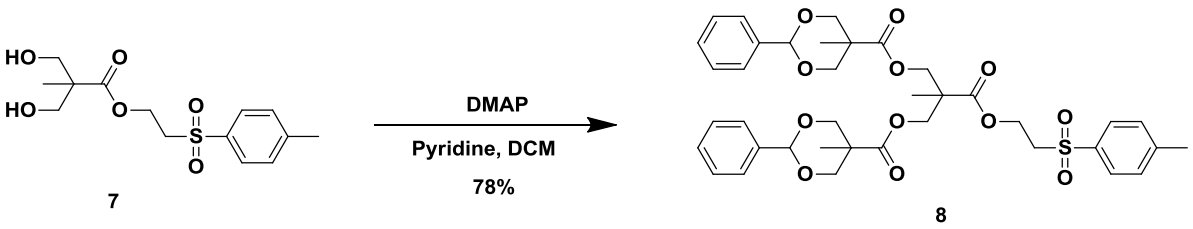

To a flame-dried round-bottom flask equipped with a magnetic stir bar (under nitrogen atmosphere), the benzylidene protected anhydride (12.3 g, 29.1 mmol, 4 equiv), the diol (2.30 g, 7.26 mmol, 1 equiv) and DMAP (558 mg, 4.35 mmol, 0.6 equiv) were all dissolved in 25 mL of pyridine and 50 mL CH_2Cl_2. After stirring at rt overnight approximately 5 mL of water was added and the reaction was stirred for an additional 24 h in order to quench the excess anhydride. The product was isolated by diluting the mixture with CH_2Cl_2 (200 mL) and washing with 1 M NaHSO4 (3x 200 mL), followed by saturated aqueous Na_2CO_3 (2 × 200 mL), and finally with brine (1 x 200 mL). The organic layer was evaporated to dryness and the product was then precipitated three times from hexanes. The precipitate was filtered to yield a white solid: 4.89 g, (93%).

^{1}H NMR (400 MHz, $CDCl_3$): **δ** 7.68 (d, J= 8.2 Hz, 2H). 7.40 (m, 4H), 7.32 (m, 8H), 5.41 (s, 2H), 4.56 (m, 4H), 4.20 (m, 6H), 3.61 (d, *J* = 11.6 Hz, 4H) 3.10 (t, *J* = 6 Hz, 2H), 2.38 (s, 3H), 1.08 (s, 3H), 0.96 (s, 6H).

^{13}C{^{1}H} NMR (125 MHz $CDCl_3$,): **δ** 172.72. 171.56, 144.56, 137.31, 135.81, 129.55, 128.46, 127.71, 127.59, 125.66, 101.17, 73.07, 73.00, 64.74, 57.86, 54.17, 46.23, 42.14, 21.10, 17.27, 16.87.

LRMS-FD (*m*/*z*): [M]+ calcd for $C_{38}H_{44}O_{12}S$, 724.26; found, 724.3.

Synthesis of 2-methyl-2-((2-tosylethoxy)carbonyl)propane-1,3-diyl bis(3-hydroxy-2-(hydroxymethyl)-2-methylpropanoate)[19]

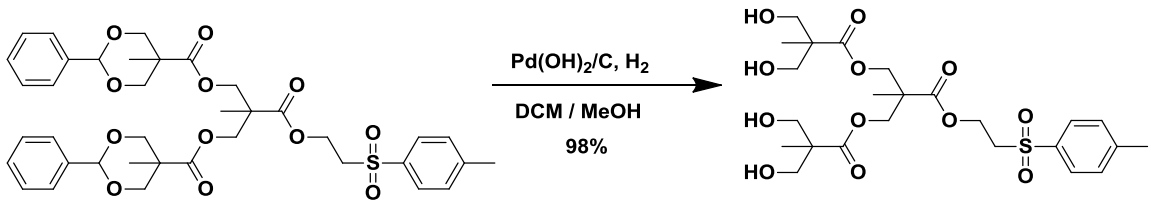

8 9

To a schlenk flask equipped with a balloon in the neck, the benzylidene protected starting material (3.4 g, 4.69 mmol) was dissolved in 125 mL of a 1:1 mixture of CH_2Cl_2 : MeOH (v/v). Pd(OH)2 on Carbon (20%) (160 mg) was added and the flask was evacuated and back-filled with hydrogen three times. After vigorous stirring for 24 h under balloon pressure, the reaction mixture was filtered through a celite plug in a fritted glass funnel and the filtrate was evaporated to dryness on a rotary evaporator to yield a white solid: 2.33g (91%)

^{1}H NMR (400 MHz, CD_3OD): **δ** 7.82 (d, *J* = 8.2 Hz, 2H). 7.47 (d, *J* = 8.2 Hz, 2H), 4.43 (t, *J* = 5.7 Hz, 2H), 4.09 (dd, *J* = 11.0 Hz, J = 20.2 Hz, 4H), 3.64 (dd, J = 1.8 Hz, J = 10.7 Hz, 4H), 3.60 (t, *J* = 5.7 Hz, 2H), 3.56 (d, J = 10.7 Hz, 4H), 2.46 (s, 3H), 1.12 (s, 9H).

^{13}C{^{1}H} NMR (125 MHz, CD_3OD): **δ** = 173.94, 171.81, 144.82, 136.02, 129.41, 127.40, 64.25, 63.95, 57.75, 53.92, 49.91, 45.76, 19.72, 15.94, 15.38.

LRMS-ESI (*m*/*z*): [M + H]+ calcd for $C_{24}H_{37}O_{12}S$, 549.20; found, 549.4

Synthesis of (((2-methyl-2-((2-tosylethoxy)carbonyl)propane-1,3-diyl)bis(oxy))bis(carbonyl))bis(2-methylpropane-3,2,1-triyl) tetrakis(2-bromo-2-methylpropanoate)

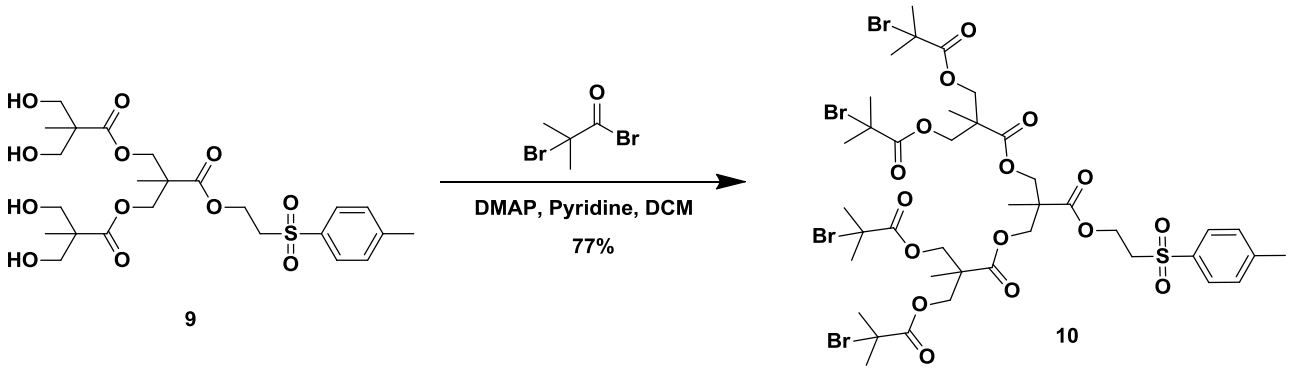

The tetraol (1.00 g, 1.82 mmol, 1 equiv), and DMAP (116 mg, 0.910 mmol, 0.5 equiv) was added to 18 mL of dry CH_2Cl_2 and 9 mL of pyridine at 0 °C under a nitrogen atmosphere. 2-Bromo-2-methylpropionyl bromide (1.35 mL, 10.92 mmol, 6 equiv) was added dropwise. After stirring at 0 °C for 1 h, the reaction turned from colorless to yellow. The reaction was allowed to warm to rt and stir overnight. The reaction mixture was diluted with CH_2Cl_2 (100 mL) and washed with 1 M NaHSO4 (3x 100 mL), followed by saturated aqueous Na_2CO_3 (3 × 100 mL), and finally with brine (1 x 100 mL). The organic layer was collected, dried with $MgSO_4$, filtered, and evaporated to dryness. The product was purified by column chromatography eluting with a gradient starting with CH_2Cl_2 and increasing polarity to 5% EtOAc in CH_2Cl_2. The fractions containing the product were evaporated to dryness, redissolved in CH_2Cl_2 and precipitated in hexanes to give a white solid: 1.61 g, (77%).

^{1}H NMR (400 MHz, $CDCl_3$): **δ** 7.81 (d, J = 8.4 Hz, 2H), 7.39 (d, 8.4 Hz, 2H), 4.49 (t, J = 6.0 Hz, 2H), 4.38 (d, J = 11.0 Hz, 4H), 4.285 (dd, J = 5.0 Hz, J = 11.0 Hz, 4H), 4.22 (m, 4H), 3.46 (t, J = 6.0 Hz, 2H), 2.46 (s, 3H), 1.91 (s, 24H), 1.32 (s, 6H), 1.20 (s, 3H).

^{13}C{^{1}H} NMR (125 MHz $CDCl_3$,): **δ** 175.9, 171.5, 171.3, 139.4, 135.9, 130.0, 128.2, 67.2, 66.2, 63.4, 60.3, 51.4, 41.3, 40.7, 33.6, 21.3, , 16. 3, 15.4

LRMS-ESI (*m*/*z*): [M + Na]+ calcd for $C_{40}H_{56}NaO_{16}S$, 1167.53; found, 1166.4

.Synthesis of 3-((3-((2-bromo-2-methylpropanoyl)oxy)-2-(((2-bromo-2-methylpropanoyl)oxy)methyl)-2-methylpropanoyl)oxy)-2-(((3-((2-bromo-2-methylpropanoyl)oxy)-2-(((2-bromo-2-methylpropanoyl)oxy)methyl)-2-methylpropanoyl)oxy)methyl)-2-methylpropanoic acid

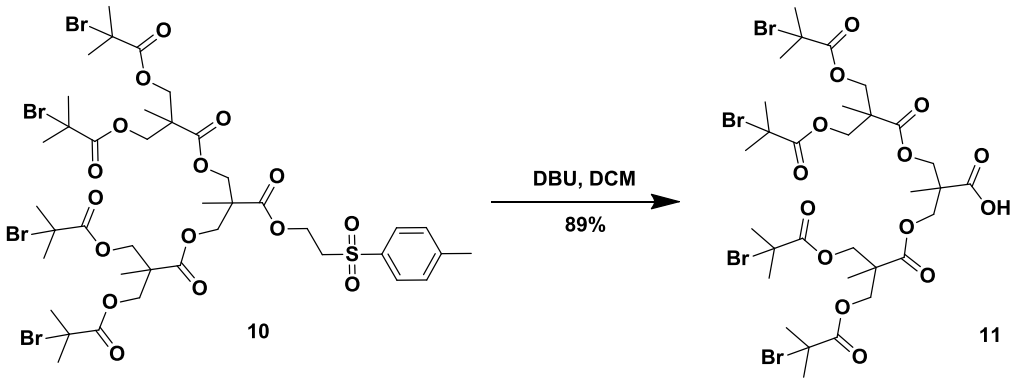

The initiator functionalized Dendron (163 mg, 0.142 mmol, 1 equiv) was dissolved in 1.5 mL of CH_2Cl_2. 1,8- diazabicyclo[5.4.0]undec-7-ene (DBU) (43 μL, 0.285 mmol, 2 equiv) was added. The reaction was stirred for 15 min. The reaction mixture was diluted with 25 mL CH_2Cl_2 and washed with 1 M NaHSO4 (1x 25 mL). The organic layer was dried with $MgSO_4$, filtered, and evaoporated to dryness. The product was purified by column chromatography eluting with a gradient starting with CH_2Cl_2 and increasing polarity to 10% EtOAc in CH_2Cl_2. The fractions containing the product were evaporated to dryness, redissolved in CH_2Cl_2 and precipitated in hexanes to give a white solid: 105 mg, (89%).

^{1}H NMR (400 MHz, $CDCl_3$): **δ** 4.3-4.4 (m, 12H), 1.91 (s, 24H), 1.34 (m, 9H).

$^{13}C\{^1H\}$ NMR (125 MHz, $CDCl_3$): **δ** = 177.2, 171.8, 171.5, 66.17, 66.15, 65.99, 55.46, 46.91, 46.48, 30.733, 17.96, 17.78

LRMS-ESI (*m*/*z*): $[M - H]^-$ calcd for $C_{31}H_{45}O_{14}$, 961.30; found, 961.30

Synthesis of ((((((1',3',3'-trimethyl-6-nitrospiro[chromene-2,2'-indoline]-5',8-diyl)bis(oxy))bis(carbonyl))bis(2-methylpropane-3,2,1-triyl))tetrakis(oxy))tetrakis(carbonyl))tetrakis(2-methylpropane-3,2,1-triyl) octakis(2-bromo-2-methylpropanoate)

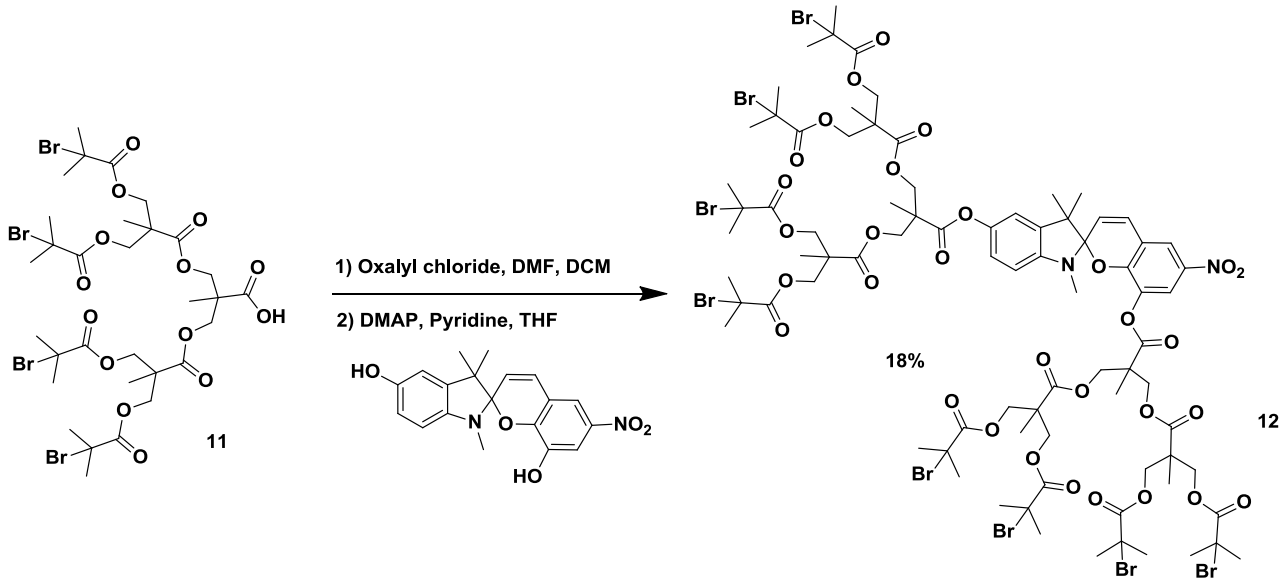

The carboxylic acid (286 mg, 0.292 mmol, 1 equiv) was dissolved in 3 mL of dry CH_2Cl_2. Oxalyl chloride (76 µL, 0.876 mmol, 3 equiv) was added dropwise to the solution. One drop of DMF was added to the solution which initiated the evolution of bubbles. The solution stirred at rt for 4 h. The solution was evaporated by rotary evaporation followed by successive additions of 3 mL of 1,2-dichloroethane and evaporation to remove excess oxalyl chloride. In a separate flask, the dihydroxy spiropyran (34 mg, 0.0964 mmol, 0.33 equiv) was first partially dissolved in 0.5 mL of pyridine then diluted with 0.5 mL of dry THF. DMAP (5 mg, 0.044 mmol, 0.15 equiv) was added and the mixture was cooled to 0 °C. The acid chloride was dissolved in 2 mL of dry THF and added dropwise to the solution which caused a color change from blue to purple. The reaction was allowed to warm to rt and stir overnight. The solution was evaporated and dissolved in 50 mL of CH_2Cl_2. The solution was washed with 1 M $NaHSO_4$ (3 x 50 mL), followed by sat. aqueous Na_2CO_3 (2 x 50 mL), and finally with brine (1 x 50 mL). The organic layer was dried with Na_2SO_4, filtered, and evaporated to dryness. The product was purified by column chromatography eluting with 1% MeOH in CH_2Cl_2. The product was obtained as a purple foam with turned yellow over time: 39 mg (18%)

^{1}H NMR (400 MHz, $CDCl_3$): 7.97 (d, J = 2.6 Hz, 1H), 7.88 (d, J = 2.6 Hz, 1H), 6.99 (d, J = 10.4 Hz, 1H), 6.805 (dd, J = 2.1 Hz, J = 8.2 Hz, 1H), 6.78 (d, J = 2.1 Hz, 1H), 6.49 (d, J = 8.2 Hz, 1H), 5.91 (d, J = 10.4 Hz, 1H), 4.0-4.5 (m, 24H), 2.67 (s, 3H), 1.90 (m, 48H), 1.55 (s, 3H), 1.44 (s, 3H), 1.34 (m, 9H), 1.26 (s, 3H), 1.22 (s, 3H), 0.67 (s, 3H)

$^{13}C\{^{1}H\}$ NMR (125 MHz, $CDCl_3$) **δ** 171.82, 171.80, 171.64, 171.61, 171.45, 171.04, 170.98, 169.58, 150.75, 145.66, 144.18, 140.43, 137.59, 136.83, 128.67, 121. 18, 120.55, 120.48, 119.62, 199.31, 155.53, 108.02, 107.53, 66.16, 66.09, 66.02, 65.94, 65.11, 64.88, 55.60, 55.58, 55.57, 55.51, 55.47, 52.16, 47.05, 46.99, 46.95, 46.91, 46.67, 30.77, 29.83, 28.94, 19.42, 18.13, 18.03, 17.20

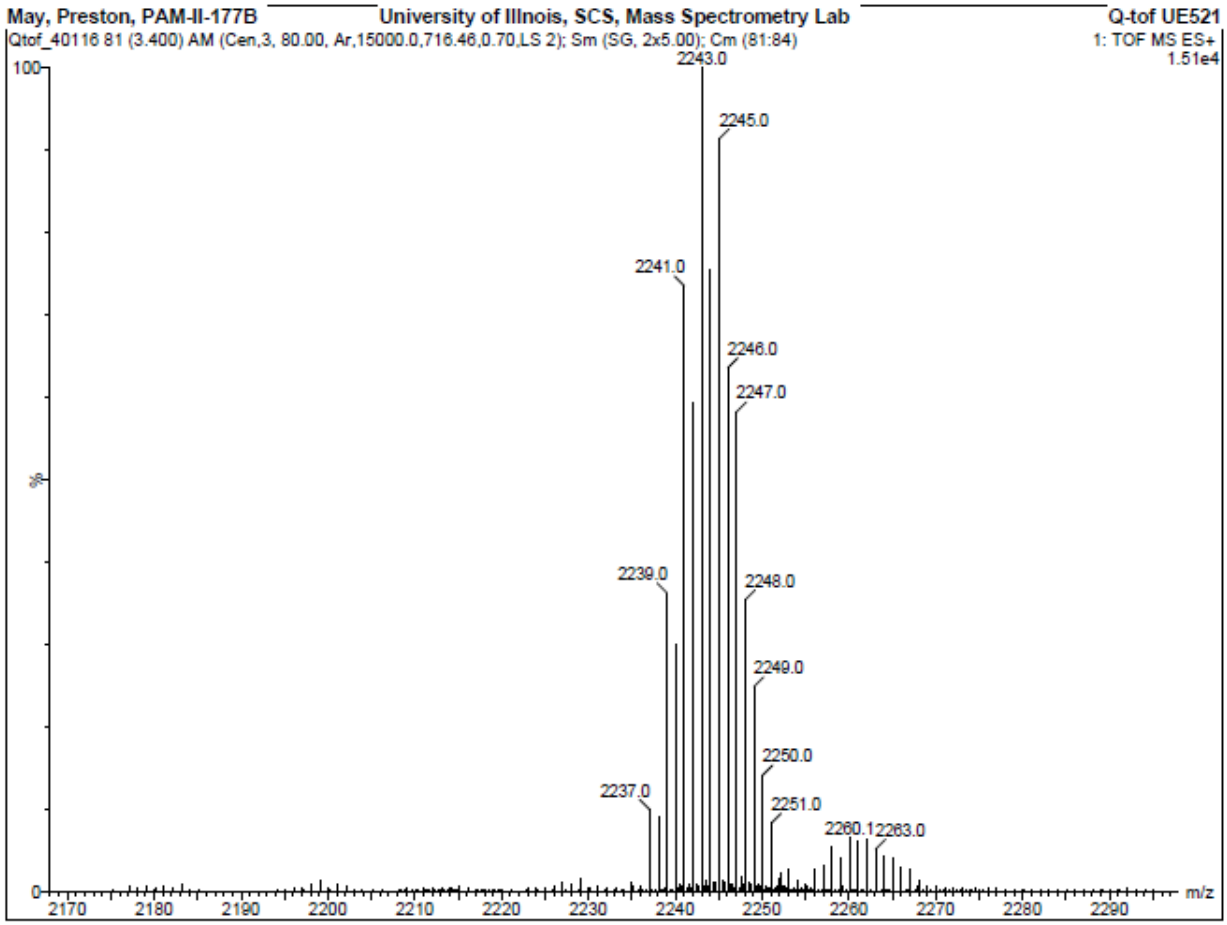

Figure 2.5. LRMS-ESI (*m*/*z*): $[M + H]^+$ calcd for $C_{81}H_{107}Br_8N_2O_{31}$, 2243.02.

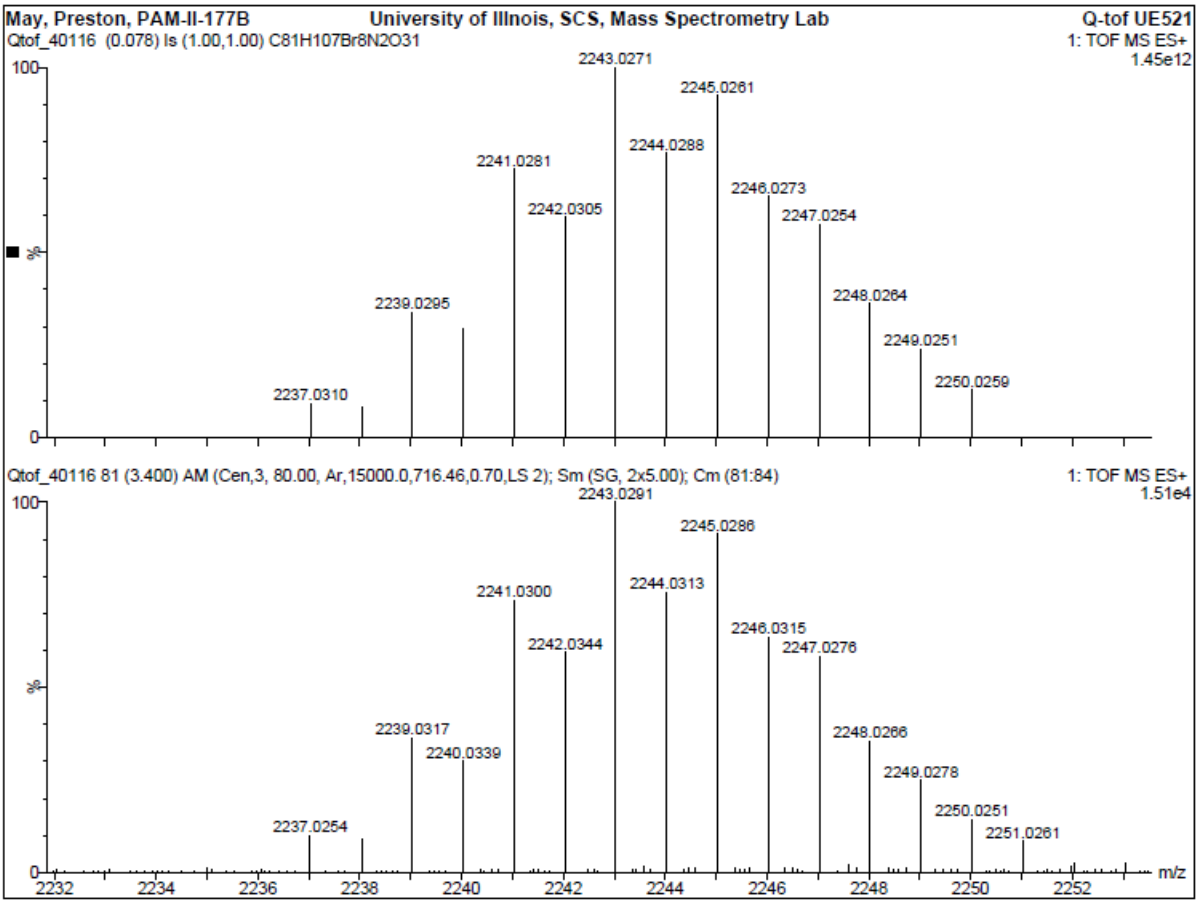

Figure 2.6. HRMS-ESI (*m*/*z*): $[M + H]^+$ calcd for $C_{81}H_{107}Br_8N_2O_{31}$, 2243.0238.

Synthesis of (((2-(((5'-methoxy-1',3',3'-trimethyl-6-nitrospiro[chromene-2,2'-indolin]-8-yl)oxy)carbonyl)-2-methylpropane-1,3-diyl)bis(oxy))bis(carbonyl))bis(2-methylpropane-3,2,1-triyl) tetrakis(2-bromo-2-methylpropanoate)

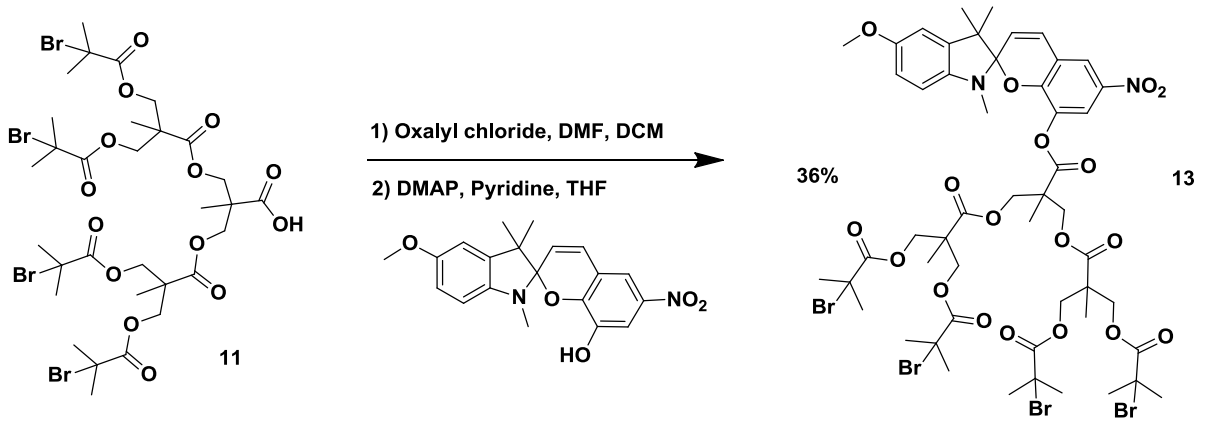

The carboxylic acid (207 mg, 0.210 mmol, 1 equiv) was dissolved in 2 mL of dry CH_2Cl_2. Oxalyl chloride (37 µL, 0.423 mmol, 2 equiv) was added dropwise to the solution. One drop of DMF was added to the solution which initiated the evolution of bubbles. The solution stirred at rt for 4 h. The solution was evaporated by rotary evaporation followed by successive additions of 2 mL of 1,2-dichloroethane and evaporation to remove excess oxalyl chloride. In a separate flask, the hydroxy spiropyran (39 mg, 0.105 mmol, 0.5 equiv) was first partially dissolved in 0.5 mL of pyridine then diluted with 0.5 mL of dry THF. DMAP (4 mg, 0.0300 mmol, 0.15 equiv) was added and the mixture was cooled to 0 °C. The acid chloride was dissolved in 2 mL of dry THF and added dropwise to the solution which caused a color change from blue to purple. The reaction was allowed to warm to rt and stir overnight. The solution was evaporated and dissolved in 50 mL of CH_2Cl_2. The solution was washed with 1 M $NaHSO_4$ (3 x 50 mL), followed by sat. aqueous Na_2CO_3 (2 x 50 mL), and finally with brine (1 x 50 mL). The organic layer was dried with Na_2SO_4, filtered, and evaporated to dryness. The product was purified by column chromatography eluting with 1% MeOH in CH_2Cl_2. The product was obtained as a purple foam with turned yellow over time: 50 mg (36%).

^{1}H NMR (400 MHz, $CDCl_3$): 7.97 (d, J = 2.6 Hz, 1H), 7.86 (d, J = 2.6 Hz, 1H), 6.97 (d, J = 10.4 Hz, 1H), 6.68 (m, 2H), 6.44 (d, J = 8.1 Hz, 1H), 5.92 (d, J = 10.4 Hz, 1H), 4.0-4.4 (m, 12H), 3.76 (s, 3H), 2.61 (s, 3H), 1.90 (m, 24H), 1.33 (s, 3H), 1.32 (s, 3H), 1.25 (s, 3H), 1.21 (s, 3H), 0.74 (s, 3H)

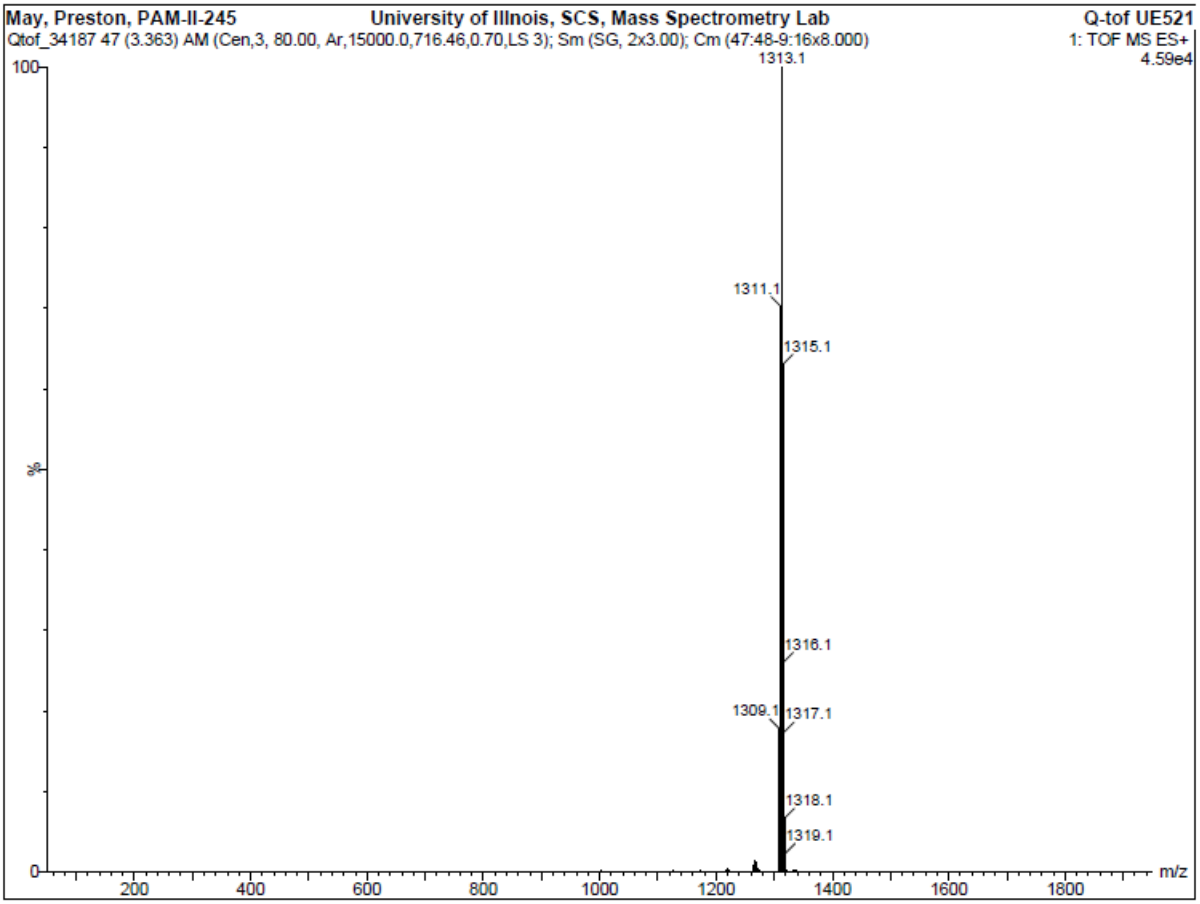

Figure 2.7 LRMS-ESI-TOF (*m*/*z*): [M + H]+ calcd for $C_{51}H_{65}Br_4N_2O_{18}$, 1313.09.

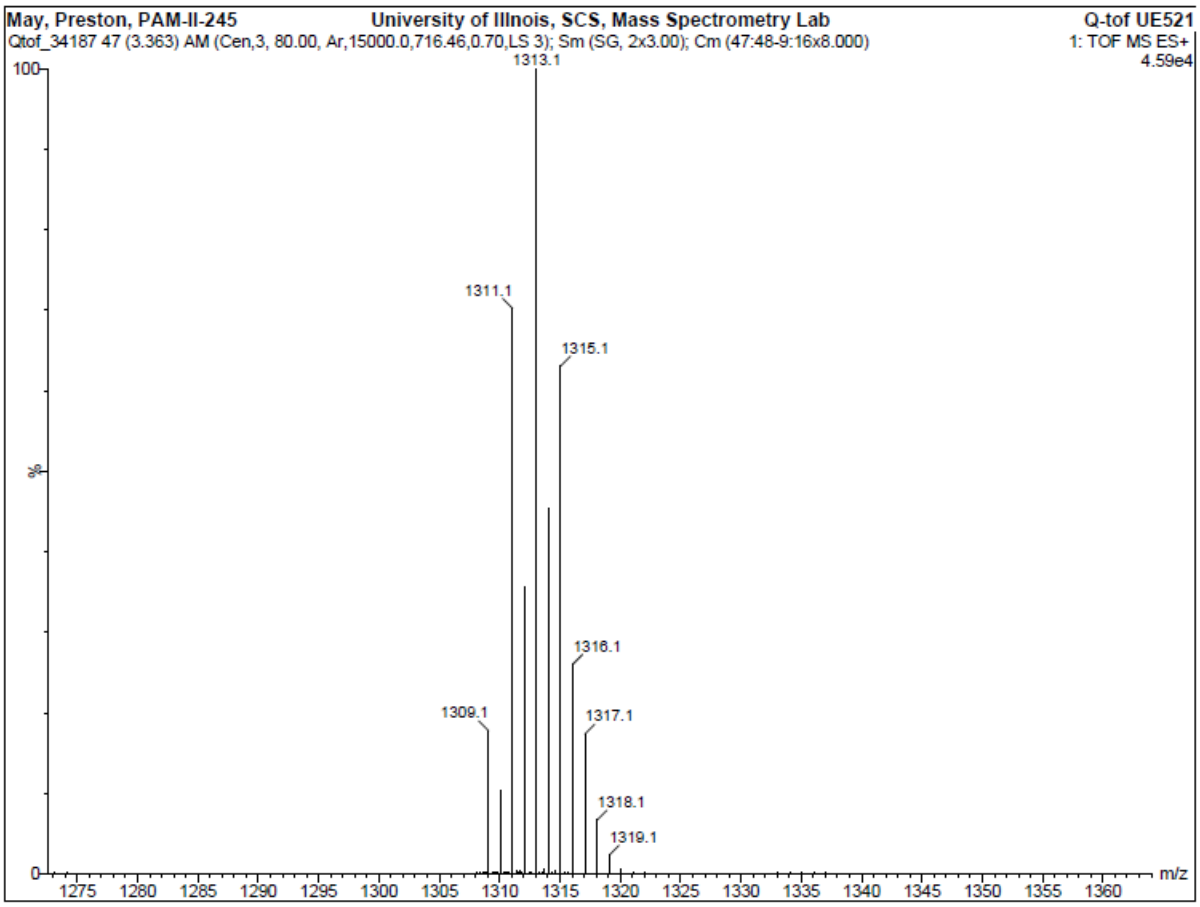

Figure 2.8. LRMS-ESI-TOF (*m/z*): [M + H]+ calcd for $C_{51}H_{65}Br_4N_2O_{18}$, 1313.09.

Synthesis of 2,3,3-trimethyl-3*H*-indole-5-carboxylic acid[23]

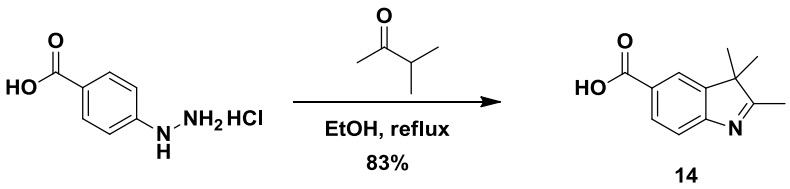

4-benzoic acid hydrazine hydrochloride (1.00 g, 5.30 mmol, 1 equiv) and methyl isopropyl ketone (0.568 mL, 5.30 mmol, 1 equiv) were dissolved in 40 mL absolute EtOH and heated to reflux using a reflux condenser under N_2 pressure. After refluxing for 5 h, the solution was concentrated *in*

vacuo. The material was redissolved in CH_2Cl_2, filtered through celite and evaporated to dryness. The product was used in the next reaction without any further purification. Orange solid: 896 mg (83%).

^{1}H NMR (400 MHz, d_6-DMSO): **δ** 12.83 (s, 1H,); 7.99 (d, J= 1.7 Hz), 7.91 (dd, J = 1.7 Hz, J = 8.2 Hz, 1H), 7.50 (d, J = 8.2 Hz, 1H), 2.25 (s, 3H), 1.28 (s, 6H).

^{13}C{^{1}H} NMR (125 MHz, $CDCl_3$) **δ** 192.9, 171.0, 156.7, 145.5, 130.9, 128.4, 123.4, 119.7, 54.1, 23.0, 15.6.

LRMS-ESI (*m*/*z*): [M + H]+ calcd for $C_{12}H_{14}NO_2$, 204.10; found, 204.0.

MP: 192-194 °C

Synthesis of 5-carboxy-1,2,3,3-tetramethyl-3*H*-indol-1-ium iodide[23]

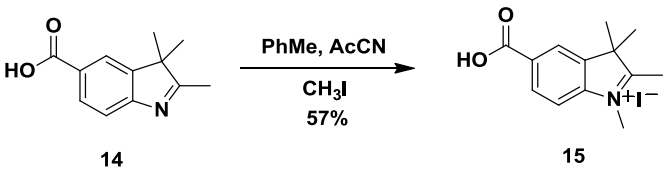

14 15

The indole (508 mg, 42.49 mmol, 1 equiv) was added to 4 mL of toluene and 2 mL of acetonitrile. Methyl iodide (778 μL, 12.45 mmol, 5 equiv) was added and heated to 75 °C using a reflux condenser under N_2 pressure. After 24 h, the solution was filtered and washed with EtOH and hexanes to give a tan solid: (488 mg, 57%).

^{1}H NMR (400 MHz, d_6-DMSO): **δ** 8.38 (s, 1H), 8.19 (d, *J* = 8.4 Hz), 8.02 (d, *J* = 8.4 Hz), 3.99 (s, 3H), 2.80 (s, 3H), 1.56 (s, 6H)

^{13}C NMR [100 MHz, CD_3CN/CD_3OD (5:1, v/v)] : **δ** 22.4, 36.0, 56.0, 116.4, 125.5, 132.2, 133.5, 143.2, 167.5.

LRMS-ESI-TOF (*m*/*z*): [M]+ calcd for $C_{13}H_{16}NO_2$, 218.12; found, 218.1.

Synthesis of 8-hydroxy-1',3',3'-trimethyl-6-nitrospiro[chromene-2,2'-indoline]-5'-carboxylic acid

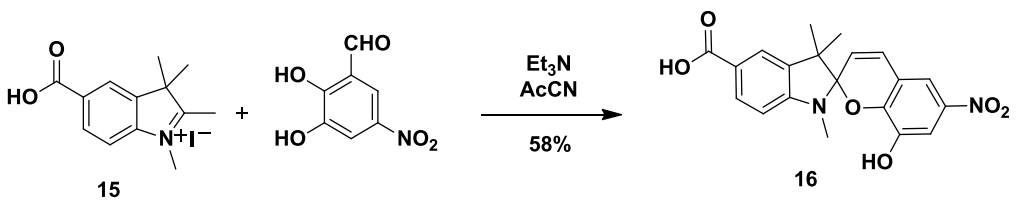

15 16

The indole salt (469 mg, 1.36 mmol, 1 equiv), 2,3-dihydroxy-5-nitrobenzaldehyde (249 mg, 1.36 mmol, 1 equiv), and triethylamine (0.379 mL, 2.72 mmol, 2 equiv) were dissolved in 13 mL acetonitrile and heated to reflux at 100 °C. After 5 h, the solution was removed from heat, filtered, washed with AcCN, and the precipitate dried under high vacuum to give a black solid: (301 mg, 58%).

^{1}H NMR (400 MHz, d_6-DMSO): **δ** 10.31 (s, 1H), 7.81 (dd, J = 1.7, J = 8.2, 1H), 7.74 (d, J = 2.8, 1H), 7.65 (d, J = 1.7 Hz, 1H), 7.56 (d, J = 2.8 Hz, 1H), 7.17 (d, J = 10.4 Hz, 1H), 6.69 (d, J = 8.2 Hz, 1H), 5.96 (d, J = 10.4 Hz, 1H), 3.81 (br, 1H), 2.77 (s, 3H), 1.24 (s, 3H), 1.19 (s, 3H).

LRMS-ESI (*m*/*z*): [M]- calcd for $C_{20}H_{17}N_2O_6$, 381.11; found, 381.1.

Synthesis of 8-(methacryloyloxy)-1',3',3'-trimethyl-6-nitrospiro[chromene-2,2'-indoline]-5'-carboxylic acid

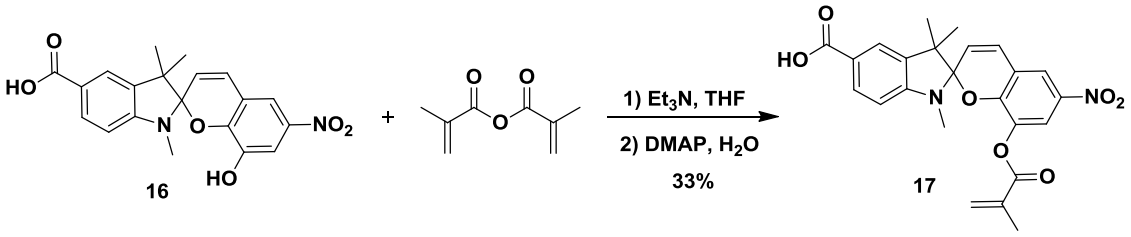

The spiropyran (548 mg, 1.43 mmol, 1 equiv) was partially dissolved in 15.3 mL of THF. Triethyle amine (420 µL, 3.01 mmol, 2.1 equiv) was added followed by methacrylic anhydride (858 µL, 5.73 mmol, 4 equiv) and the solution was allowed to stir at rt for 24 h. Next, to hydrolyze the excess methacrylic anhydride and the anhydride formed on the spiropyran, DMAP (367 mg, 2.87 mmol, 2 equiv) was added and allowed to dissolved followed by the addition of 4 mL of DI H_2O. The reaction mixture was allowed to stir at rt for another 24 h. Next, the reaction mixture was added to 150 mL of CH_2Cl_2 and washed with aqueous $NaHSO_4$ (2 x 150 mL), then washed with brine (1 x 150 mL). The organic layer was dried with Na_2SO_4, filtered and evaporated to dryness. The product was purified by column chromatography eluting with 0.5% MeOH in CH_2Cl_2 to give a light green solid: 216 mg (33%).

^{1}H NMR (500 MHz, d_6-DMSO): **δ** 12.3 (s, 1H), 8.24 (d, J = 2.7 Hz, 1H), 8.02 (d, J = 2.7 Hz, 1H), 7.79 (dd, J = 1.7 Hz, J = 8.2 Hz, 1H), 7.63 (d, J = 1.7 Hz, 1H), 7.34 (d, J = 10.4 Hz, 1H), 6.65 (d, J = 8.2 Hz, 1H), 6.11 (d, J = 10.4 Hz, 1H), 5.83 (m, 1H), 5.51 (m, 1H), 2.65 (s, 3H), 1.54 (s, 3H), 1.21 (s, 3H), 1.15 (s, 3H).

LRMS-ESI (*m*/*z*): $[M - H]^-$ calcd for $C_{24}H_{21}N_2O_7$, 449.14; found, 449.5.

Synthesis of 8-methoxy-1',3',3'-trimethyl-6-nitrospiro[chromene-2,2'-indoline]-5'-carboxylic acid[23]

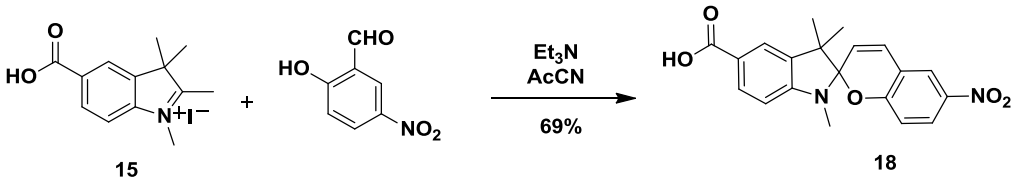

Indole salt **3** (503 mg, 1.46 mmol, 1 equiv), nitrobenzaldehyde (244 mg, 1.46 mmol, 1 equiv), and triethylamine (203 μL, 1.46 mmol, 1 equiv) were dissolved in 15 mL acetonitrile and heated to reflux. After 24 hours, the solution was removed from heat, filtered, washed with AcCN and EtOH, and the precipitate was dried under high vacuum to yield **18** as a light green solid: (371 mg, 69%).

^{1}H NMR (400 MHz, d_6-DMSO): **δ** 12.39 (s, 1H), 8.25 (d, J = 2.8 Hz, 1H), 8.02 (dd, J = 2.8 Hz, J = 9.0 Hz, 1H), 7.81 (dd, J = 1.8, J = 8.2 Hz, 1H), 7.67 (d, J = 1.8 Hz, 1H), 7.26 (d, J = 10.4 Hz, 1H), 6.92 (d, J = 9.0 Hz, 1H), 6.70 (d, J = 8.2 Hz), 6.02 (d, J = 10.4 Hz), 2.76 (s, 3H), 1.24 (s, 3H), 1.13 (s, 3H).

^{13}C{^{1}H} NMR (125 MHz, $CDCl_3$): **δ** 19.5, 25.5, 28.4, 51.5, 105.9, 106.2, 115.4, 118.8, 120.9, 121.6, 122.8, 122.9, 125.8, 128.5, 130.8, 135.9, 140.7, 151.2, 158.9, 167.3.

LRMS-FD (*m*/*z*): [M]+ calcd for $C_{20}H_{18}N_2O_5$, 366.12; found, 366.1.

M.P. 163-165 °C.

2.6 References

(1) Potisek, S. L.; Davis, D. A.; Sottos, N. R.; White, S. R.; Moore, J. S. *J. Am. Chem. Soc.* **2007**, *129*, 13808.

(2) Davis, D. A.; Hamilton, A.; Yang, J.; Cremar, L. D.; Van Gough, D.; Potisek, S. L.; Ong, M. T.; Braun, P. V.; Martínez, T. J.; White, S. R.; Moore, J. S.; Sottos, N. R. *Nature* **2009**, *459*, 68.

(3) Beiermann, B. A.; Davis, D. A.; Kramer, S. L. B.; Moore, J. S.; Sottos, N. R.; White, S. R. *J. Mater. Chem.* **2011**, *21*, 8443.

(4) Kingsbury, C. M.; May, P. A.; Davis, D. A.; White, S. R.; Moore, J. S.; Sottos, N. R. *J. Mater. Chem.* **2011**, *21*, 8381.

(5) Beiermann, B. A.; Kramer, S. L. B.; Moore, J. S.; White, S. R.; Sottos, N. R. *ACS Macro. Lett.* **2012**, *1*, 163-166.

(6) Lee, C. K.; Beirmann, B. A.; Silberstein, M. N.; Wang, J.; Moore, J. S.; Sottos, N. R.; Braun, P. V. *Macromolecules* **2013**, *46*, 3746-3752.

(7) Lee, C. K.; Davis, D. A.; White, S. R.; Moore, J. S.; Sottos, N. R.; Braun, P. V. *J. Am. Chem. Soc.* **2010**, *132*, 16107.

(8) Davis, D. Ph.D. dissertation. University of Illinois at Urbana-Champaign, **2010**.

(9) Unpublished work by Brett Beierrman.

(10) Kingsbury, C. Ph.D. dissertation. University of Illinois at Urbana-Champaign, **2012.**

(11) Wojtyk, J. T. C.; Wasey, A.; Xiao, N.; Kazmaier, P. M.; Hoz, S.; Yu, C.; Lemieux, R. P.; Buncel, E. *J. Phys. Chem. A* **2007**, *111*, 2511-2516.

(12) Song, X.; Zhou, J.; Li, Y.; Tang, Y. *J. Photochem. and Photbiol. A: Chem* **1995**, *92*, 99-103.

(13) Heise, A.; Nguyen, C.; Malek, R.; Hedrick, J. L.; Frank, C. W.; Miller, R. D. *Macromolecules* **2000,** *33*, 2346-2354.

(14) Ihre, H.; Hult, A.; Frechet, J. M. J.; Gitsov, I. *Macromolecules* **1998,** *31*, 4061-4068.

(15) Ostmark, E.; Macakova, L.; Auletta, T.; Malkoch, M.; Malmstrom, E.; Blomberg, E. *Langmuir* **2005**, *21*, 4512-4519.

(16) Barrio, J.; Oriol, L.; Alcala, R.; Sanchez, C. *Macromolecules* **200**9, *42*, 5752-5760.

(17) Ihre, H.; Padilla De Jesus, O. L.; Frechet, J. M. J. *J. Am. Chem. Soc*. **2001**, *123*, 5908-5917.

(18) Malkoch, M. Claesson, H.; Lowenhielm, P.; Malmstrom, E.; Hult, A. Journal of Polymer Science: Part A: Polymer Chemistry 2004, 421758-1767.

(19) Parrott, M. C.; Benhabbour, R.; Saab, C.; Lemon, J. A.; Parker, S.; Valliant, J. F.; Adronov, A. *J. Am. Chem. Soc*. **2009**, *131*, 2906-2916.

(20) Gorelik, S.; Hongyan, S.; Lear, M. J.; Hobley, *J. Photochem.and Photobiol. Sci*. **2010**, *9*, 141-145.

(21) Rosario, R.; Gust, D.; Hayes, M.; Jahnke, F.; Springer, J.; Garcia, A. A. *Langmuir* **2002**, *18*, 8062-8069.

(22) Rosario, R.; Gust, D.; Hayes, M.; Springer, J.; Garcia, A. A. *Langmuir* **2003**, *19*, 8801-8806.

(23) Tomasulo, M.; Kaanumal, S. L.; Sortino, S.; Raymo, F. M. *J. Org. Chem.* **2007**, 72, 595-605.

(24) Zhang, P.; Meng, J.; Li, X.; Matsura, T.; Wang, Y. *J. Heterocyclic Chem. 2002*, **39**, 179-184.

Chapter 3 – Investigating Architecture Effects Using Spectroscopy-Coupled Ultrasonication

3.1 Introduction

Polymer mechanochemistry is a unique area of research experiencing a resurgence in recent years.[1-4] The fundamental mechanism of interest is the transduction of macroscopic forces into a select few chemical bonds within polymers. This process results in distortion of molecular orbital overlap and, ultimately, rupture of the forces holding atoms together. This chemical event represents a unique opportunity to program intrinsic chemical responses into load-bearing materials such as self-sensing of mechanical integrity, self-reinforcing feedback mechanisms, and, ultimately, the autonomous repair of structural defects. However, achieving these goals is predicated on our ability to understand mechanotransduction processes. We must learn the design rules for creating mechanically sensitive molecules and couple that knowledge to produce synthetic materials with useful mechanoresponsive properties. At present, many types of mechanically-induced transformations have been demonstrated including forced-induced catalysis,[5,6] generation of reactive cyanoacrylates,[7] mechanochromic force sensors,[8] and even mechanically-generated acids and bases.[9] In the context of polymer mechanochemistry, the term 'mechanophore' has been adopted to describe these types of mechanically sensitive molecules with latent reactivity.[10] The forces needed to elicit mechanophore activation can be supplied to the polymers by several means;[11] however, the most widely adopted technique uses ultrasound irradiation applied to polymer solutions.[4] Ultrasonication has proved to be a valuable screening tool for new mechanochemical transformations due to the small sample requirement, reproducibility, and the high strain rates imposed on the polymer chains. While discovering new mechanophores is a frontier of this field, rigorous kinetic analyses of these reactions provide the opportunity to greater understand the nature of mechanochemical transduction in polymers. For example, Kryger et al., were able to determine activation rate consequences of stereochemical variances within dicyanocyclobutane mechanophores with extensive kinetic information.[13] Additionally, Brantley et al. investigated the effects of polymer attachments sites to mechanophores with triazole regioisomers.[14] We were interested in the role of the polymer chains in mechanotransduction to the mechanophore. To date, very few reports address this topic and most regard the chains simply as inert handles needed to transmit force to the mechanophore.[15-17] We wondered if we could uncouple the properties of molecular mass and chain length of the polymers to determine which property relayed force transfer to the mechanophore more efficiently. To help us achieve this goal we sought out a method to improve the ultrasonication technique analytically. Recently, Giz et al. described an ultrasonication technique with online light scattering measurements to monitor weight-average molecular weight changes of poly(vinylpyrrolidone) *in-situ*.[18-19] Likewise, with our experimental

efforts, we aimed to create an increased throughput method to acquire mechanokinetic information directly from a single mechanophore embedded in a macromolecule. Herein, we report the design and implementation of an ultrasonication flow system with synchronous UV-Vis absorption spectroscopy. From a practical standpoint, we are able to monitor reactivity in real-time while acquiring kinetic information on color-changing spiropyran mechanophores in a highly efficient manner. Furthermore, with this technique in hand, we examined the influence of several sonication parameters on this force-induced transformation including flow rate and sonication intensity. Finally, we were able to systematically investigate a series of spiropyran-linked polyacrylates and found a stronger relationship between chain length and activation than with molecular weight of the polymers.

3.1.1 Spiropyran Mechanophores

Spiropyran mechanophores have become model compounds for studying mechanochemical reactivity in both solution-based and solid-state polymers. This mechanophore has been embedded in linear polymers such as poly(methyl acrylate) (PMA),[20,21,22] poly(methyl methacrylate) (PMMA),[22,23] polyurethanes (PU),[24] poly(caprolactone) (PCL),[25] and as crosslink junctions in PMMA.[26] Spiropyran can be converted to a merocyanine form, reversibly, through a number of different stimuli,[27] including light, heat, change in pH, solvent interactions, and, specific to our experiments, mechanical force (Figure 3.1). Two spectroscopic signals can be attributed to this chemical transformation: a change in the visible absorption spectrum and a change in the fluorescence spectrum. While the spiropyran does not absorb light in the visible spectrum, the merocyanine displays a large absorption peak, centered around 550 nm (solvent dependant). Additionally, the spiropyran emits no fluorescence, while the merocyanine is excited at 550 nm and emits fluorescent light of c.a. 620 nm.

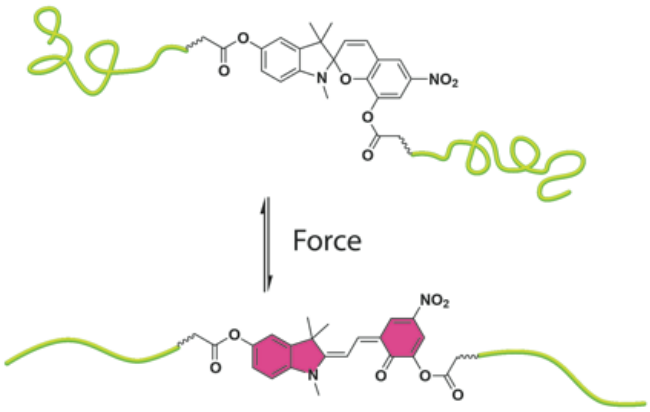

Figure 3.1. Response of spiropyran-linked polymers to ultrasound-induced cavitation. The spiropyran is converted to its highly colored merocyanine form by mechanical force.

3.2 Polymer Synthesis

For our experimental efforts, polymers were grown from a bis-functional spiropyran initiator[20] using single-electron-transfer living radical polymerization (SET-LRP)[28] to achieve polymers covalently linked near the center by the mechanophore (See Scheme 3.1). Target molecular weights were achieved by controlling the initiator to monomer ratios, and low PDIs for all polymerizations were attained (See Table 3.1). The initiator was polymerized with a variety of monomers including methyl acrylate, ethyl acrylate, *n*-butyl acrylate, *iso*-butyl acrylate, and *tert*-butyl acrylate.[29] For very high molecular weight poly(butyl acrylates), an excess of monomer was used to mitigate the growing polymers from precipitating from DMSO before reaching the target molecular weight. Molecular weight and polydispersity indices were recorded using an analytical GPC that had been calibrated with polystyrene standards (Table 3.1).

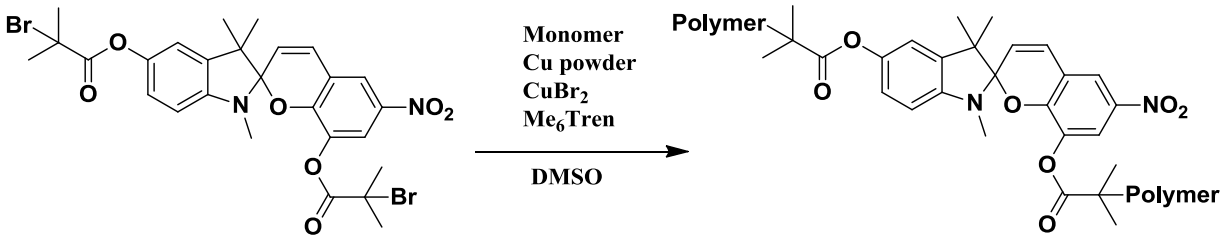

Scheme 3.1. SET-LRP of Bis-functional Spiropyran Initiator

Table 3.1. Molecular Weight Data of Synthesized Polyacrylates

PMA		**PEA**		**P*n*BA**		**P*i*BA**		**P*t*BA**	
M_n (kDa)	**PDI**	**M_n (kDa)**	**PDI**	**M_n (kDa)**	**PDI**	**M_n (kDa)**	**PDI**	**M_n (kDa)**	**PDI**
270	1.25	282	1.16	224	1.21	309	1.31	292	1.21
194	1.24	233	1.13	184	1.3	239	1.32	273	1.26
184	1.21	177	1.24	137	1.33	167	1.18	226	1.18
156	1.22	155	1.16	98	1.35	152	1.19	178	1.17
139	1.28	121	1.11	87	1.24	81	1.17	131	1.12
102	1.31	96	1.28	60	1.25	60	1.13	89	1.27
54	1.34	77	1.22	-	-	-	-	50	1.19
-	-	49	1.22	-	-	-	-	-	-

3.3 Spectroscopy-Coupled Ultrasonication

A custom flow cell was constructed using a peristaltic pump to draw fluid from the reaction vessel (Suslick cell), flow it through a UV-Vis flow-through cuvette for light absorption measurements, and return the fluid back to the reaction vessel continuously throughout the course of each experiment. Flow rates were held constant for each experiment. The total volume of the apparatus was 16 ml with 7.5 ml in the Suslick cell. The remaining 8.5 ml filled the Teflon tubing and cuvette. Additionally, the solutions were irradiated with continuous, not pulsed, ultrasound at 20 kHz and varying power intensities. The Suslick cell was submerged in a cooling bath which was regulated by an immersion cooler to achieve a consistent temperature of 3-5 ºC of the reaction mixture in the Suslick cell throughout all experiments. Polymer solutions were sonicated at a concentration of 1 mg mL^{-1} in either acetonitrile or methyl ethyl ketone (MEK) using argon as the saturation gas. The UV-Vis spectrometer was programmed to obtain either full spectra, absorbance at one wavelength or two wavelengths over time.

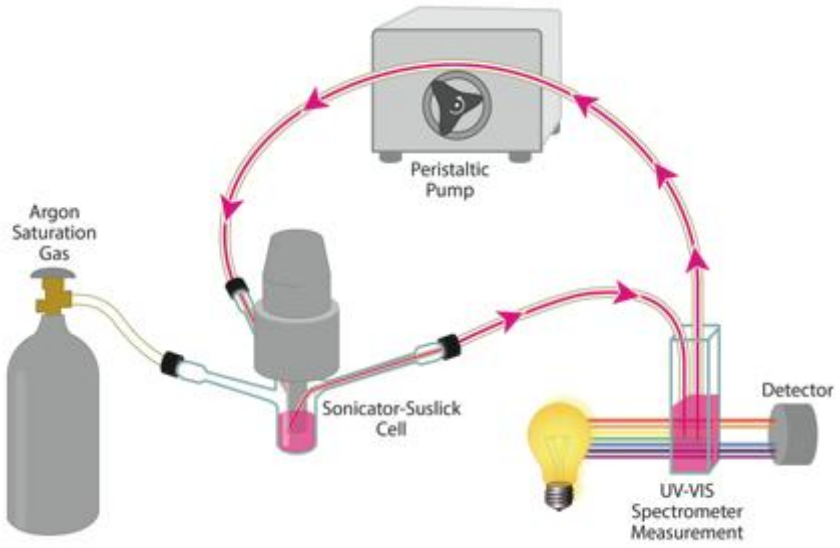

Figure 3.2. Representation of the flow system experimental set-up. Reaction mixture is circulated from the Suslick cell to the UV-Vis spectrometer via a peristaltic pump. The Suslick cell is submerged in a cooling bath (not shown).

3.3.1 Activation Characterization

Mechanochemical characterization of these polymers was streamlined by the use of a flow-through system represented in Figure 2. Upon subjecting the polymers to ultrasonication in this setup, a smooth rise in the absorption of the merocyanine form can be observed (Fig. 3.3a). The change from spiropyran to merocyanine can be monitored as a function of time and asymptotically levels off as the maximum amount of merocyanine species is reached (Fig. 3.3b). Importantly, control polymers containing spiropyrans only at their terminus do not show this change in absorption when irradiated with ultrasound, but do change their absorption spectrum when irradiated with UV light due to the presence and photochemical activity of the spiropyran (Fig. 3.3c). The spiropyran and merocyanine conformations exist in equilibrium which can be biased by a number of different stimuli, as mentioned earlier. Before ultrasound is applied, the spiropyran form is favored. Upon irradiation with ultrasound, the ring-opening reaction proceeds at a much higher rate than ring-closing until the system reaches a new dynamic equilibrium, a mechanostationary state, where the merocyanine is favored. This dynamic equilibrium is short-lived due to occurring chain cleavage which relieves the molecular strain on the mechanophore. Figure 3.3d shows a cycling experiment where ultrasound irradiation is applied and removed, repeatedly, showing the change in merocyanine absorption for the forward and reverse reactions.

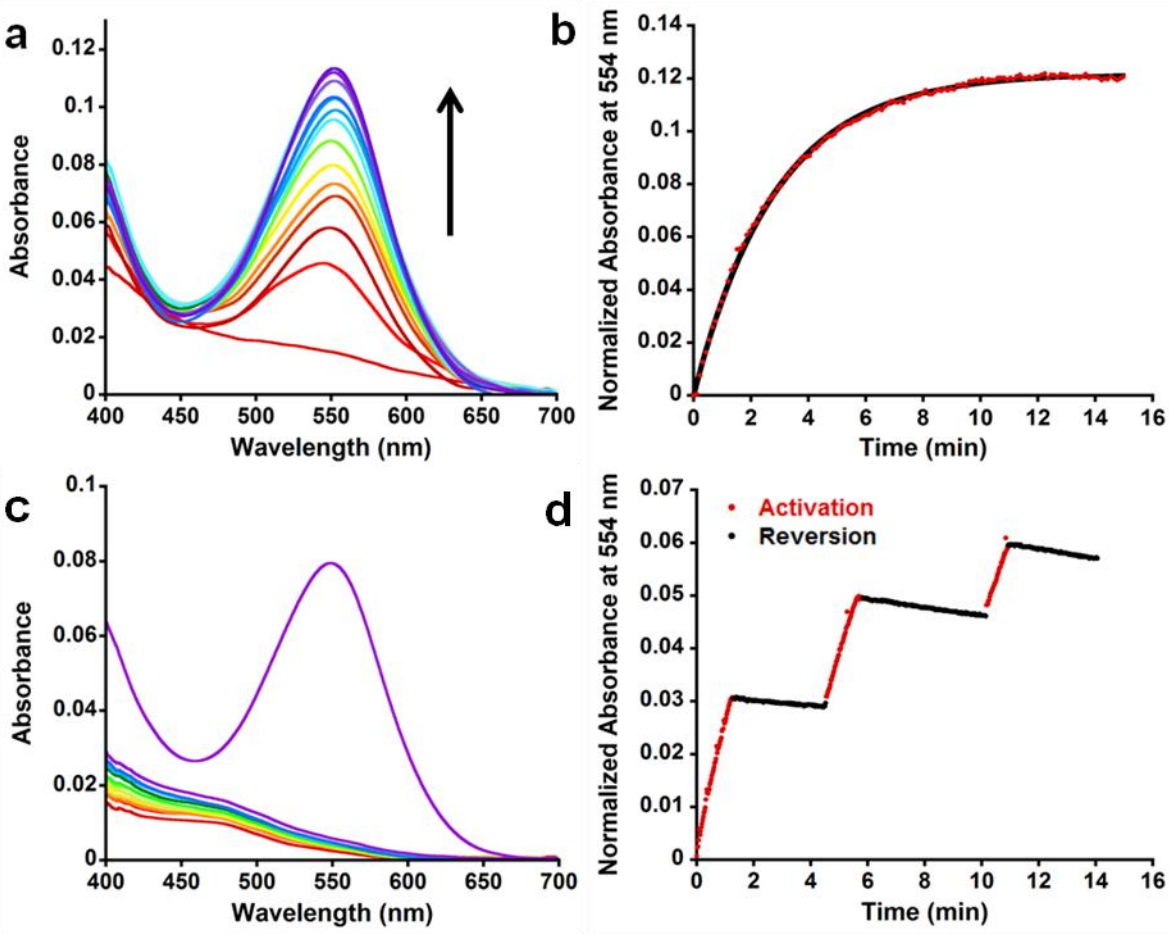

Figure 3.3. a) Change in the visible absorption spectrum of spiropyran-linked PMA (M_n = 156 kDa, PDI = 1.22) in acetonitrile subjected to ultrasound (10.7 W cm^{-2}) in the flow cell (λ_{max} = 554 nm. b) Change in the normalized absorbance at 554 nm with respect to time. Red dots are raw data points. Black line is non-linear regression of the data fit to equation 1: $A_t = B\left(1 - e^{-kt}\right)$. c) Spectra of spiropyran end-functionalized PMA control (M_n = 154 kDa, PDI = 1.13) collected during sonication (bottom spectra) showing very little change and the spectrum measured after irradiation with UV light (365 nm for 5 min) (purple spectrum). d) Sonication cycling experiment. Ultrasound irradiation is applied (red) and removed (black), repeatedly, showing the forward reaction and reverse reactions.

3.3.2 Effects of Flow Rate

Determining the rate of the spiropyran to merocyanine conversion under ultrasound irradiation allowed us to systematically investigate various factors influencing this reaction. Besides ultrasonication, several other techniques generate elongational flow fields which can lead to polymer scission such as cross-slots and abrupt contraction flows.[4,11] These techniques, however, all differ from ultrasonication because they are macroscopically flowing. Therefore, we set out to probe the effects of flow rate on the reactivity of the mechanophores in this system. For these experiments PMA polymers were sonicated in acetonitrile at varying flow rates in the flow system. Each molecular weight sample was sonicated in

duplicate at a power intensity of 10.7 W cm^{-2} and the rate constants were calculated by the previously described method. By comparing the change in the rate constant as a function of initial molecular weight, we are able to determine if there were any significant effects on reactivity by varying the flow rate. As expected, all sonicated polymers exhibited a linear increase in rate constant with increasing initial molecular weight. Additionally, all polymers showed a limiting molecular weight threshold, below which no activation occurs. Figure 3.4 shows there was no observable effect on reactivity for the three flow rates we tested. Statistical analysis showed no difference in slope or elevation (x-axis intercept) between any of the flow rates tested at a 95% confidence interval.[30]

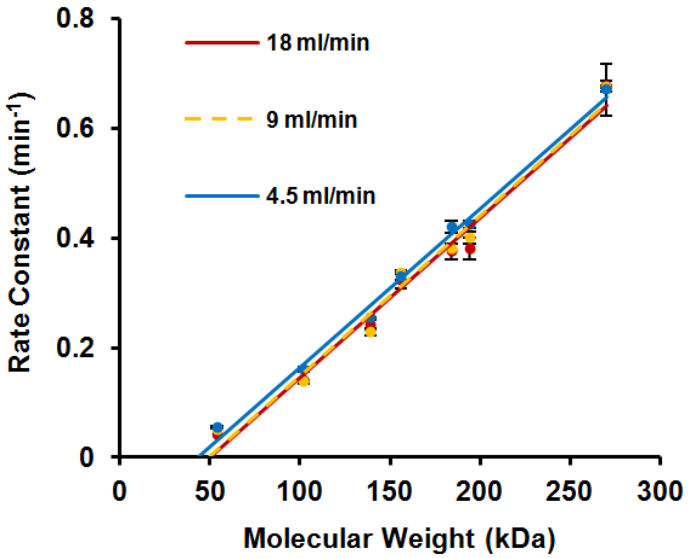

Figure 3.4. Effect of reactivity on varying flow rate. Reaction kinetics are independent of flow rate. Rate constants plotted (data points) are averages of two sonication experiments. Error bars represent the maximum and minimum rate constants obtained experimentally.

3.3.3 Effects of Sonication Intensity

Next, we probed the effects of power intensity on the mechanophore containing polymers. The literature is inconclusive how changing the power intensity affects mechanoactivation of polymers. The increased intensity is mainly thought to increase the number of cavitation events per unit of volume, therefore increasing the reaction rate.[31] The secondary effect is thought to be an increase in bubble size, leading to a more violent cavitation event, and ultimately higher strain rates experienced by the polymer chains.[32] Larger bubble diameter would have a two-fold result; not only would the reaction rate increase with increasing sonication intensity, the limiting molecular weight threshold (x-axis intercept) should lower due to higher forces experienced by the polymers. Importantly, increasing the power intensity also increases the temperature of the reaction medium which must be taken into account. Accordingly, for

each increase in power intensity a corresponding decrease in the temperature of the cooling bath was used to compensate and perform all experiments at the same temperature (3-5 °C). For these experiments, we sonicated the PMA series in acetonitrile at varying power intensities and constant flow rate (4.5 mL min^{-1}). Figure 3.5 shows the results of probing the change in reactivity of spiropyran-linked PMA with varying power intensity in our flow cell. A change in the slope for each regression line correlates well with the increased power intensity. Statistical analysis revealed that the differences in slopes between all power intensities were statistically significant at a 95% confidence interval. However, we do not observe any noticeable change in the lower molecular threshold. This observation gives strong evidence that, while there is a strong contribution of the increased number of cavitation events, there seems to be little evidence for the proposed secondary effect of larger bubbles creating higher strain rates.

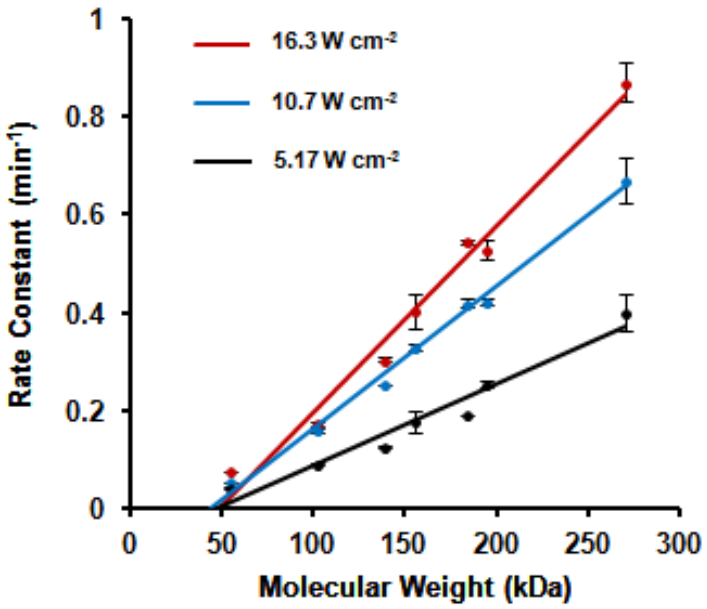

Figure 3.5. Effect of power intensity on reactivity. Reaction rates are increased (increase in slope) while M_{lim} (x-axis intercept) is not affected. Rate constants plotted (data points) are averages of two sonication experiments. Error bars represent the maximum and minimum rate constants obtained experimentally.

3.3.4 Effects of Polymer Chain Architecture

For our final series of experiments, we probed the effect of polymer chain architecture on mechanophore activation. A rigorous investigation was recently performed by Kryger et al. where it was shown that changing the stereochemistry and subsitition density of a dicyanocyclobutane mechanophore influenced the limiting molecular weight threshold of mechanophore-linked PMA.[13] Additionally, Brantley et al. showed that polymer attachment regiochemistry can influence the rate of triazole mechanophore activation.[14] Here the mechanophore structure and polymer attachment sites were kept

constant, while the polymer architecture was varied. We compared the differences in reactivity of PMA, PEA, P*n*BA, P*i*BA, and P*t*BA, all of which contained the same spiropyran at the chain center. The various repeating units in the polymers allow us to test the effects of molecular mass against chain length. For example, a P*n*BA chain and a PMA chain of similar molecular weight will have different chain lenghts due to a portion of the total mass of the P*n*BA chain functioning as a side chain and not contributing to the length of the backbone. Additionally, the poly(butyl acylates) of similar molecular weight all have similar chain lengths but vary only by the branching of the side chain. These polymers allowed us to test the effects of branching in the side chain. For these experiments, MEK was chosen as the solvent as the poly(butyl acrylates) were not soluble in acetonitrile. These experiments were performed at a constant flow rate (4.5 mL min^{-1}) and constant power intensity (10.7 W cm^{-2}). The merocyanine displayed a λ_{max} value of 570 nm in MEK for all polymers and the small molecule initiator.. Additionally, reversion rate constants of all polymers in MEK are similar suggesting no different electronic interactions between the mechanophore and polymer chains which have varying polarity. Examining the rate constant vs molecular weight plots gave insight into the differences in reactivity as a function of polymer architecture. Figure 3.6a shows a difference in slopes between the polymers that correspond to the molecular weight of the monomers. PMA has the largest slope and lowest molecular weight repeating unit, followed by PEA with a slightly smaller slope and higher molecular weight of the repeating unit. Accordingly, all butyl acrylate isomers (*n*-butyl, *iso*-butyl, and *tert*-butyl) resulted in the same slope and all being lower than PMA and PEA. Pairwise *t* tests confirmed a statistically different slope between PMA and all other polymers. Additionally, PEA was found to have a statistically significant difference in slope compared to all other polymers. Furthermore, we found no statistical difference in slope or elevation between any of the butyl acrylate polymers. Alternatively, we examined the data from the perspective of chain length as shown in Figure 3.6b. Degree of polymerization gives the number of monomer units in a chain, regardless of molecular weight. Figure 3.6b shows that all regression lines become equivalent when plotting them as rate constant vs degree of polymerization. Statistical analysis confirmed no difference in slope or elevation in any of these regression lines. Together these data show that to achieve an equivalent increase in the rate constant of mechanophore activation an equivalent increase in chain length is needed, independent of molecular weight of the individual chains. It would be interesting to study an extreme limit of this type of architecture trend (e.g. a high molecular weight brush polymer) to test the boundaries of side chain molecular weight and chain length influence.

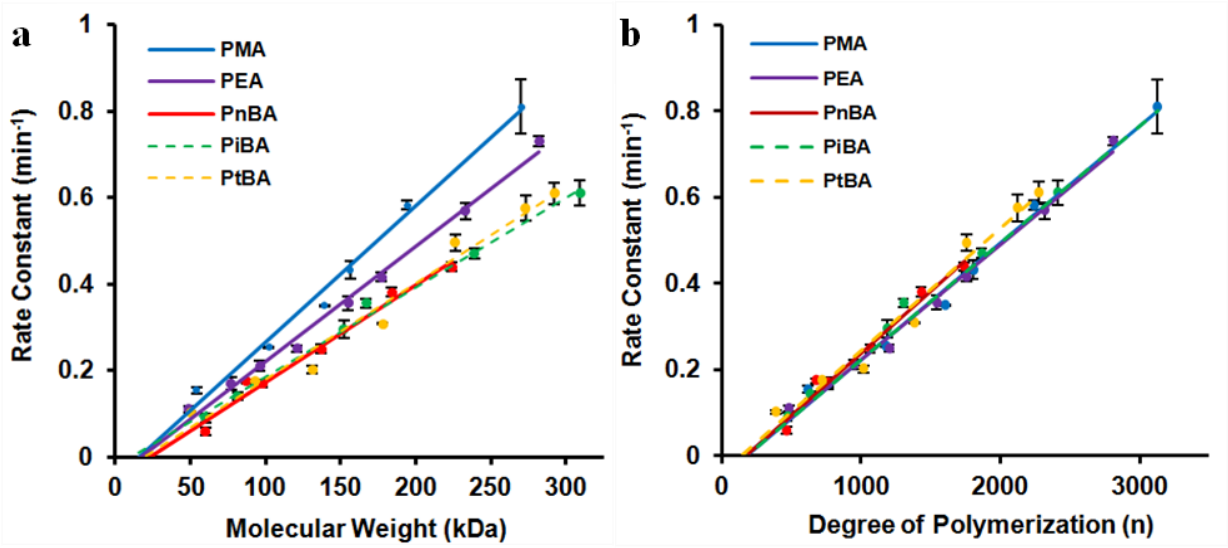

Figure 3.6. A) Plot of rate constant vs molecular weight of varying polyacrylates. Blue = PMA, Purpe = PEA, Red = PnBA, Green (dashed) = PiBA, Orange (dashed) = PtBA. Slopes are determined by monomer molecular weight. B) Plot of rate constant vs degree of polymerization of the same set of polymers. Slopes and M_{lim} are all equivalent. Rate constants plotted (data points) are averages of two sonication experiments. Error bars represent the maximum and minimum rate constants obtained experimentally.

3.4 Conclusions

We demonstrated the design and implementation of a fully automated ultrasonication flow cell with online UV-Vis spectroscopy using readily available components to study the kinetics of spiropyran mechanophore activation. We envision this technique to be directly amenable to any mechanophore that exhibits a change in its UV-Vis absorption spectra. Future iterations of this technique could make use of other spectroscopic signals such as fluorescence, infrared (IR) or light scattering to study mechanochemical reactions. With this system, we were able to quickly screen the effects of flow rate, power intensity and chain architecture on mechanophore activation. We found that activation kinetics are independent of flow rate. In addition, power intensity affects the rate of activation but not M_{lim} giving strong evidence that power intensity controls the frequency of cavitation but not the strength.

Furthermore, we synthesized a series of various polyacrylates and found that chain length, not molecular weight, is the materials property that controls activation. One could extrapolate this data to an extreme, such as a high molecular weight brush polymer, and hypothesize that it would require sufficient backbone length, independent of total molecular weight, to achieve reasonable mechanophore activation under ultrasound-induced cavitation. It could also be reasonably assumed that the side chains of a brush polymer would contribute little to mechanophore activation unless they are of significant length. However, these assumptions should be tested experimentally and perhaps there exists a crossover point (i.e. when the side-chains become comparable in length to M_{lim} of the main-chain) where side-chains of a

brush polymer begin to influence mechanophore activation. Additionally, an interesting avenue to explore would the backbone chemistry of the polymer. Here, the polymers used contained C-C bonds in the backbone. Perhaps optimal polymer chain chemistry exists that transmits force more efficiently than others, although polymer-solvent interactions might contribute to any observed differences in activation of different chain chemistries. An interesting possibility to explore might be block copolymers or brush polymers with different main-chain and side-chain chemistries. However, at this point in time, the evidence suggests that chain length is the main factor contributing to mechanophore activation and it is recommended to target large chain lengths to achieve the fastest mechanophore response.

Finally, we aim to use this ultrasonication technique to perform broad, systematic surveys of mechanochemical activation parameters of mechanophores. To this end, we aim to acquire knowledge relevant to the design of new mechanoresponsive materials such as polymer-solvent interactions, tuning of mechanophore sterics and electronics, and polymer microstructure.

3.5 Detailed Procedures

3.5.1 General Experimental Details

Unless otherwise stated, all starting materials were obtained from commercial suppliers and used without purification. Anhydrous acetonitrile was obtained from Acros (Acroseal, 99.9%). Methyl ethyl ketone (MEK), Cu(0) powder (99%, 1-5 μm) and Me_6TREN were purchased from Sigma-Aldrich. Silica gel 60 (230-400 mesh) was purchased from Silicycle. Acrylate monomers were filtered through basic alumina to remove the inhibitors prior to use and kept under an argon atmosphere. Cu(0) powder was sonicated in DMSO in a Fisher Scientific Tabletop Ultrasonic Cleaner, model FS-20D (3/4 gal tank), 40kHz, with a max input power of 80W. All synthetic reactions and sonication experiments were performed under argon atmosphere.

Analytical gel permeation chromatograph (GPC) analyses were performed with a Waters 1515 Isocratic HPLC pump, a Waters (2998) Photodiode Array Detector, a Waters (2414) Refractive Index Detector, a Waters (2707) 96-well autosampler, and a series of 4 Waters HR Styragel columns (7.8 X 300mm, HR1, HR3, HR4, and HR5) in THF at 30 °C. The GPC was calibrated using monodisperse polystyrene standards.

UV-Vis spectra were recorded using a Shimadzu UV-2401PC. Standard quartz cells and standard quartz flow cell cuvettes with a path length of 10 cm used were purchased from Starna Cells. UV

irradiation of samples dissolved in acetonitrile or MEK was performed with a Model UVG-11 Mineralight lamp (short wave UV – 254 nm or long wave UV-365 nm).

Ultrasound experiments were performed on a Vibra Cell 505 liquid processor with a ½" diameter solid probe from Sonics and Materials. The distance between the titanium tip and bottom of the Suslick cell was 1 cm. The Suslick cells were made by the School of Chemical Sciences' Glass Shop at the University of Illinois. PTFE tubing was used to circulate the solvent. A peristaltic pump from equipped with a Masterflex L/S PTFE-tubing pump head was purchased from Cole-Parmer. A Neslab CC 100 immersion cooler equipped with a Neslab cryotrol temperature controller was purchased from Thermoscientific.

3.5.2 Synthetic Procedures

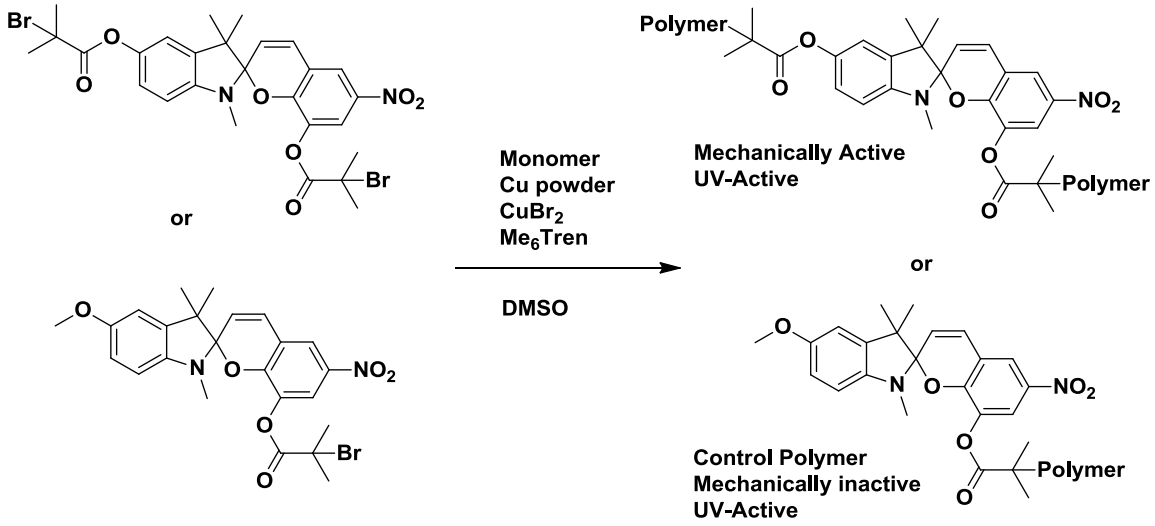

Scheme 3.2. Components of SET-LRP

Cu(0) (2.44 mg) was weighed on analytical balance and then added to a 20 mL scintillation vial. DMSO (0.5 ml) was added to the vial and the mixture was sonicated in a sonicator bath for c.a. 1 min. An aliquot of 0.25 mL (containing 1.22 mg Cu(0), 0.0192 mmol, 2 equiv) was removed and added to a 10 mL Schlenk flask equipped with a teflon stir bar. $CuBr_2$ (1.72 mg) was added to 2 mL of DMSO and allowed to dissolve. An aliquot of 0.25 mL was removed (containing 0.215 mg $CuBr_2$, 0.000961 mmol, 0.1 equiv) and added to the Schlenk flask. Me_6TREN (5.40 µL, 0.0202 mmol, 2.1 equiv) was measured with a microliter syringe and transferred to the Schlenk flask. Monomer (1.00 mL, 11.1 mmol, 1154 equiv) was added. Lastly, the initiator[20,21] (6.27 mg, 0.00961 mmol, 1 equiv) was added to the flask. The

flask was immediately sealed with a ground glass stopper, secured with copper wire, and three freeze-pump-thaw cycles were applied to remove dissolved oxygen. The flask was backfilled with argon and was allowed to stir in a water bath for 2 h at room temperature. The polymerization was opened to air, 10 mL of THF were added, and the polymer filtered through a pad of silica gel. After solvent was removed *in vacuo*, a highly concentrated mixture of polymer in THF was precipitated by drop wise addition to stirring cold methanol. Poly(ethyl acrylate), poly(n-butyl acrylate), poly(*iso*-butyl acrylate), and poly(*tert*-butyl acrylate) were precipitated from a 50:50 mixture of MeOH:H_2O. The resulting polymer was collected and dried under vacuum at 50 °C.

Table 3.2: Conditions used for SET-LRP

Polymer Type	Initiator (eq)	Cu(0) (eq)	$CuBr_2$ (eq)	Me_6Tren (eq)	DMSO (vol)	Monomer (vol)
Poly(methyl acrylate)	1.0	2.0	0.1	2.1	0.5 ml	1.0 ml
Poly(ethyl acrylate)	1.0	2.0	0.1	2.1	0.5 ml	1.0 ml
Poly(n-butyl acrylate)	1.0	2.0	0.1	2.1	0.5 ml	1.0-1.5 ml
Poly(*iso*-butyl acrylate	1.0	2.0	0.1	2.1	0.5 ml	1.0-1.5 ml
Poly(*tert*-butyl acrylate)	1.0	2.0	0.5	2.5	0.5 ml	1.0-1.5 ml

Table 3.3: Poly(methyl acrylate) characterization

M_n (kDa)	PDI
270	**1.25**
194	**1.24**
184	**1.21**
156	**1.22**
139	**1.28**
102	**1.31**
54	**1.34**

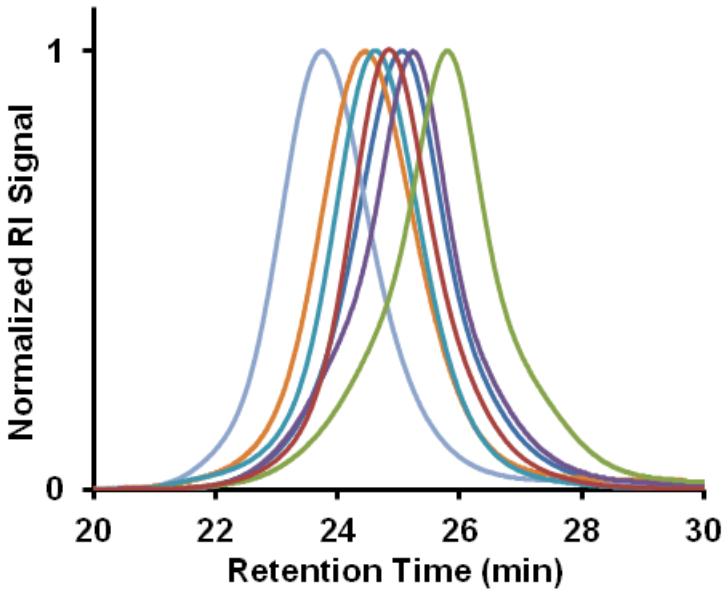

Figure 3.7. GPC traces of spiropyran-linked poly(methyl acrylate).

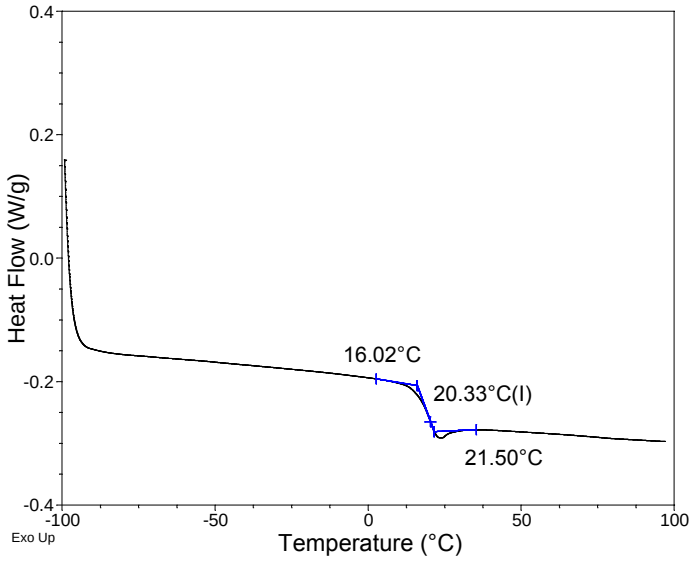

Figure 3.8. DSC trace of PMA (M_n =156) showing glass transition temperature (onset, midpoint, endset).

Table 3.4. Poly(ethyl acrylate) characterization

M_n (kDa)	PDI
282	1.16
233	1.13
177	1.24
155	1.16
121	1.11
96	1.28
77	1.22
49	1.22

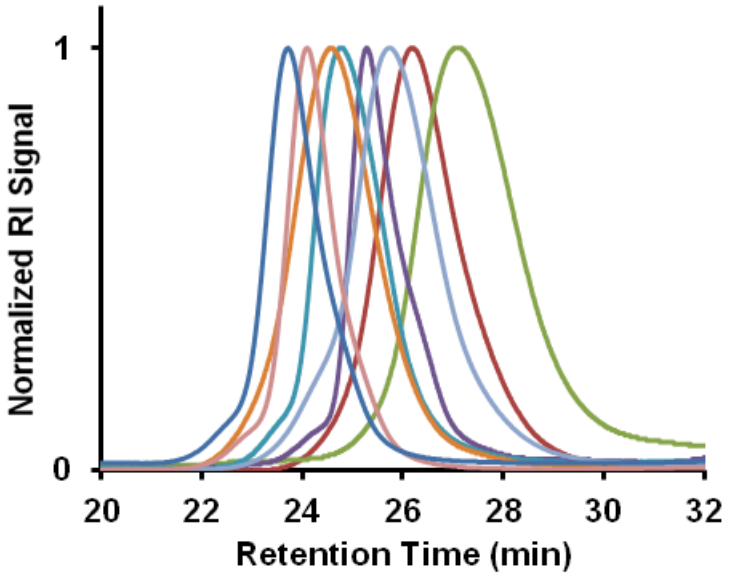

Figure 3.9. GPC traces of spiropyran-linked poly(ethyl acrylate).

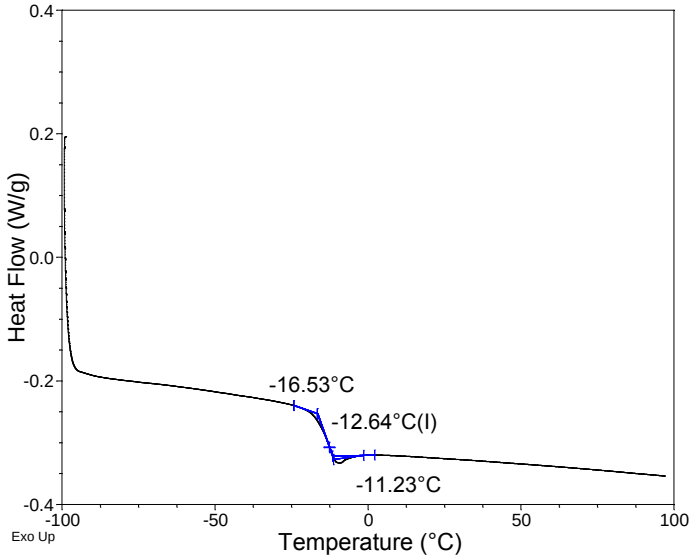

Figure 3.10. DSC trace of PEA (M_n =155) showing glass transition temperature (onset, midpoint, endset).

Table 3.5 Poly(n-butyl acrylate) characterization

M_n (kDa)	PDI
224	**1.21**
184	**1.30**
137	**1.33**
98	**1.35**
87	**1.24**
60	**1.25**

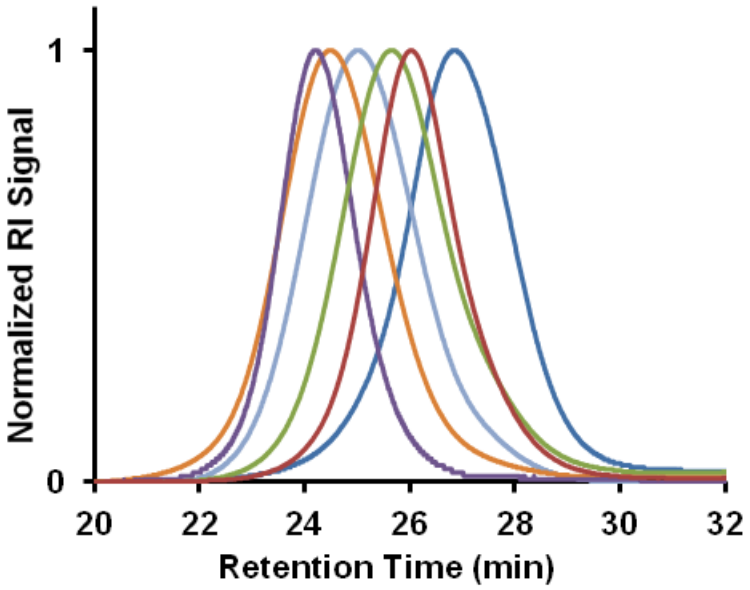

Figure 3.11. GPC traces of spiropyran-linked poly(n-butyl acrylate).

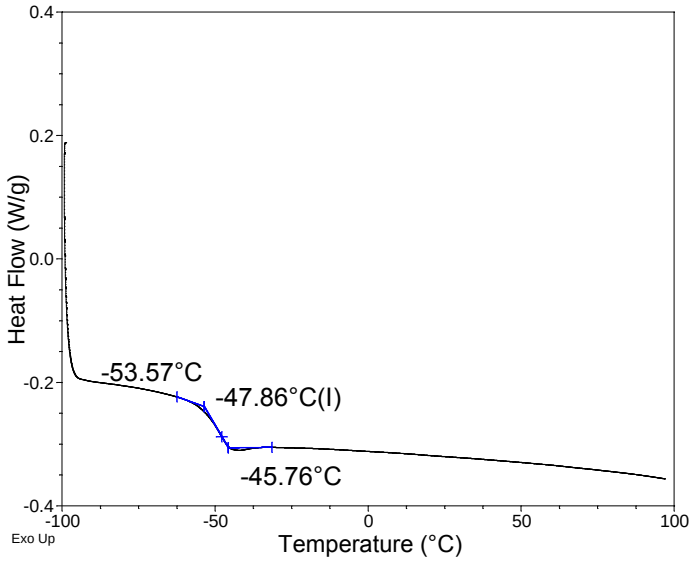

Figure 3.12. DSC trace of PnBA (M_n =137) showing glass transition temperature (onset, midpoint, endset).

Table 3.6. Poly(*iso*-butyl acrylate) characterization

M_n (kDa)	PDI
309	**1.31**
239	**1.32**
167	**1.18**
152	**1.19**
81	**1.17**
60	**1.13**

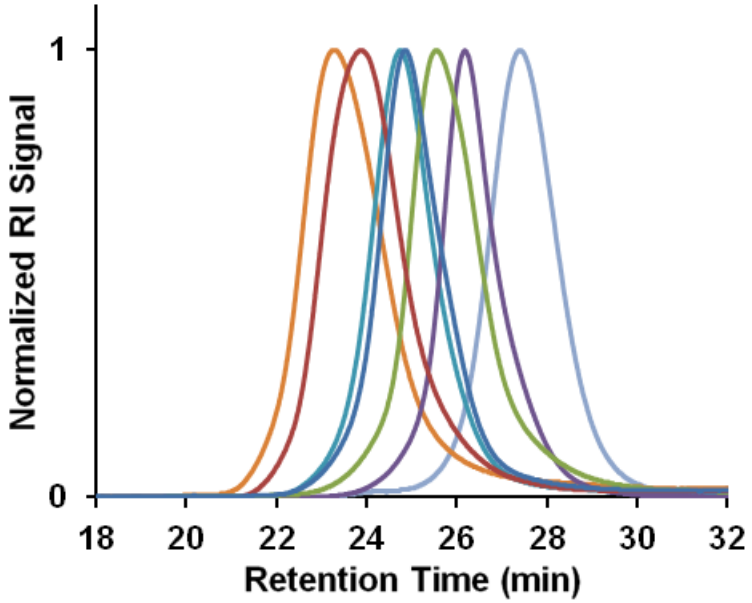

Figure 3.13. GPC traces of spiropyran-linked poly (*iso*-butyl acrylate).

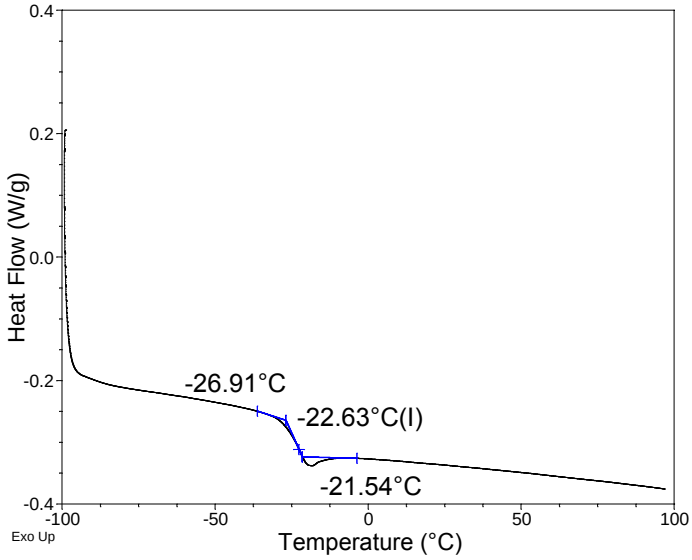

Figure 3.14. DSC trace of P*i*BA (M_n =152) showing glass transition temperature (onset, midpoint, endset).

Table 3.7. Poly(*ter*t-butyl acrylate) characterization

M_n (kDa)	PDI
292	**1.21**
273	**1.26**
226	**1.18**
178	**1.17**
131	**1.12**
89	**1.27**
50	**1.19**

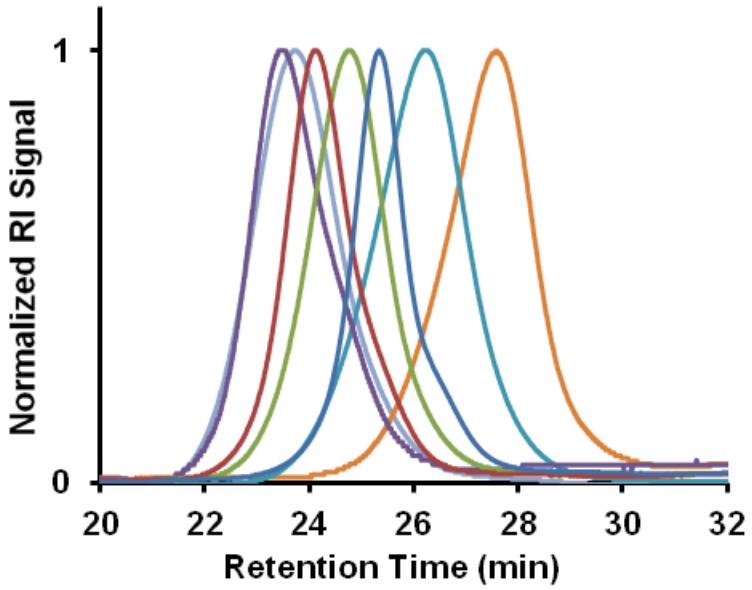

Figure 3.15. GPC traces of spiropyran-linked poly (*tert*-butyl acrylate).

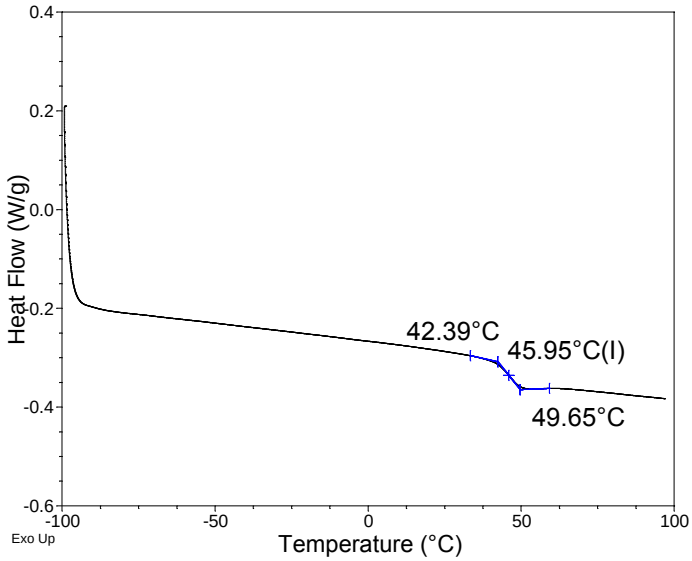

Figure 3.16. DSC trace of P*t*BA (M_n =131) showing glass transition temperature (onset, midpoint, endset).

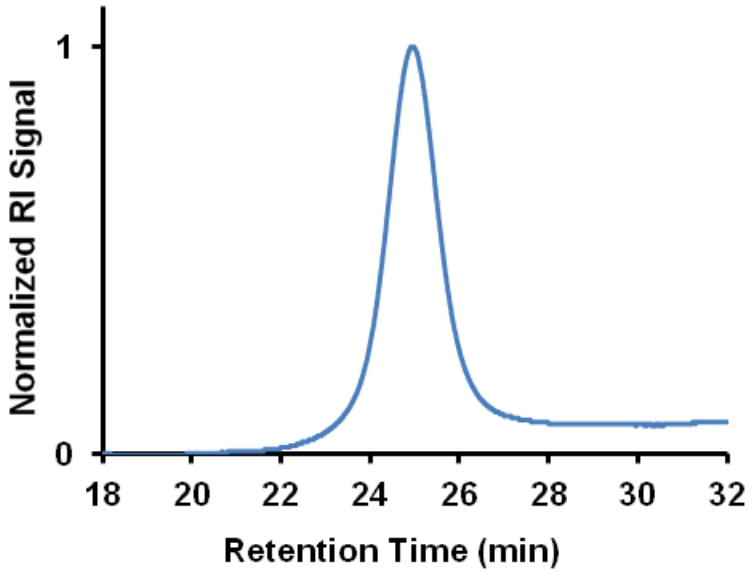

Figure 3.17. GPC trace of PMA control polymer. M_n = 154 kDa, PDI = 1.13.

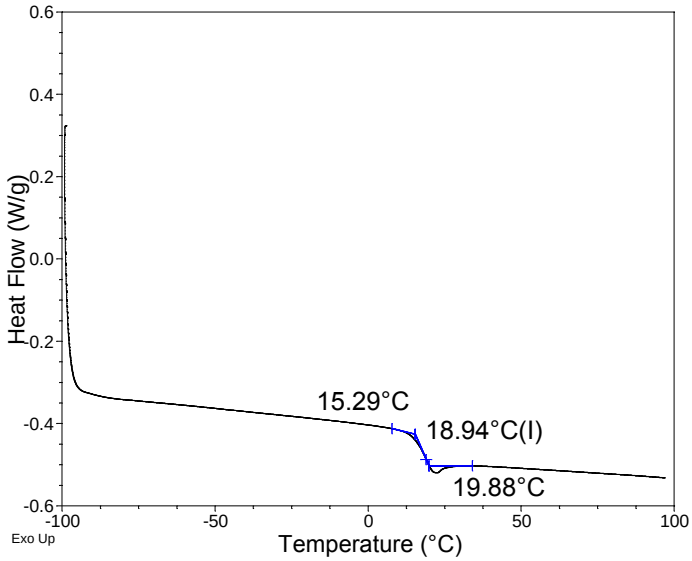

Figure 3.18. DSC trace of PMA control polymer showing glass transition temperature (onset, midpoint, endset).

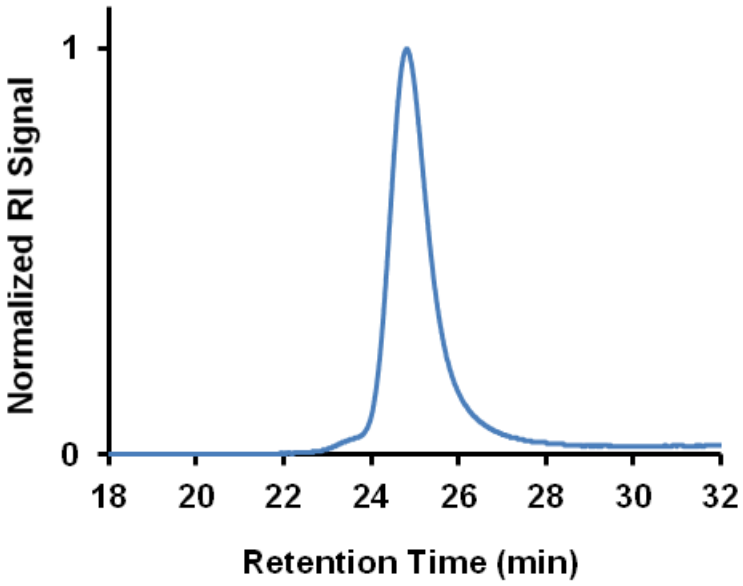

Figure 3.19. GPC trace of PEA control polymer. M_n = 166 kDa, PDI = 1.07.

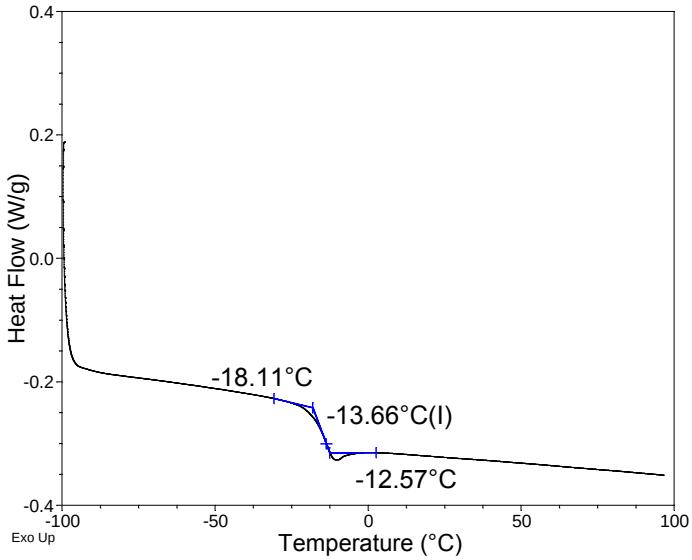

Figure 3.20. DSC trace of PEA control polymer showing glass transition temperature (onset, midpoint, endset).

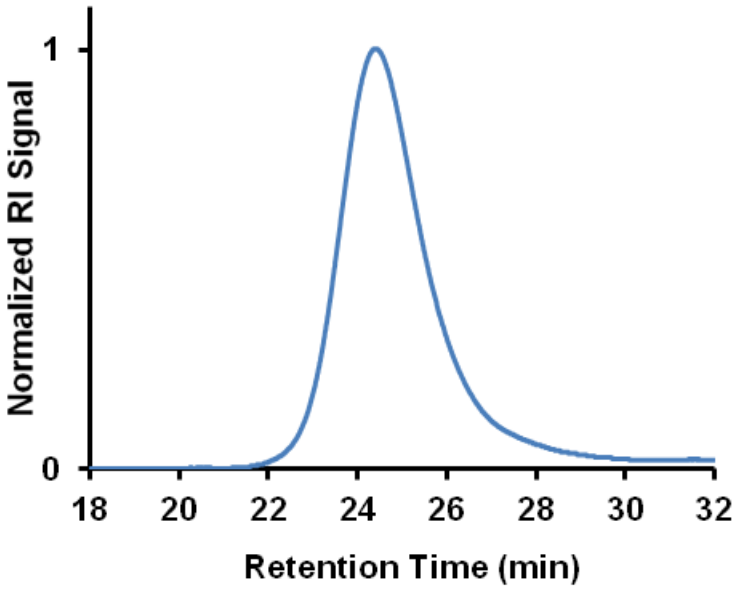

Figure 3.21. GPC trace of P*n*BA control polymer. M_n = 169 kDa, PDI = 1.31.

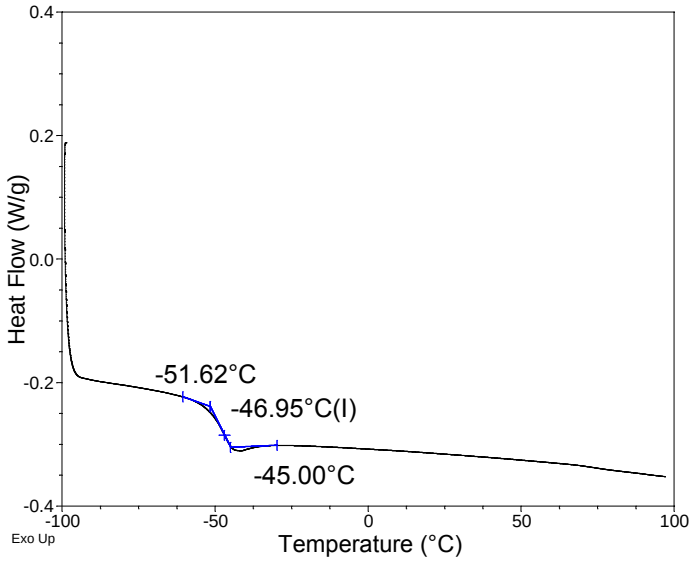

Figure 3.22. DSC trace of P*n*BA control polymer showing glass transition temperature (onset, midpoint, endset).

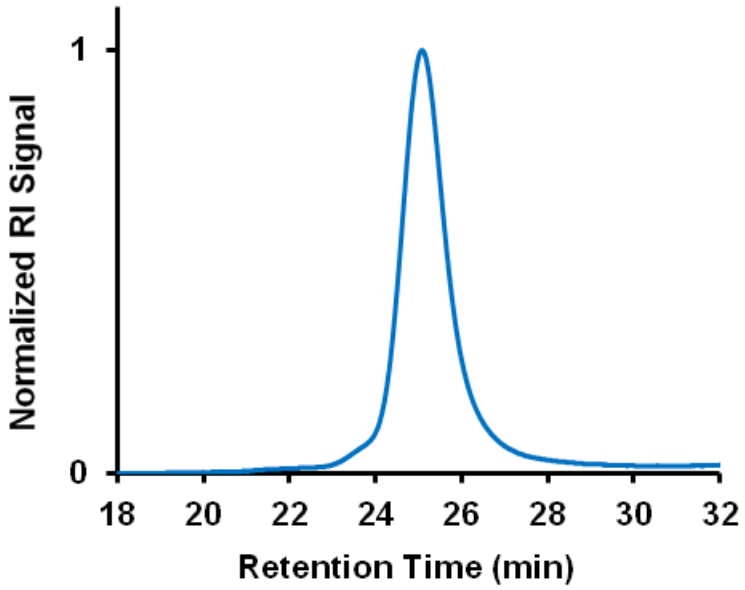

Figure 3.23. GPC trace of P*i*BA control polymer. M_n = 149 kDa, PDI = 1.09.

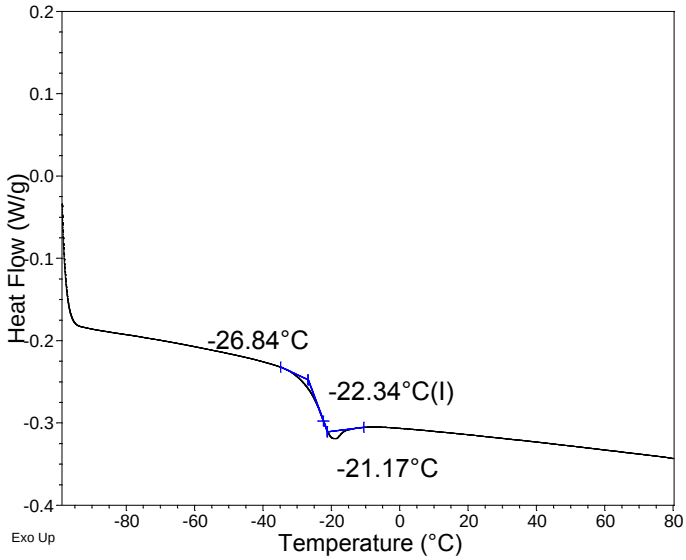

Figure 3.24. DSC trace of P*i*BA control polymer showing glass transition temperature (onset, midpoint, endset).

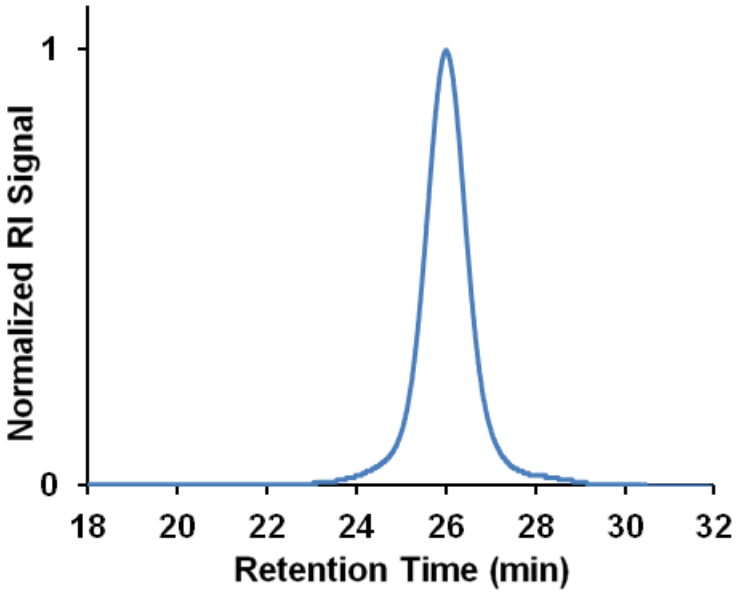

Figure 3.25. GPC trace of P*t*BA control polymer. M_n = 124 kDa, PDI = 1.11

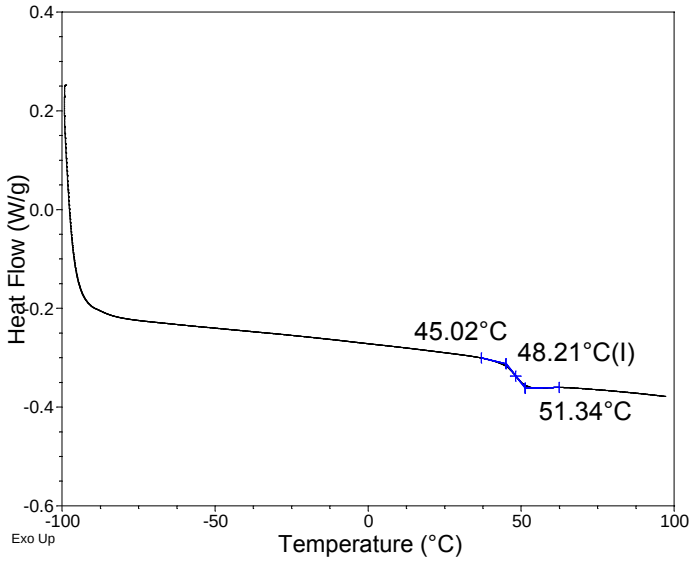

Figure 3.26. DSC trace of P*t*BA control polymer showing glass transition temperature (onset, midpoint, endset).

3.5.3. UV-Vis Absorption Spectra

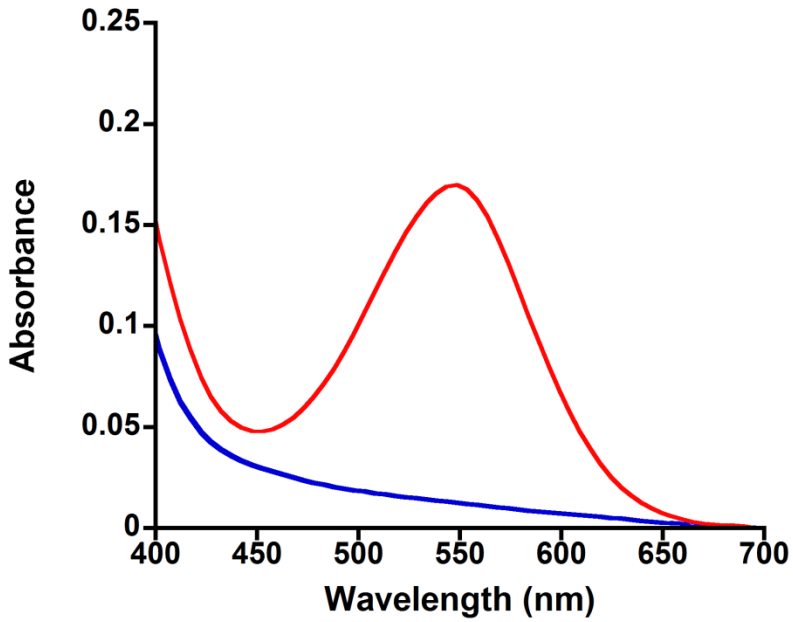

Figure 3.27. Visible absorption spectra of all SP initiators in AcCN before (blue) and after UV irradiation (365 nm) for 5 min (red). λ_{max} = 554 nm.

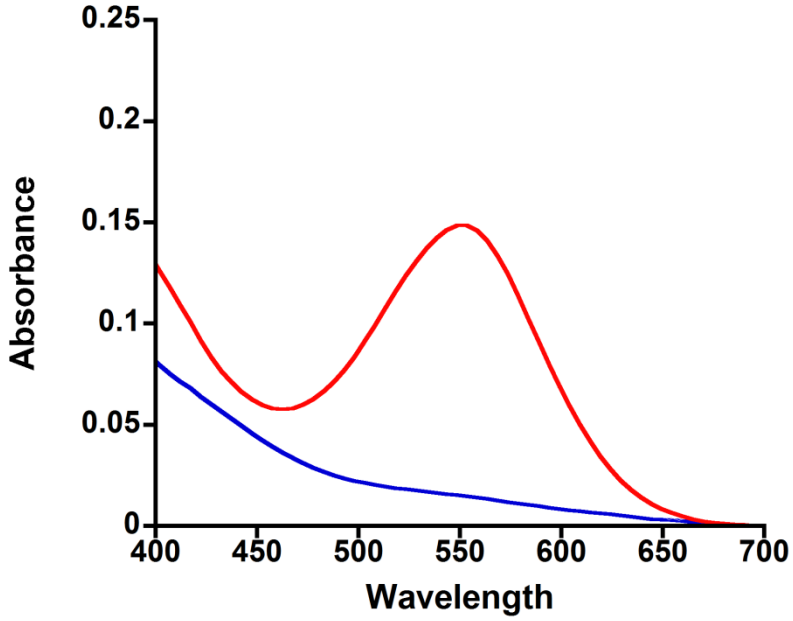

Figure 3.28. Visible absorption spectra of PMA-SP-PMA (270 kDa) in AcCN (1mg/ml) before (blue) and after UV irradiation (365 nm) for 5 min (red). λ_{max} = 554 nm.

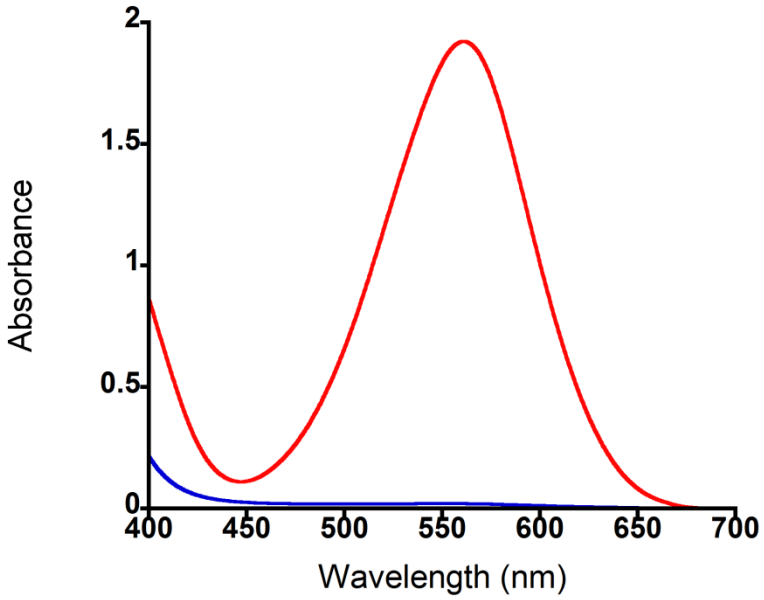

Figure 3.29. Visible absorption spectra of difunctional spiropyran initiator in MEK. Blue trace = spectrum recorded before UV irradiation. Red trace = spectrum recorded after UV irradiation (365 nm) for 2 min. λ_{max} = 570 nm.

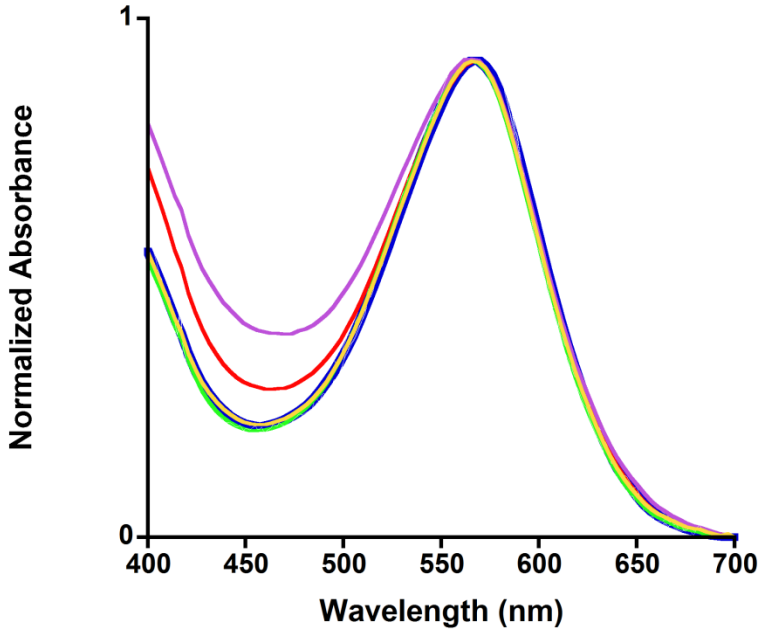

Figure 3.30. Visible absorption spectra of all spiropyran linked poly acrylates in MEK (1mg/ml) after UV irradiation (365 nm) for 5 min. For all polymers λ_{max} = 570 nm. Blue = P*t*BA (292 kDa). Red = P*n*BA (224 kDa). Green = PMA (270 kDa). Purple = P*i*BA (309 kDa). Yellow = PEA (282 kDa). Yellow, green, and blue traces are almost entirely overlapping.

3.5.4 Sonication Calibration

Calorimetry was used to determine power intensities generated by the sonicator.[33] 250 ml of deionized water was added to a small dewar. A thermocouple was placed into the water. The sonicator tip

was lowered into the water about 1 inch and the depth was marked for reproducibility. The sonicator was set to 25% amplitude and the temperature was recorded at 0 s. Sonication was started and the temperature of the water was recorded every 15 s for 4 min. The temperature was plotted against time and the slope of the line was determined ($\frac{\Delta T}{\Delta t}$). This process was repeated for amplitudes of 30%, 35%, 40%, 45% and 50%. The power produced in J/s or W was determined from the following equation:

$$Power = C_p * M * \frac{\Delta T}{\Delta t}$$

Where C_p is the specific heat capacity of the solvent in $\mathrm{J\,g^{-1}\,^{\circ}\,C^{-1}}$, M is the mass of solvent used in g, and $\frac{\Delta T}{\Delta t}$ is the change in temperature as a function of time in $^{\circ}\,\mathrm{C\,s^{-1}}$. 4.179 $\mathrm{J\,g^{-1}\,^{\circ}\,C^{-1}}$ was used as the specific heat capacity of water, 250 g was used for the mass, and the slope of each line was used for the change in temperature with the change in time. The power intensity in W cm^{-2} can be determined from the following equation:

$$Power\ intensity = power/area$$

where area is the surface area of the probe tip in cm. The probe tip is a ½" or 1.27 cm^2.

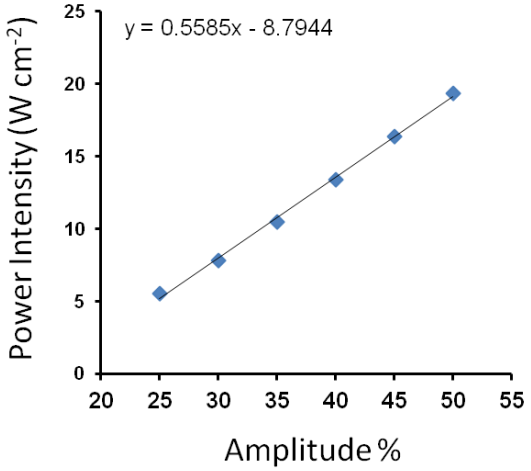

Figure 3.31. Calibration curve of the ultrasonicator.

3.5.5. Ultrasound Flow Cell Set-Up

The general apparatus was assembled as shown in Figure 3.32. Each sonication reaction took place inside the Suslick cell. PTFE tubing was introduced into one arm of the Suslick cell. The diameter of the tubing was increased, stepwise, to fit onto the flow cell cuvette. After the flow cell cuvette, the diameter of the PTFE tubing was again increased to fit the tubing size required for the pump head. After

the pump head, the diameter of the tubing was decreased, stepwise, to match the PTFE tube in the other side arm of the Suslick cell.

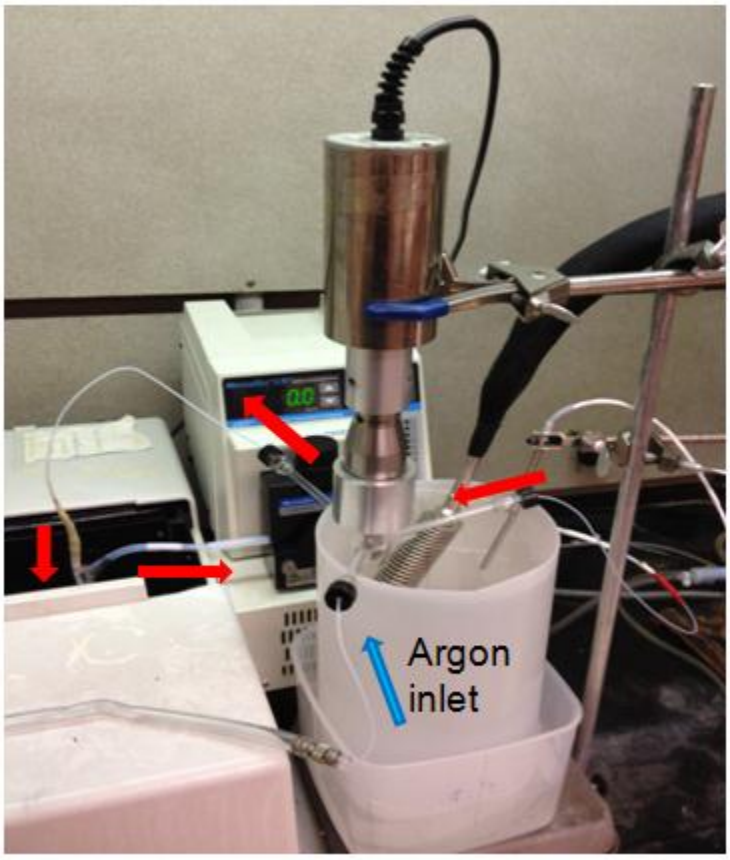

Figure 3.32. General set-up of the sonication flow cell apparatus. Red arrows show the direction of liquid flow. Blue arrow shows the inlet for argon.

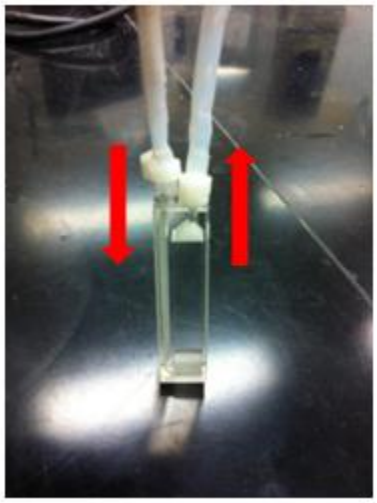

Figure 3.33. Image of the flow cell cuvette. Red arrows show the direction of flow.

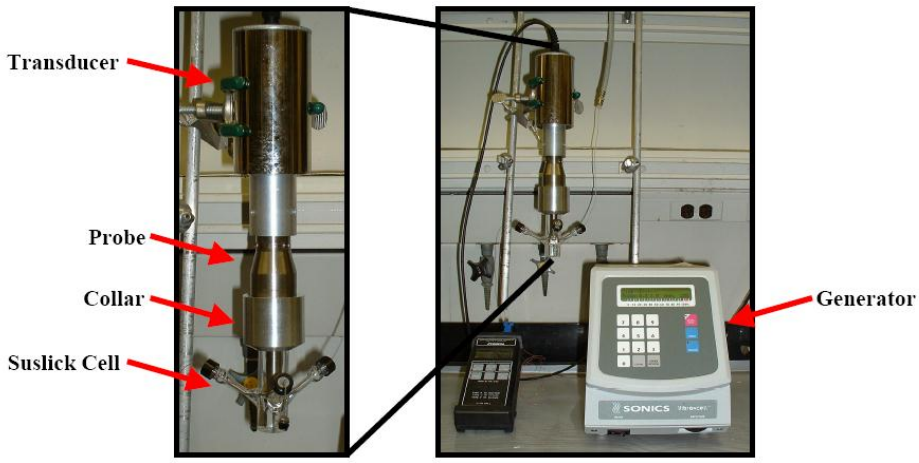

Figure 3.34. General set-up of the sonication apparatus.

3.5.6. General Procedure for Sonication Experiments

The sonication apparatus was assembled as shown in Figures 3.32-3.34. Polymer dissolved at a concentration of 1 mg/ml in acetonitrile or MEK was transferred to an oven-dried Suslick cell, which was placed into the collar and screwed onto the probe. An argon line, an inlet (to return solvent to the Suslick cell) and an outlet (to draw solvent from the Suslick cell) tube were each placed into the three arms of the Suslick cell, respectively. Argon was sparged through the system for 30 min prior to any sonication runs, as well as during the run itself. Following this, the Suslick cell was lowered into the acetone bath for 5 min prior to sonication. Longer cooling times resulted in the solution being so cold that water would condense on the cuvette. After 5 min of cooling, the UV-Vis was started followed immediately by starting sonication. The whole system was kept in the dark during the entire experiment. The temperature of the reaction medium changed as a function of power intensity. Therefore, to compensate for this an appropriate alteration of the temperature of the acetone bath was used (Table 3.8).

Table 3.8. Temperatures of acetone bath for each amplitude used.

Instrument Amplitude (%)	Power Intensity (W cm^{-2})	Acetone Bath Temperature (°C)	Temperature of Solvent in Suslick Cell (°C)
25%	5.17	-11 °C	3-5 °C
35%	10.7	-18 °C	3-5 °C
45%	16.3	-25 °C	3-5 °C

3.5.7. Kinetic Analysis of Mechanophore Activation

Kinetics of the ring-opening of spiropyran have been described by the following single-exponential rise term:[34]

$$A_t = B\left(1 - e^{-kt}\right)$$

where t equals actual sonication time, A_t equals the max absorbance at λ_{max} at time t, B is equal to the amplitude (maximum absorbance value), and k is the rate constant. At any given time, 7.5 ml of solution (out of the total 16 ml) was inside the Suslick cell being irradiated with ultrasound with the remaining 8.5 ml outside of the Suslick cell not subjected to ultrasound. Therefore, actual sonication time was treated as 7.5/16 of real time. Drift in the obtained values were corrected by measuring the absorbance values of λ_{max} and 700 nm during each experiment as shown in Figure 3.35. The drift in absorbance values was unique to each experiment, therefore the absorbance at 700 nm was collected for every experiment in addition to λ_{max} absorbance values and the absorbance values of λ_{max} – 700 nm were used for all calculations. Kaleidagraph software was used for nonlinear least-squares fitting of the data to equation 1 which gives the rate constant k and amplitude B as shown in Figure 3.36.

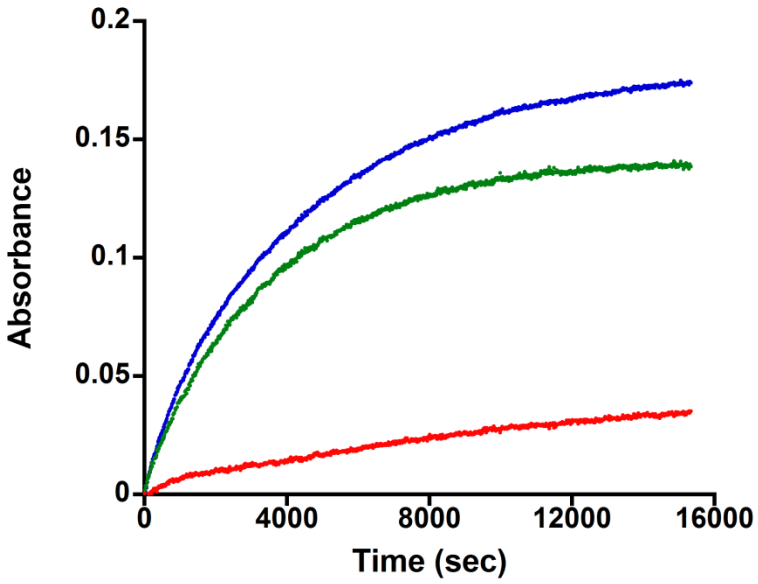

Figure 3.35. Raw data collected for PMA (54 kDa) in acetonitrile at 25% amplitude. Blue = 554 nm absorbance values, red = 700 nm absorbance values, green = abs (554nm) - abs (700nm).

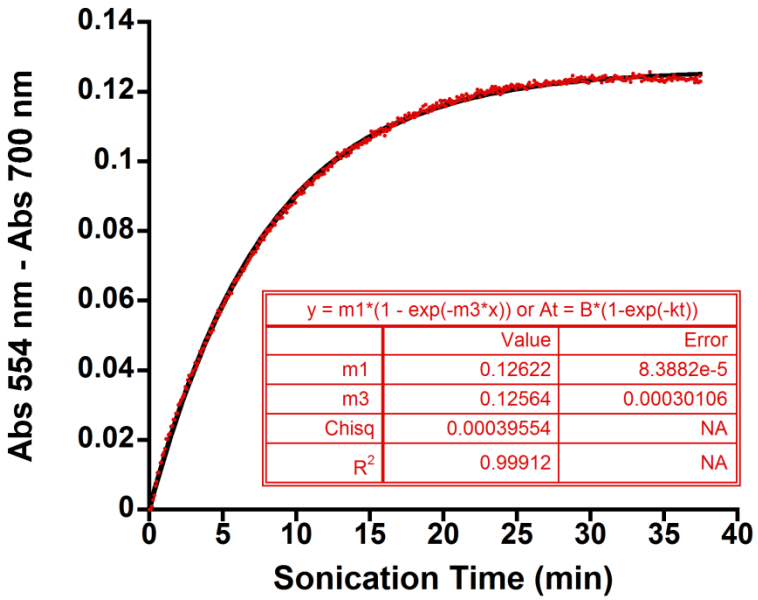

Figure 3.36. Data used for rate calculations directly from Kaleidagraph software. Red data points are measured by UV-Vis and the black curve is generated by fitting the data to the equation: $A_t = B(1 - e^{-kt})$. The rate constant, k, is calculated to be 0.126 min^{-1} (m3 value in Kaleidagraph). Absorbance values are λ_{max} - 700 nm. Sonication time is treated as 7.5/16 of real time. The polymer data shown is for PMA (139 kDa) in acetonitrile at 25% amplitude.

Table 3.9. Measured rate constants of PMA in acetonitrile at various flow rates, 3-5 °C, 1 mg/ml.

	4.5 ml/min	**9 ml/min**	**18 ml/min**
M_n (kDa)	**Rate Constant (min^{-1})**	**Rate Constant (min^{-1})**	**Rate Constant (min^{-1})**
54	0.054	0.049	0.0422
102	0.16	0.137	0.14
139	0.254	0.2285	0.242
156	0.33	0.337	0.3235
184	0.42	0.38	0.375
194	0.424	0.4005	0.38
270	0.67	0.675	0.677

Table 3.10. Measured rate constants of PMA in acetonitrile at various power intensities (4.5ml/min flow rate, 1mg/ml).

	25%	35%	45%
M_n (kDa)	Rate Constant (min^{-1})	Rate Constant (min^{-1})	Rate Constant (min^{-1})
54	0.044	0.054	0.0765
102	0.09185	0.16	0.1735
139	0.1265	0.254	0.305
156	0.1785	0.33	0.403
184	0.1915	0.42	0.545
194	0.2545	0.424	0.53
270	0.4012	0.67	0.87

Table 3.11. Measured rate constants of PMA, PEA, PnBA, PiBA, and PtBA in MEK at 35% amp, 3-5 °C, 1 mg/ml.

PMA		PEA		PnBA		PiBA		PtBA	
M_n	Rate	M_n	Rate	M_n	Rate	M_n	Rate	M_n	Rate
54	0.154	49	0.11	60	0.0594	60	0.09	50	0.10165
102	0.2535	77	0.1685	87	0.1744	81	0.1415	93	0.175
139	0.35	96	0.211	98	0.1694	152	0.2955	131	0.202
156	0.432	121	0.25	137	0.2494	167	0.355	178	0.3078
194	0.5815	155	0.3555	184	0.38	239	0.47	226	0.495
270	0.81	177	0.415	224	0.4383	309	0.61	273	0.575
		233	0.569					292	0.61
		282	0.73						

3.5.8. Statistical Analysis for Comparison of Two Slopes[13,30]

A pairwise comparison between each flow rate tested was performed to test for statistical differences in slope. Example calculations for the comparison of the 4.5ml/min flow rate and 9ml/min flow rate are as follows (all other comparisons were done in a similar manner using Microsoft Excel for data analysis). For this particular *t* test, the null (H_0) hypothesis is that the slopes are statistically indistinguishable. The alternative (H_a) hypothesis is that the slopes are statistically different from each

other. Table 3.12 shows the experimental rate data for the 4.5 ml/min flow rate experiments. The rates in the table are an average of two analyzed sonication runs.

Table 3.12. Experimental rate data for 4.5 ml/min flow rate experiments.

M_n (kDa)	Rate Constant (min^{-1})
54	0.054
102	0.16
139	0.25
156	0.33
184	0.42
194	0.42
270	0.67

From this data, the average X value (molecular weight) can be calculated using the following equation:

$$\bar{X} = \sum \frac{X_i}{n}$$

and the average Y value (rate) can be calculated using the following equation

$$\bar{Y} = \sum \frac{Y_i}{n}$$

Where n = 7 due their being six data points in this series of polymers. Using the above data set (Table 3.12), $\bar{X}$ is equal to 157 kDa and $\bar{Y}$ is equal to 0.33 min^{-1}. Using these averages, the slope (b) for the regression line is calculated with the following equation:

$$b = \frac{\sum[(X_i - \bar{X}) * (Y_i - \bar{Y})]}{\sum(X_i - \bar{X})^2}$$

Using the data in table 3.13 below, the slope value for the 4.5 ml/min series was calculated to be b = 2.9 x 10^{-3} $\frac{\mathrm{min}^{-1}}{\mathrm{kDa}}$.

Table 3.13. Summary of values calculated for the 4.5 ml/min flow rate series.

M_n (kDa)	$(X_i - \bar{X})^2$	$(X_i - \bar{X}) * (Y_i - \bar{Y})$	$(Y_i - \bar{Y})^2$	Rate (min^{-1})
54	10609	28.45743	0.076334	0.054
102	3025	9.365714	0.028997	0.16
139	324	1.373143	0.00582	0.254
156	1	0.000286	8.16E-08	0.33
184	729	2.422286	0.008049	0.42
194	1369	3.467429	0.008782	0.424
270	12769	38.38771	0.115406	0.67
SUM	**28826**	**83.474**	**0.243387**	

Next, the residual sum of squares (SS) for the 4.5 ml/min flow rate series using the following equation:

$$SS = \sum (Y_i - \bar{Y})^2 - \frac{\langle \sum [(X_i - \bar{X}) * (Y_i - \bar{Y})] \rangle^2}{\sum (X_i - \bar{X})^2}$$

which in the case of the 4.5 ml/min series, SS = 0.0017. Additionally, the residual degrees of freedom for the system can be calculated using the following equation:

$$residual\ DF = n - 2$$

which in the case of the 4.5 ml/min series is 5.

Similar calculations for the 9 ml/min flow rate series were performed. Calculated values obtained are the following:

$\bar{X}$ = 157 kDa

$\bar{Y}$ = 0.32 min^{-1}

b = 2.9 x 10^{-3} $\frac{min^{-1}}{kDa}$

$n = 7$

$SS = 0.0049$

$residual\ DF = 5$

Table 3.14. Summary of values calculated for the 9 ml/min flow rate series.

M_n (kDa)	$(X_i - \bar{X})^2$	$(X_i - \bar{X}) * (Y_i - \bar{Y})$	$(Y_i - \bar{Y})^2$	Rate (min^{-1})
54	10609	27.42743	0.070908	0.054
102	3025	9.805714	0.031786	0.16
139	324	1.562143	0.007532	0.254
156	1	-0.02171	0.000472	0.33
184	729	1.747286	0.004188	0.42
194	1369	3.152929	0.007261	0.424
270	12769	40.64771	0.129394	0.67
SUM	**28826**	**84.3215**	**0.251541**	

3.5.9. Direct Statistical Comparison of Slopes[13,30]

Using the data and values calculated above, it is possible to directly investigate for statistical significance in the difference in slope between the two data sets. In order to do this analysis, the pooled residual mean square must be calculated using the following equation:

$$(s^2_{Y*X})_p = \frac{SS_{4.5} + SS_9}{DF_{4.5} + DF_9}$$

Using the above values above for both the 4.5 ml/min and 9 ml/min flow rates, a pooled residual mean square value of 6.5 x 10^{-4} was obtained. Following this, the standard error of the difference between regression coefficients was calculated using the following equation:

$$s_{b_1 - b_2} = \sqrt{\frac{(s^2_{Y*X})_p}{[\sum(X_i - \bar{X})^2]_{4.5}} + \frac{(s^2_{Y*X})_p}{[\sum(X_i - \bar{X})^2]_9}}$$

Using the pooled residual mean square value found above and summation values from Table 3.13 and 3.14, the standard error was calculated to be 2.1 x 10^{-4} for the comparison of the 4.5 ml/min and 9 ml/min flow rates. Finally, the *t* value needed to test the null hypothesis was calculated with the following equation:

$$t = \left| \frac{b_{4.5} - b_9}{s_{b_1 - b_2}} \right|$$

For the 4.5 ml/min and 9 ml/min flow rates, the *t* value obtained was *t* = 0.138. In order to compare this value to the critical *t* value to test for statistical significance, the sum of the residual degrees of freedom must be determined using the following equation:

$$v = DF_{4.5} + DF_9$$

where for this case, *v* = 10. We can reject the null hypothesis if $|t| \leq t_{\alpha(2),v}$. Searching a table of *t* values, the critical *t* value to show statistical significance with 95% confidence using a two tail test and a *v* of 10 is 2.23. Because the experimentally determined *t* value (0.138) is *not greater than* the minimum *t* value (2.23) we cannot reject the null hypothesis, and therefore it is concluded that the two slopes are *not statistically different* from each other.

3.5.10. Statistical Analysis for Comparison of Two Elevations[13,30]

If there is no statistical difference in slope between two linear regressions it is possible to test for statistical differences in the elevations (X-intercept). Calculations for pairwise comparison of 4.5 ml/min and 9 ml/min flow rates are shown as an example. All other calculations were done with the following equations in Microsoft Excel.

For this particular *t* test, the null (H_0) hypothesis is that the elevations are statistically indistinguishable. The alternative hypothesis (H_a) is that the elevations are statistically different from each other.

In order to perform this *t* test comparing the two data sets, it was necessary to calculate the following values. The sum of the squares for X (molecular weight) for common regression can be calculated by the following equation:

$$A_c = \sum (X_i - \bar{X})^2{}_{4.5} + \sum (X_i - \bar{X})^2{}_{9}$$

Where $\sum (X_i - \bar{X})^2$ for both the 4.5 ml/min and 9 ml/min flow rates can be found in Tables 3.13 and 3.14, respectively. In the case of these flow rates compared, $A_c = 57652$. Similarly, the sum of the crossproducts for common regression can be calculated using the following equation:

$$B_c = \sum [(X_i - \bar{X}) * (Y_i - \bar{Y})]_{4.5} + \sum [(X_i - \bar{X}) * (Y_i - \bar{Y})]_9$$

where $\sum [(X_i - \bar{X}) * (Y_i - \bar{Y})]$ for both flow rates tested can again be found in Tables 3.13 and 3.14, respectively. For the flow rates tested here, $B_c = 167.796$. Finally, the sum of squares Y (rate) for common regression can be calculated using the following equation:

$$C_c = \sum (Y_i - \bar{Y})^2_{4.5} + \sum (Y_i - \bar{Y})^2_9$$

where $\sum(Y_i - \bar{Y})^2$ for both flow rates can be found in Tables S12 and S13, respectively. In the case of these flow rates, $C_c = 0.495$. The common slope for the two data sets can be calculated using the following equation:

$$b_c = \frac{\mathrm{B_c}}{\mathrm{A_c}}$$

which in this case leads to a common slope for the 4.5 ml/min and 9 ml/min flow rates of 2.9 x 10^{-3} $\frac{min^{-1}}{kDa}$. Furthermore, the residual sum of squares (*SS*) for common regression can be calculated using the following equation:

$$SS_c = C_c - \frac{B_c^2}{A_c}$$

giving a value of 6.6 x 10^{-3}. The residual degree of freedom (*DF*) for common regression can be calculated using the following equation:

$$DF_c = n_{4.5} + n_9 - 3$$

which for this case gives $DF_c = 11$. This allows the calculation of the residual mean square for common regression using the following equation:

$$(s^2_{Y*X})_c = \frac{SS_c}{DF_c}$$

which is equal to 6.4 x 10^{-4} for this case. Finally, with all the above values and equations, it is possible to calculate a *t* value for the pairwise comparison of elevations using the following equation:

$$t = \frac{(\bar{Y}_{4.5} - \bar{Y}_9) - b_c * (\bar{X}_{4.5} - \bar{X}_9)}{\sqrt{(s^2_{Y*X})_c * \left[\frac{1}{n_{4.5}} + \frac{1}{n_9} + \frac{(\bar{X}_{4.5} - \bar{X}_9)^2}{A_c}\right]}}$$

For the two flow rates presented here, 4.5 ml/min and 9 ml/min, a *t* value of 1.10 was obtained using the method outlined above. Similar to the slope comparison *t* test, we can reject the null hypothesis if $|t| \leq t_{\alpha(2),\nu}$. Upon searching a table of *t* values, and finding the critical *t* value for $DF_c = 11$ and at a 95% confidence interval, we see the minimum *t* value needed to show statistical difference is 2.20. Because the calculated *t* value (1.10) is *not greater than* the minimum *t* value (2.20), we cannot reject the null hypothesis and can conclude that there is not statistical difference in elevation between these two flow rates tested.

Table 3.15. Flow rate study-Pairwise comparison of slopes based on calculated *t* values and minimum *t* values necessary for statistical significance. Calculated *t* values are listed with minimum *t* values below in parentheses. None of these comparisons gave slopes that are statistically different at the 95% confidence level.

		Flow Rate 1		
		4.5 ml/min	**9 ml/min**	**18 ml/min**
Flow Rate 2	**4.5 ml/min**	-	-	-
	9 ml/min	0.138 (2.23)	-	-
	18 ml/min	0.0804 (2.23)	0.0487 (2.23)	-

Table 3.16. Flow Rate Study-Pairwise comparison of elevations based on calculated *t* values and minimum *t* values necessary for statistical significance. Calculated *t* values are listed with minimum *t* values below in parentheses. None of these comparisons gave slopes that are statistically different at the 95% confidence level.

		Flow Rate 1		
		4.5 ml/min	**9 ml/min**	**18 ml/min**
Flow Rate 2	**4.5 ml/min**	-	-	-
	9 ml/min	1.10 (2.20)	-	-
	18 ml/min	1.41 (2.20)	0.238 (2.20)	-

Table 3.17. Power Intensity Study-Pairwise comparison of slopes based on calculated *t* values and minimum *t* values necessary for statistical significance. Calculated *t* values are listed with minimum *t* values below in parentheses. All of these comparisons gave slopes that are statistically different at the 95% confidence level.

		Power Amplitude 1		
		25%	**35%**	**45%**
Power Amplitude 2	**25%**	-	-	-
	35%	6.18 (2.23)	-	-
	45%	7.45 (2.23)	3.52 (2.23)	-

Table 3.18. Polymer Architecture Study (Rate Constant vs Molecular Weight)-Pairwise comparison of slopes based on calculated *t* values and minimum *t* values necessary for statistical significance. Calculated *t* values are listed with minimum *t* values below in parentheses. Green values are slopes that are statistically different at the 95% confidence level. Red values are slopes that are not statistically different at the 95% confidence level.

		Polymer Type 1				
		PMA	**PEA**	**P*n*BA**	**P*i*BA**	**P*t*BA**
Polymer Type 2	**PMA**	-	-	-	-	-
	PEA	2.65 (2.23)	-	-	-	-
	P*n*BA	3.68 (2.31)	2.53 (2.23)	-	-	-
	P*i*BA	5.79 (2.31)	5.08 (2.23)	0.976 (2.31)	-	-
	P*t*BA	3.74 (2.26)	2.62 (2.20)	0.135 (2.26)	0.712 (2.26)	-

Table 3.19. Polymer Architecture Study (Rate Constant vs Molecular Weight)--Pairwise comparison of elevations based on calculated *t* values and minimum *t* values necessary for statistical significance. Calculated *t* values are listed with minimum *t* values below in parentheses. None of these comparisons gave slopes that are statistically different at the 95% confidence level.

		Polymer Type 1		
		P*n*BA	**P*i*BA**	**P*t*BA**
Polymer Type 2	**P*n*BA**	-	-	-
	P*i*BA	0.0307 (2.26)	-	-
	P*t*BA	0.273 (2.23)	0.248 (2.23)	-

Table 3.20. Polymer Architecture Study (Rate Constant vs Degree of Polymerization)-Pairwise comparison of slopes based on calculated *t* values and minimum *t* values necessary for statistical significance. Calculated *t* values are listed with minimum *t* values below in parentheses. None of these comparisons gave slopes that are statistically different at the 95% confidence level.

		Polymer Type 1				
		PMA	**PEA**	**P*n*BA**	**P*i*BA**	**P*t*BA**
Polymer Type 2	**PMA**	-	-	-	-	-
	PEA	0.269 (2.23)	-	-	-	-
	P*n*BA	0.606 (2.31)	0.989 (2.23)	-	-	-
	P*i*BA	0.254 (2.31)	0.0243 (2.23)	0.976 (2.31)	-	-
	P*t*BA	0.526 (2.26)	0.852 (2.20)	0.0912 (2.26)	0.746 (2.26)	-

Table 3.21. Polymer Architecture Study (Rate Constant vs Degree of Polymerization)-Pairwise comparison of elevations based on calculated *t* values and minimum *t* values necessary for statistical significance. Calculated *t* values are listed with minimum *t* values below in parentheses. None of these comparisons gave slopes that are statistically different at the 95% confidence level.

		Polymer Type 1				
		PMA	**PEA**	**P*n*BA**	**P*i*BA**	**P*t*BA**
Polymer Type 2	**PMA**	-	-	-	-	-
	PEA	0.186 (2.20)	-	-	-	-
	P*n*BA	1.19 (2.26)	1.48 (2.20)	-	-	-
	P*i*BA	1.44 (2.26)	2.11 (2.20)	0.286 (2.26)	-	-
	P*t*BA	01.55 (2.23)	1.89 (2.18)	0.287 (2.23)	0.393 (2.23)	-

3.5.11. Thermal Reversion Experiments

The reverse ring closing reaction from the merocyanine to the closed spiropyran form was analyzed for all polymers.[35,36] Polymers were irradiated at 365 nm for 5 min to shift the equilibrium to the merocyanine photostationary state. The polymer solutions were allowed to thermally revert to the closed spiropyran form in the flow cell system with the temperature matched to the sonication experiments to reproduce, as closely as possible, the conditions of sonication (excluding sonication). To achieve this, the acetone bath was set to 2 °C, which achieved a temperature of 3-5 °C in the Suslick cell which matched the sonication experiments. The rate of the reverse reaction was determined from the first order rate law ($-dA/dt = k_{obs} A$) in its logarithmic form:

$$ln\left(\frac{A_t - A_f}{A_o - A_f}\right) = -k_r t$$

where A_0 and A_t are the absorbance at λ_{max} at 0 min and *t* min, respectively. A_f is the absorbance of the solution at λ_{max} before irradiation, and k_r is the observed rate constant for thermal reversion. Thermal reversion was found to be slower in acetonitrile than in MEK for PMA. The calculated rate constant for

PMA in acetonitrile was 7.1 x 10^{-3} min^{-1}. The calculated rate constants in MEK were found to be 1.6 x10^{-2} min^{-1} for PMA, 1.6 x10^{-2} min^{-1} for PEA, 1.7 x10^{-2} min^{-1} for PBA, 1.5 x10^{-2} min^{-1} for PiBA, and 1.8 x10^{-2} min^{-1} for PtBA. Thermal reversions for all polymer architectures in MEK were almost identical and therefore electronic contributions of the local polymer environment are not likely the source of differences in mechanochemical activation. The thermal reversion rate constants were also significantly slower than the forward ring-opening reaction and were not included in calculating mechanochemical activation rate constants.

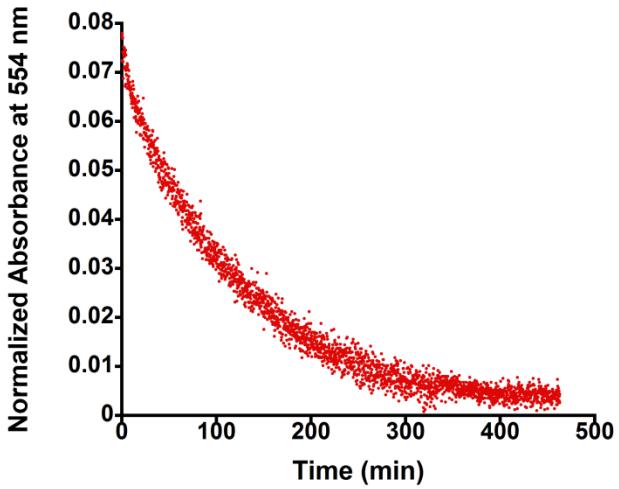

Figure 3.37. Reversion data for PMA in acetonitrile.

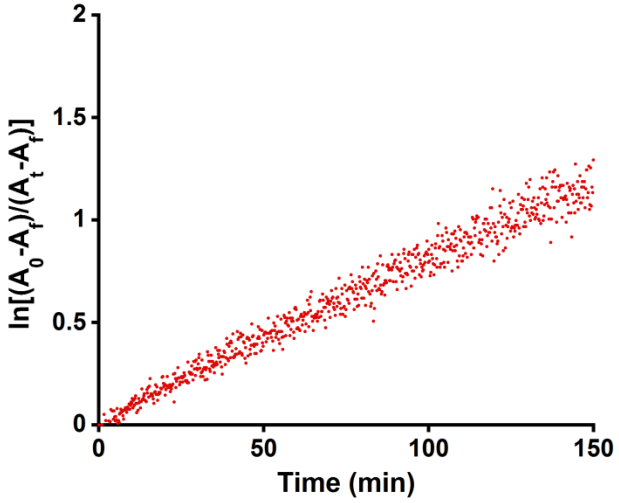

Figure 3.38. Reversion data for PMA in acetonitrile calculated using first order kinetics. The slope of the line is equal to k_r.

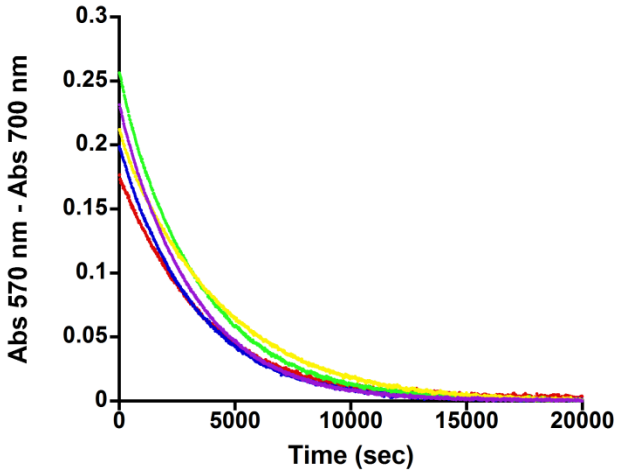

Figure 3.39. Reversion data in MEK. Red is PMA (156 kDa). Blue is PEA (155 kDa). Green is P*n*BA (137 kDa). Yellow is P*i*BA (155 kDa). Purple is P*t*BA (131 kDa).

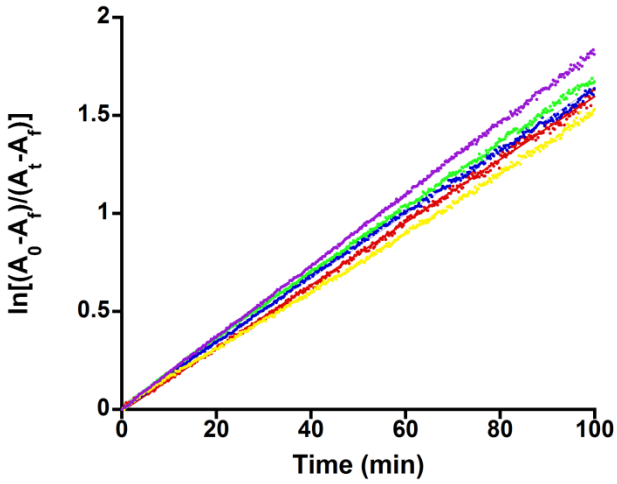

Figure 3.40. Reversion data calculated using first order kinetics. The slopes of the lines are equal to k_r. Red is PMA (156 kDa). Blue is PEA (155 kDa). Green is P*n*BA (137 kDa). Yellow is P*i*BA (155 kDa). Purple is P*t*BA (131 kDa).

3.5.12. Control Experiments

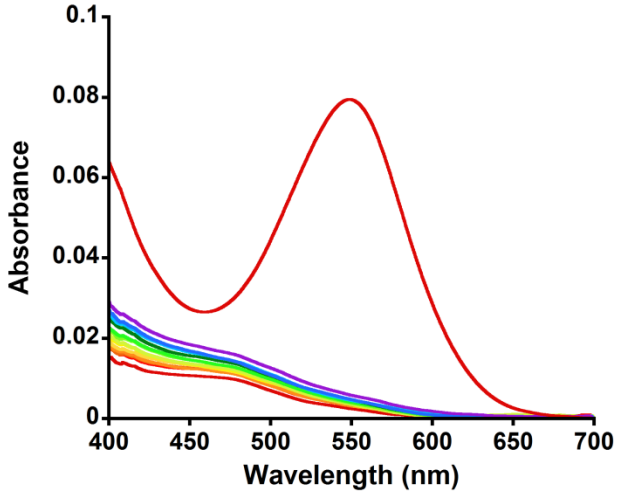

Figure 3.41. UV-Vis absorption spectra of control PMA during sonication in acetonitrile at 25% amplitude. 15 spectra collected at 2 minute intervals for a total of 30 min sonication. No change is observed. Red line = absorption spectrum of post-sonication polymer irradiated with 254 nm light showing that the spiropyran is UV active.

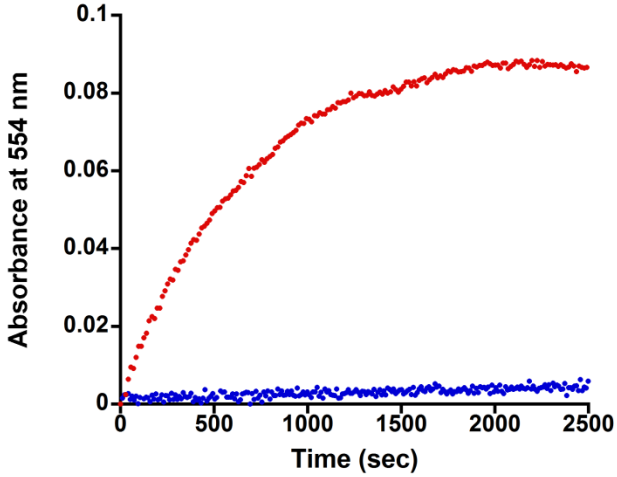

Figure 3.42. Absorbance at 554 nm of 156 kDa PMA (red) and 154 kDa PMA control polymer (blue) during sonication in acetonitrile. 25% amplitude. 1 mg/ml. 3-5°C.

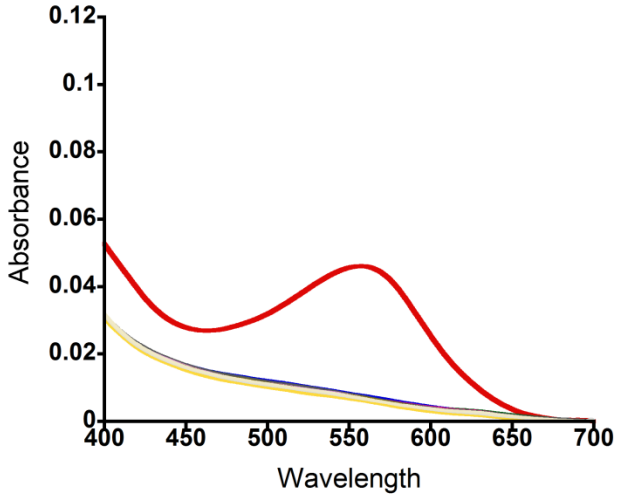

Figure 3.43. UV-Vis absorption spectra of control PMA during sonication in MEK. 15 spectra collected at 2 minute intervals for a total of 30 min sonication. 35% amplitude. No change is observed. Red line = absorption spectrum of post-sonication polymer irradiated with 365 nm light showing that the spiropyran is UV active.

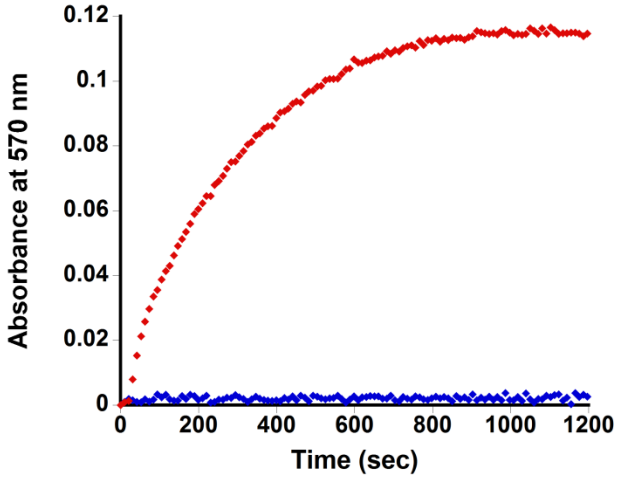

Figure 3.44. Absorbance at 570 nm of 156 kDa PMA (red) and 154 kDa PMA control polymer (blue) during sonication in MEK. 35% amplitude. 1 mg/ml. 3-5 degrees.

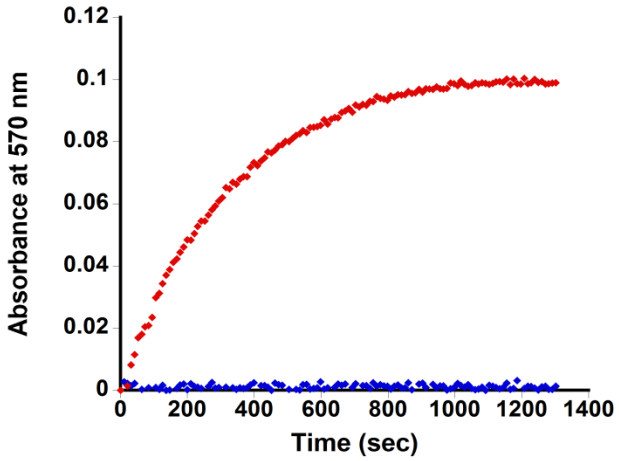

Figure 3.45. Absorbance at 570 nm of 177 kDa PEA (red) and 166 kDa PEA control polymer (blue) during sonication in MEK. 35% amplitude. 1mg/ml. 3-5 degrees.

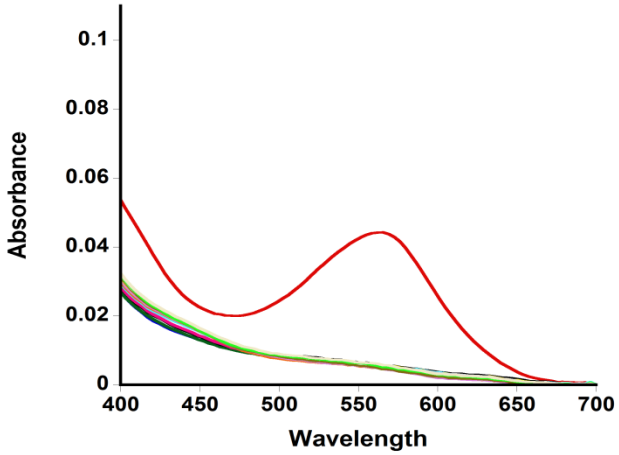

Figure 3.46. UV-Vis absorption spectra of control PEA during sonication. 15 spectra collected at 2 minute intervals for a total of 30 min sonication. 35% amplitude. No change is observed. Red line = absorption spectrum of post-sonication polymer irradiated with 365 nm light showing that the spiropyran is UV active.

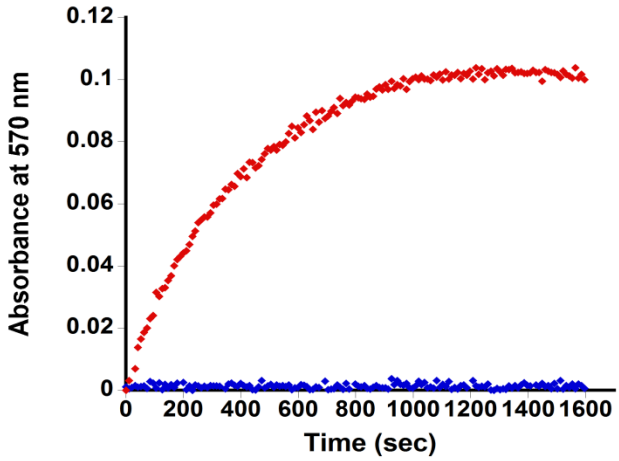

Figure 3.47. Absorbance at 570 nm of 139 kDa P*n*BA (red) and 169 kDa P*n*BA control polymer (blue) during sonication in MEK. 35% amplitude.

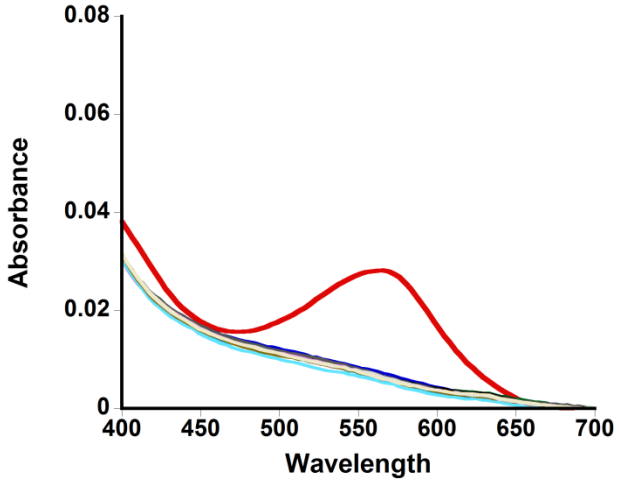

Figure 3.48. UV-Vis absorption spectra of control P*n*BA during sonication. No change is observed. Red line = absorption spectrum of post-sonication polymer irradiated with 365 nm light showing that the spiropyran is UV active.

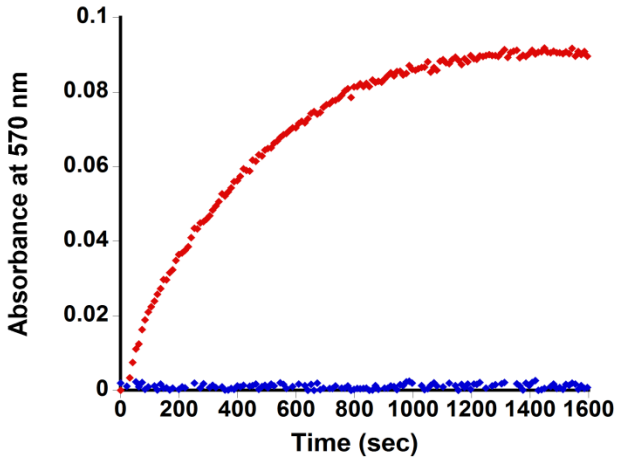

Figure 3.49. Absorbance at 570 nm of 152 kDa P*i*BA (red) and 149 kDa P*i*BA control polymer (blue) during sonication.

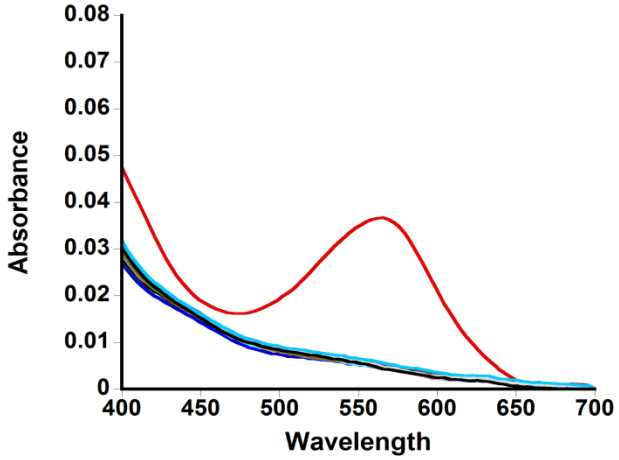

Figure 3.50. UV-Vis absorption spectra of control P*i*BA during sonication. No change is observed. Red line = absorption spectrum of post-sonication polymer irradiated with 365 nm light showing that the spiropyran is UV active.

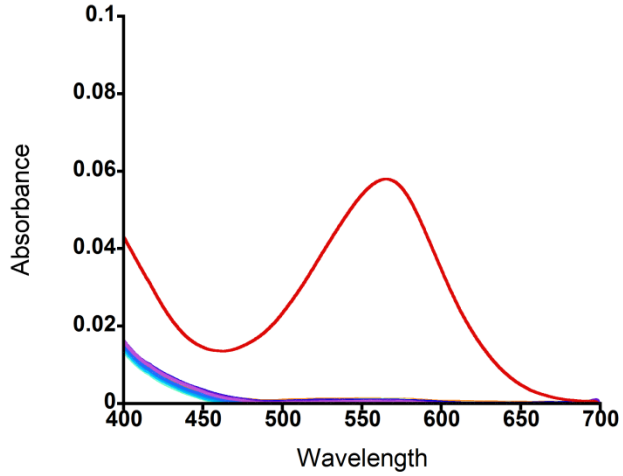

Figure 3.51. UV-Vis absorption spectra of control P*t*BA during sonication. No change is observed. Red line = absorption spectrum of post-sonication polymer irradiated with 365 nm light showing that the spiropyran is UV active.

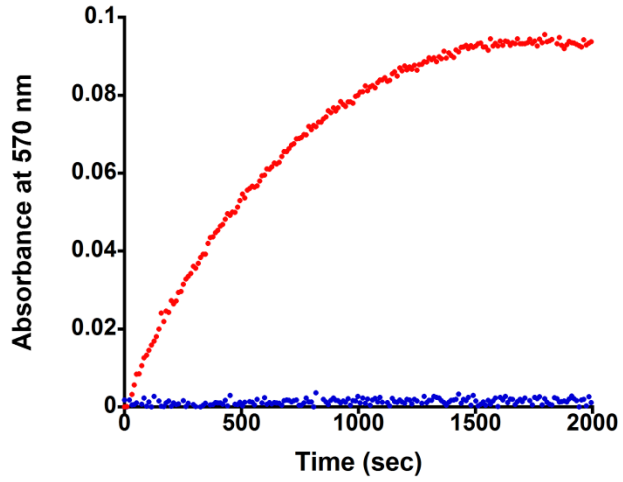

Figure 3.52. Absorbance at 570 nm of 124 kDa P*t*BA (red) and 131 kDa P*t*BA control polymer (blue) during sonication.

3.6. REFERENCES

(1) Caruso, M. M.; Davis, D. A.; Shen, Q.; Odom, S. A.; Sottos, N. R.; White, S. R.; Moore, J. S. *Chem. Rev*. **2009**, *109*, 5755-5798.

(2) Kean, Z. S.; Craig, S. L. *Polymer*, **2012**, *53*, 1035-1048.

(3) Wiggins, K. M.; Brantley, J. N.; Bielawski, C. W. *Macro Lett*. **2012**, *1*, 623-626.

(4) May, P. A.; Moore, J. S. *Chem. Soc. Rev*. **2013**. DOI: 10.1039/C2CS35463B.

(5) Tennyson, A. G.; Wiggins, K. M.; Bielawski, C. W. *J. Am. Chem. Soc*. **2010**, *132*, 16631-16636.

(6) Groote, R.; Jakobs, R. T. M.; Sijbesma, R. P. *Macro. Lett*. **2012**, *1*, 1012-1015.

(7) Kryger, M. J.; Ong, M. T.; Odom, S. A.; Sottos, N. R.; White, S. R.; Martinez, T. J.; Moore, J. S. *J. Am. Chem. Soc*. **2010**, *132*, 4558-4559.

(8) Ciardelli, F.; Ruggeri, G.; Pucci, A. *Chem. Soc. Rev*. **2013**, *42*, 857-870.

(9) Diesendruck, C. E.; Steinberg, B. D.; Sugai, N.; Silberstein, M. N.; Sottos, N. R.; White, S. R.; Braun, P. V.; Moore, J. S. *J. Am. Chem. Soc*. **2012**, *134*, 12446-12449.

(10) Brantley, J. N.; Wiggins, K. M.; Bielawski, C. W. *Polym. Int*. **2012**, *62*, 2-12.

(11) Wiggins, K. M.; Brantley, J. N.; Bielawski, C. W. *Chem. Soc. Rev*. **2013**. DOI:10.1039/C3CS35493H

(12) Cravotto, G.; Gaudino, E. C.; Cintas, P. *Chem. Soc. Rev*. **2013**. DOI:10.1039/C2CS35456J

(13) Kryger, M. J.; Munaretto, A. M.; Moore, J. S. *J. Am. Chem. Soc*. **2011**, *133*, 18992-18998.

(14) Brantley, J. N.; Konda, S. S. M.; Makarov, D. E.; Bielawski, C. W. *J. Am. Chem. Soc*. **2012**, *134*, 9982-9985.

(15) Ribas-Arino, J.; Shiga, M.; Marx, D. J. *Am. Chem. Soc.* **2010**, *132*, 10609-10614.

(16) Dopieralski, P.; Anjukandi, P.; Rückert, M.; Shiga, M.; Ribas-Arino, J.; Mark, D. *J. Mater. Chem.* **2011**, *21*, 8309-8316.

(17) Klukovich, H. M.; Kean, Z. S.; Ramirez, A. L. B.; Lenhardt, J. M.; Lin, J.; Hu, X.; Craig, S. L. *J. Am. Chem. Soc*. **2012**, *134*, 9577-9580.

(18) Akyüz, A.; Catalgil-Giz, H.; Giz, A. *Macromol. Chem. Phys.*, **2008**, *209*, 801-809.

(19) Akyüz, A.; Catalgil-Giz, H.; Giz, A. *Macromol. Chem. Phys.*, **2009**, *210*, 1331-1338.

(20) Potisek, S. L.; Davis, D. A.; Sottos, N. R.; White, S. R.; Moore, J. S. *J. Am. Chem. Soc*. **2007**, *129*, 13808-13809.

(21) Davis, D. A.; Hamilton, A.; Yang, J. L.; Cremar, L. D.; Van Gough, D.; Potisek, S. L.; Ong, M. T.; Braun, P. V.; Martinez, T. J.; White, S. R.; Moore, J. S.; Sottos, N. R. *Nature* **2009**, *459*, 68−72.

(22) Lee, C. K.; Davis, D. A.; White, S. R.; Moore, J. S.; Sottos, N. R.; Braun, P. V. *J. Am. Chem. Soc*. **2010**, *132*, 16107-16111.

(23) O'Bryan, G.; Wong, B. M.; McElhanon, J. R. *ACS Appl. Mater. Interfaces* **2010**, *2*, 1594−1600.

(24) Beiermann, B. A.; Davis, D. A.; Kramer, S. L. B.; Moore, J. S.; Sottos, N. R.; White, S. R. *J. Mater. Chem. 2011*, **21**, 8443−8447.

(25) Kingsbury, C. M.; May, P. A.; Davis, D. A.; White, S. R.; Moore, J. S.; Sottos, N. R. *J. Mater. Chem.* **2011**, *21*, 8381−8388.

(26) Beiermann, B. A.; Kramer, S. L. B.; Moore, J. S.; White, S. R.; Sottos, N. R. *ACS Macro. Lett.* **2012**, *1*, 163-166.

(27) Minkin, V. L. *Chem. Rev*. **2004**, *104*, 2751-2776.

(28) Rosen, B. M.; Percec, V. *Chem. Rev*. **2009**, *109*, 5069-5119.

(29) Ren, W.; Jiang, L.; Wang, W.; Dan, Y. *J. Polym. Sci. Part A: Polym. Chem.* **2010**, *46*, 2793-2797.

(30) Zar, J. H. Comparing Simple Linear Regression Equations. Biostatistical Analysis, 5th ed.; Pearson Prentice Hall: Upper Saddle River, NJ, 2010; p 363.

(31) Basedow, A. M.; Ebert, K. H. *Adv. Polym. Sci.*, **1977**, 22, 83-148.

(32) Price, G. J.; Smith, P. F. *Polymer*, **1993**, *34*, 4111-4117.

(33) Berkowski, K. Ph.D. dissertation. University of Illinois at Urbana-Champaign, **2004**.

(34) Wohl, C. J.; Kuciauskas, D. *J. Phys. Chem. B* **2005**, *109*, 21893-21899.

(35) Davis, D. Ph.D. dissertation. University of Illinois at Urbana-Champaign, **2010**.

(36) Potisek, S. Ph.D. dissertation. University of Illinois at Urbana-Champaign, **2008.**

Chapter 4 – Force Transduction in Branched Polymers

4.1 Introduction

The spiropyran mechanophore has become a ubiquitous tool to learn the fundamental mechanisms of polymer mechanochemistry in both solution and solid-state studies. One of the main goals of polymer mechanochemistry investigations is to understand how to efficiently transmit force to a mechanophore to initiate mechanochemical responses. The properties of molecular mass and chain length for force transduction in various linear acrylic polymers were studied in the previous chapter and identified chain length as the dominant factor in force transduction. In this chapter branched polymer architectures are investigated. To this end we aimed to answer a fundamental question: Can we transmit force more efficiently to a mechanophore using branched architectures?

Recent studies suggest branched architectures are less sensitive to mechanical force under elongational flow in solution. Striegel compared the cleavage profiles, by GPC, of 2-arm, 3-arm, and 8-arm polystyrene in DMAc/LiCl subjected to ultrasonication in an ultrasonic bath.[1] However, the polymers contained different core structures. 2-arm polystyrene contained no linking core, 3-arm polystyrene contained a trimethylbenzene core, and 8-arm polystyrene contained a trimethylsilane core. Additionally, only 2 samples of each type of polymer were studied. Results showed that these specific branched polymers cleaved slower than linear polymers and the cleavage profiles suggested predominant cleavage of the arms of branched polymers rather than the core, or middle, of the polymers. Xue et al. compared 6-arm star PMMA containing different cores in an opposed cross slot apparatus.[2] The cores studied were a rigid triphenylene core and a flexible ethylene core. The hypothesis was that the flexible ethylene core would be more susceptible to cleavage than the rigid triphenylene core. However, the cleavage profile of both types of polymers suggested cleavage of the arms and not the core. Furthermore, the polymers were connected to the cores via an ester linkage. The ester linkage may have been intrinsically more susceptible to cleavage than either of the core structures.

A more systematic approach was adopted here to introduce a proven mechanophore, a spiropyran, at the core of various linear and branched polymers and investigate the activation of the mechanophore itself rather than the distribution of polymer molecular weights. Using previously described sonication flow cell apparatus, solution-based experiments were efficiently conducted to compare the mechanochemical response of branched polymers to linear polymers. Solid-state tensile experiments were conducted using an advanced spectroscopic technique particularly suited for spiropyran-linked polymers. Fluorescence data was collected *in-situ* during tensile tests while simultaneously collected stress and strain responses from the samples. Together, these two analytical techniques were used to understand the

role of branching in force transduction to spiropyran mechanophores in solution and in the solid state, expanding our knowledge of methods to efficiently activate mechanophores.

4.2 Polymerization Initiators

4.2.1 Small Molecule Initiators

To create a systematic series of polymers to compare, appropriately functionalized spiropyrans were synthesized. Bis-functionalized initiator (**1**) was synthesized according published procedures.[3,4] Tetra-and octa-functionalized initiators (**3** and **12**, respectively) were synthesized as outlined in Chapter 2. Original synthetic targets included "clicking" the dendrons to the core spiropyran via azide-alkyne cycloaddition. However, Bielawski et al. reported on the surprising mechanical instability of triazoles.[5,6] Therefore, it became clear that an important criterion to compare linear and branched structures was the chemically equivalent connectivity of polymers to the mechanophores. Branched polyesters were chosen as the branching motif to match the ester connection of the previously developed 2-arm PMA polymers. Additionally, the connecting dendrons contain only C-C bonds which are the same bonds connecting the polymer backbone. The structures of the initiators are given in Figure 4.1.

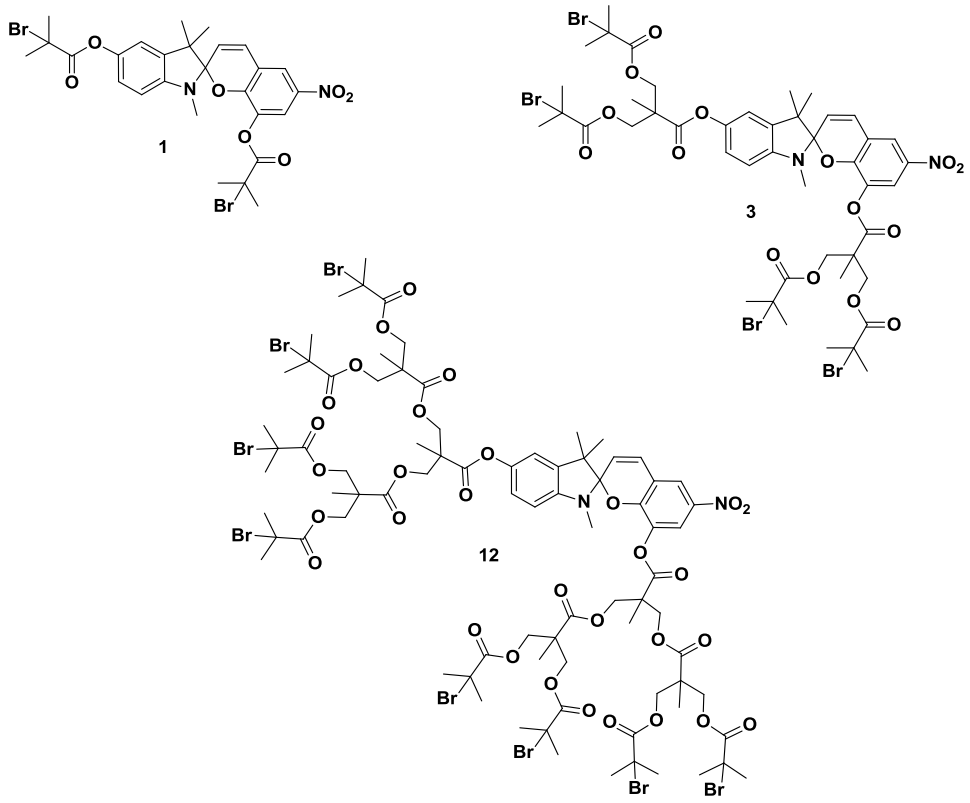

Figure 4.1. Structure of Initiators used for SET-LRP.

4.2.2 UV-Vis Characterization

The UV-Vis absorption spectra of the initiators are important pieces of data to understand any potential electronic differences between the compounds that could manifest itself in polymer testing. The UV-Vis for each compound was measured in the open and closed states in acetonitrile, the solvent used for sonication studies. All compounds respond to UV light and convert to their merocyanine form in a predictable manner. λ_{max} for each compound was 554 nm as shown in Figure 4.2 a-c.

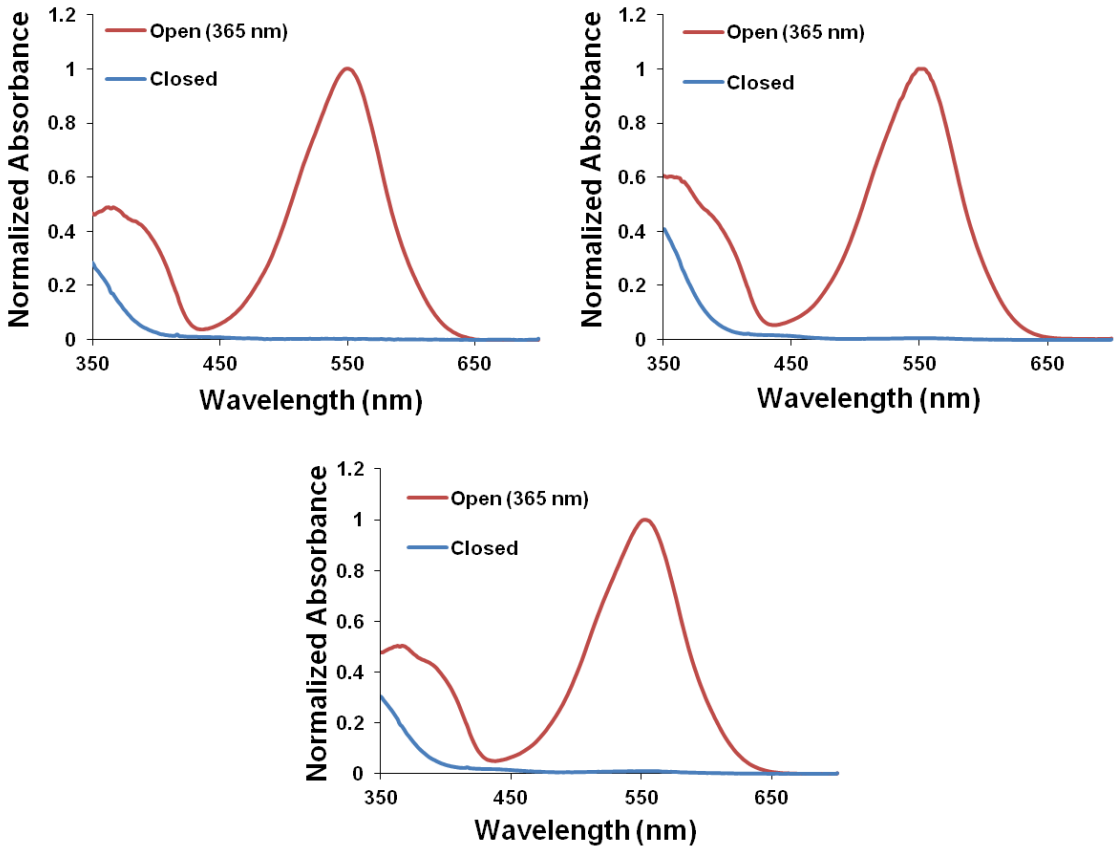

Figure 4.2. UV-Vis spectra of initiators in the closed and open states: a) compound **1**; b) compound **3**; c) compound **12**.

4.3 Polymer Synthesis

4.3.1 Polymers

Each type of polymer architecture was synthesized by polymerizing the respective intiators (**1**, **3** and **12**) with methyl acrylate under SET-LRP conditions. PMA was targeted as the polymer of choice because it has proved to be a useful polymer for mechanophore incorporation and sonication studies[3,7] and it has adequate optical properties for solid state testing.[8] A range of molecular weights was targeted for each polymer series. 2-arm polymers were controlled by the initiator to monomer ratio. Sonication of copper powder before introducing it to the reaction vessel and addition of small amounts of $CuBr_2$ gave consistently good results, as evidenced by monomodal GPC traces with narrow PDI, and these techniques were used for all polymerizations. However, synthetic challenges arose with the synthesis of 4-arm and 8-arm polymers. Upon complete consumption of monomer a significant high molecular weight shoulder could be observed by GPC. This high MW shoulder was attributed to star-star coupling[9,10] and was mitigated by quenching the polymerization before complete consumption of monomer. For 4-arm polymers, a 2 hour rxn time was shortened to 1.5 hrs. Target MW could be achieved by adding a slight excess of monomer to account for the star-star coupling towards the end of the reaction. For 8 arm polymers, MW was controlled strictly by time[11] as star-star coupling was an even more significant issue. Additionally, the 8-arm series was susceptible to various types of degradation. For example, after long-term storage (> 6 months) the 8-arm polymers no longer displayed photochromic or mechanochromic properties indicating degradation of the spiropyran. Interestingly, the GPC traces showed no evidence of a change in molecular weight. Furthermore, several 8-arm polymers displayed a significant growth of a high molecular weight shoulder over a matter of

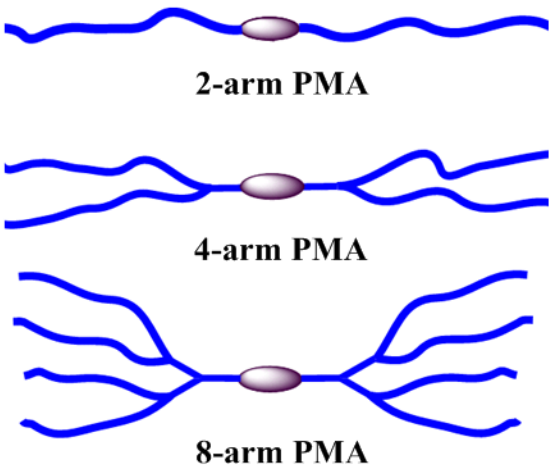

Figure 4.3. Mechanophore-linked poly(methyl acrylate) architectures investigated.

weeks potentially indicating star-star coupling. Fortunately, these challenges were overcome by filtering the polymers through both basic alumina and silica to remove as much copper as possible, precipitating from THF into MeOH twice to remove as much DMSO as possible, and drying at 50 °C overnight to remove as much solvent as possible. Interestingly, only the 8-arm polymers had these problems, although all polymers were subsequently treated in this manner to ensure no future problems and for consistency.

4.3.2 Characterization

Polymers were characterized by GPC with equipped refractive index (RI), UV-Vis, light scattering, and viscometry detectors to obtain a range of information. Figure 4.4 shows the GPC traces of polymers in each series. 4-arm and 8-arm polymers display much sharper peaks compared to the 2-arm polymers which is indicative of their structure. Additionally, several samples in both the 4-arm and 8-arm have a very slight high molecular weight shoulder which was previously attributed to star-star coupling. Table 4.1 give numerical data acquired for each polymer series including weight average molecular weight, M_w, polydispersity index, PDI, radius of gyration, R_g radius of hydration, R_h, shape factor, R_g/R_h, and intrinsic viscosity, [η]. It can be seen that intrinsic viscosity and size, both R_h and R_g, are lowest for the 8-arm polymers. Additionally these measurements are lower for the 4-arm polymers than the 2-arm polymers. The shape factor, ρ (R_g/R_h), gives an indication of conformation with values of 0.77 being associated with hard spheres, values of 1.5 associated with extended chains, and even higher values associated with rigid rods. The values obtained here, show the linear polymers between 1.3-1.2, 4 arm polymers with values of 1.17-1.14, and 8-arm polymers with values of 1.05-1.04. These data indicate that linear polymers are in a more extended coil conformation while the 4-arm and 8-arm polymers are more compact. Together, these data give a good indication of the more compact structure of the branched polymers in relation to the linear polymers.

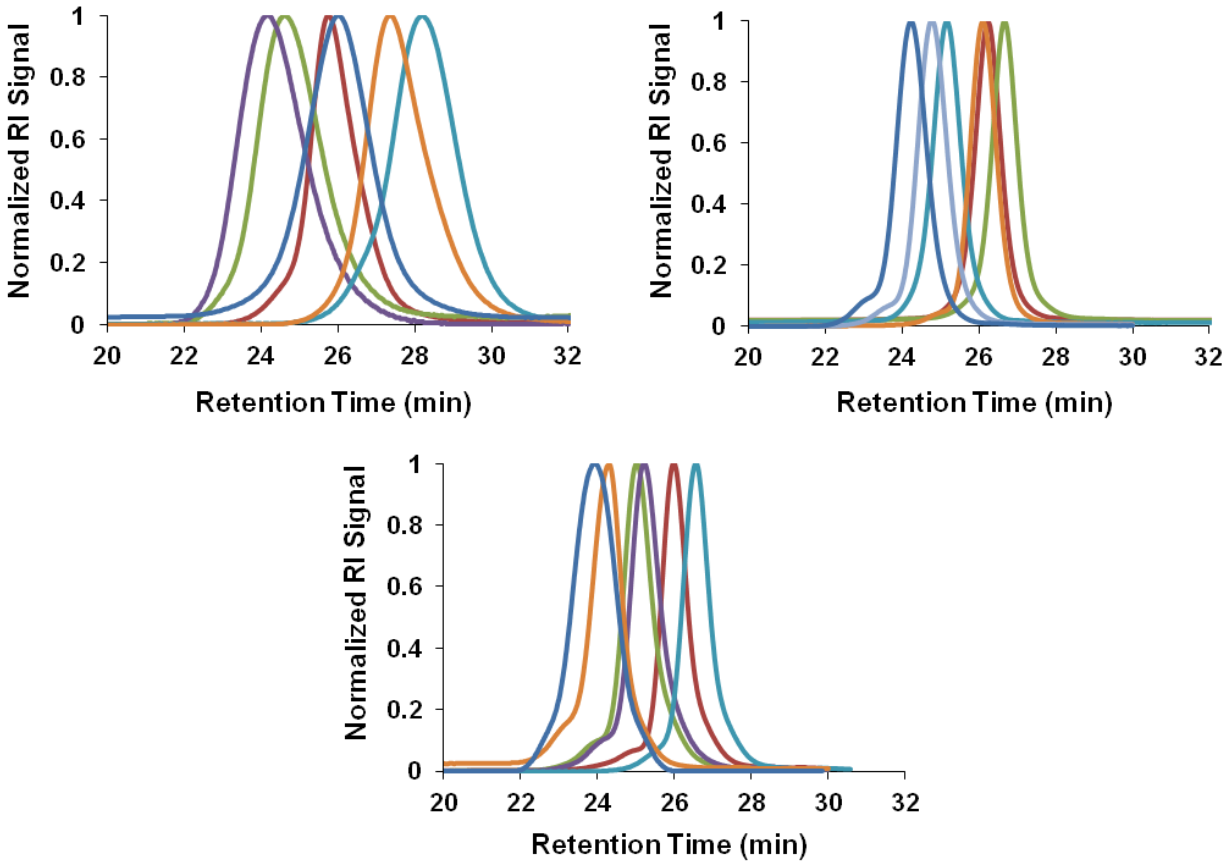

Figure 4.4. GPC traces of spiropyran-linked PMA: a) 2-arm PMA; b) 4-arm PMA; c) and 8-arm PMA.

Table 4.1. GPC-MALS characterization of a) 2-arm PMA, b) 4-arm PMA and c) 8-arm PMA.

a)

M_w (kDa)	PDI	R_g (nm)	R_h (nm)	R_g/R_h	[η] (mL/g)
518	1.04	26.2	20.2	1.29703	98.64
419	1.02	22.5	17.5	1.285714	80.89
240	1.09	15.9	12.6	1.261905	52.34
243	1.08	15.7	12.4	1.266129	50.2
132	1.01	11.4	9.1	1.252747	30.48
124	1.02	10.0	8.3	1.204819	24.22

b)

M_w (kDa)	PDI	R_g (nm)	R_h (nm)	R_g/R_h	[η] (mL/g)
523	1.067	20.5	17.5	1.171429	78
396	1.1	17.3	14.9	1.161074	56.7
264	1.038	13.7	12	1.141667	42
211	1.06	-	10.3	-	32
191	1.045	-	9.3	-	29.5
157	1.038	-	8.3	-	25.7

c)

M_w (kDa)	PDI	R_g (nm)	R_h (nm)	R_g/R_h	[η] (mL/g)
658	1.16	20.4	19.4	1.051546	65
555	1.15	17.8	17	1.047059	55
450	1.09	14.6	14.1	1.035461	41
410	1.107	14	13.5	1.037037	39.5
284	1.06	-	10.9	-	29.9
201	1.17	-	9.1	-	24.4

4.4 Solution-Based Characterization

4.4.1 UV-Vis Characterization

Each series of polymers was tested for photochromic and mechanochromic properties. First UV-Vis spectra for the open and closed states was measured. Each type of polymer displayed photochromic behavior typical of spiropyran compounds. λ_{max} for each type of polymer in acetonitrile was 554 nm.

These measurements show that there is no change in λ_{max} due to attaching various number of polymer chains.

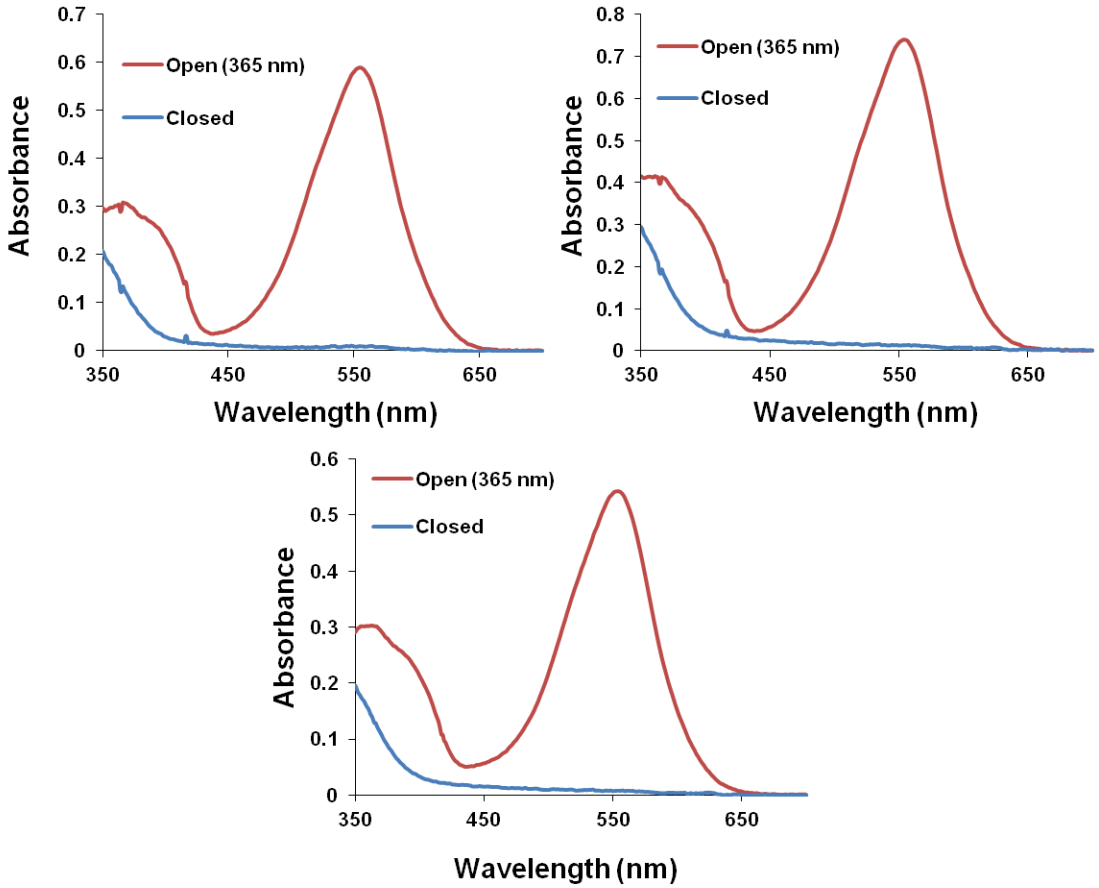

Figure 4.5. Representative UV-Vis spectra of polymers in their closed and open states: a) 2-arm PMA; b) 4-arm PMA; c) and 8-arm PMA.

4.4.2 Thermal Reversion

Additionally reversion of each type of architecture was measured. The thermal reversion rate gives information on the rate of ring-closure from the merocyanine to the spiropyran form. Even small changes in the reversion rate can have drastic consequences in measuring the forward ring-opening process under mechanical stimuli, as both forward and reverse reactions are always occurring. Davis synthesized a series of spiropyran derivatives and found drastically different thermal reversion rates, precluding them from being tested mechanically in a reasonable manner.[12] Here, each compound was dissolved in acetonitrile and irradiated with UV light and the absorption at λ_{max} was measured over time until the molecules reached the predominant spiropyran form. Figure 4.6 shows that the rate of thermal reversion for the compounds is very similar which proved promising for testing their mechanochemical differences. Measured rate constants for thermal reversion for each type of architecture were 8.2 x 10^{-3} min^{-1}, 8.7 x 10^{-3} min^{-1}, and 8.6 x 10^{-3} min^{-1}. These experimental results suggest no intrinsic electronic differences between each type of architecture due to their varying structures.

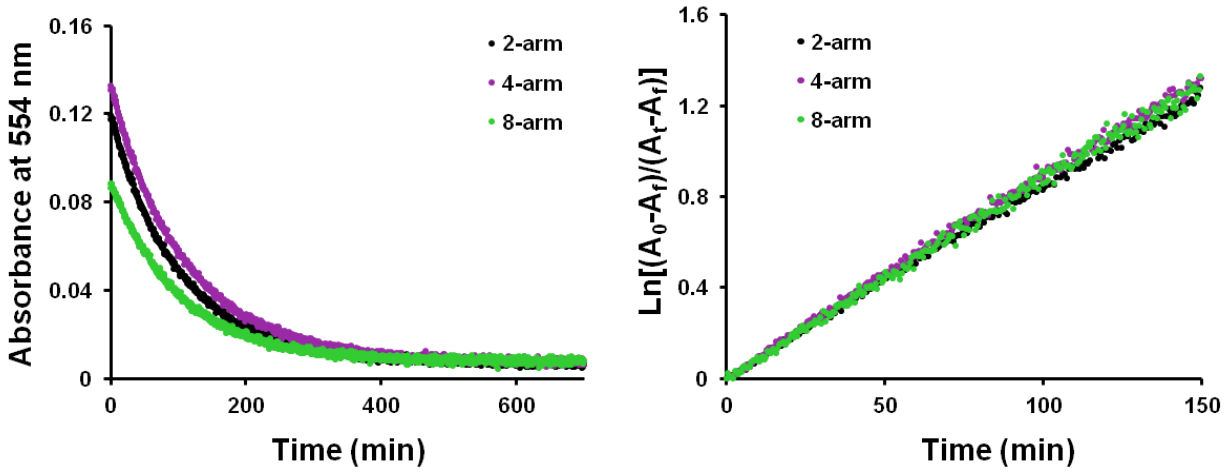

Figure 4.6. Thermal reversion measurements of polymers in the flow cell at 3-5 degrees.

4.4.3 Mechanochemical Characterization

Next the mechanochromic capabilities of these polymers of these polymers were tested. Each type of polymer was subjected to ultrasonication in a flow cell described in Chapter 3 while obtaining UV-Vis absorbance throughout the experiments. Each type of polymer architecture displayed a gradual increase in the merocyanine peak over time. However, the maximum intensity was reached for 2-arm polymers much faster than other architectures. Figure 4.7 shows the rise in 554 nm as a function of sonication time. Clearly, time to maximum intensity increases as the number of arms increases.

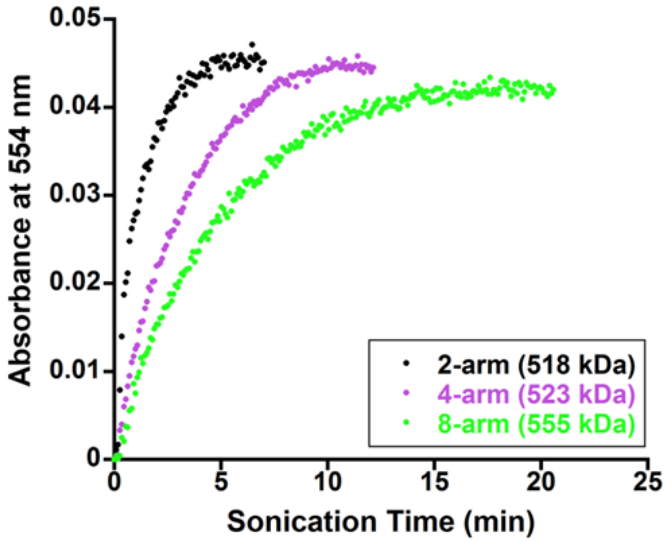

Figure 4.7. Plot of UV-Vis absorbance against sonication time of varying architectures showing trend of increasing time to maximum absorbance with increasing number of arms.

4.4.4 Rate Activation Kinetics

Rate constants for mechanochemical ring-opening were obtained for each polymer in each series. Rate constants were calculated in the same way as presented in Ch. 3. Figure 4.8 shows the rate constant as a function of weight average molecular weight. All polymer architectures exhibited an increase in rate constant with increasing molecular weight. Slopes of the linear regression lines decrease with increasing number of arms by a factor of 2. Additionally, Figure 4.9 shows the rate constant against average chain weight. The average chain weight was calculated by dividing the total molecular weight by the number of arms. These data show that the threshold mass of an individual arm is lower for branched polymers. However, Figure 4.10 shows the rate constant against the size of the polymers (radius of hydration). These data show that the threshold size of the branched polymers is still larger than that of the 2-arm polymers even if the chains are shorter in length. Together, these data suggest that chain length is the dominant factor but not the only factor that governs the mechanochemical reactivity in solution. It is unclear exactly what the secondary factor is, but it is probably related to size. Furthermore, Figure 4.11 shows the relationship of intrinsic viscosity and rate constant between the polymers. This plot shows a similar trend in slope, but the threshold value (x-intercept) is the most similar between the architectures of all the properties examined.

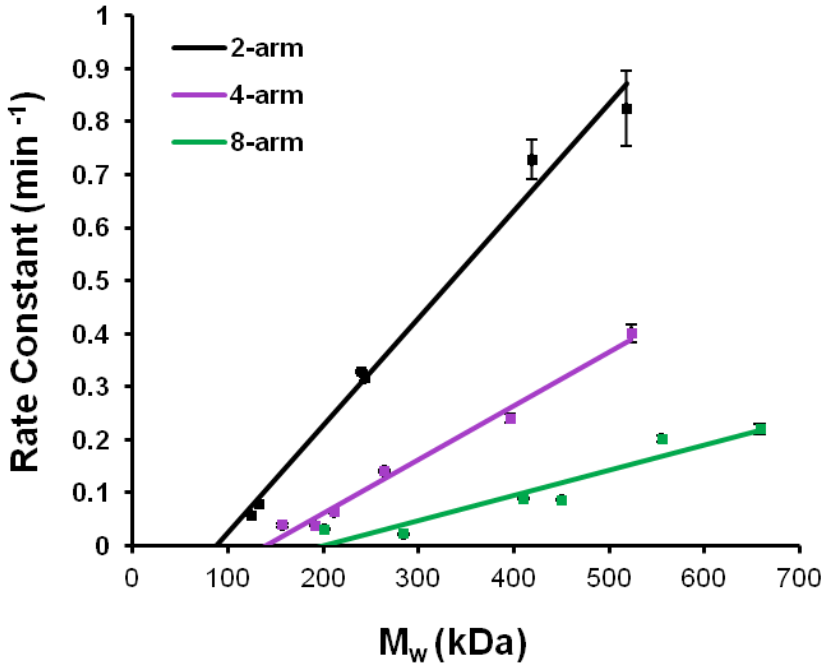

Figure 4.8. Comparison of the molecular weight (M_w) dependence on mechanochemical activation of varying architectures. Rate constants plotted (data points) are averages of two sonication experiments. Error bars represent the maximum and minimum rate constants obtained experimentally.

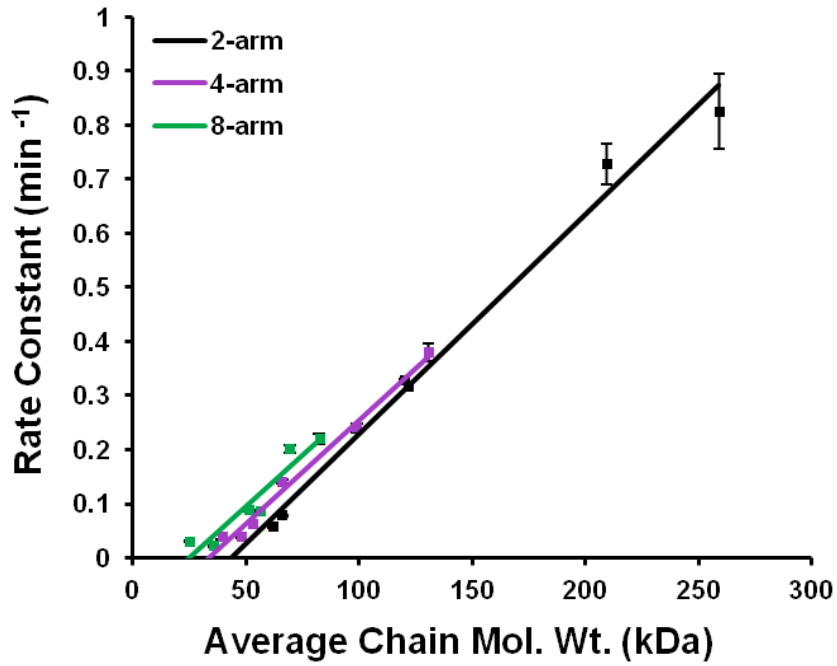

Figure 4.9. Comparison of the average arm molecular weight (M_w) dependence on mechanochemical activation of varying architectures. Rate constants plotted (data points) are averages of two sonication experiments. Error bars represent the maximum and minimum rate constants obtained experimentally.

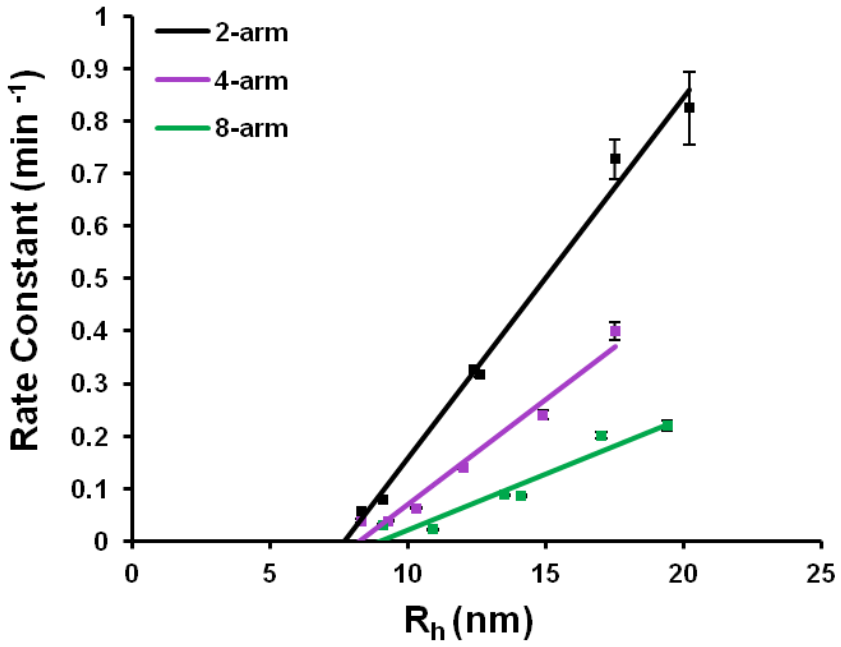

Figure 4.10. Comparison of the size dependence (R_h) on mechanochemical activation of varying architectures. Rate constants plotted (data points) are averages of two sonication experiments. Error bars represent the maximum and minimum rate constants obtained experimentally.

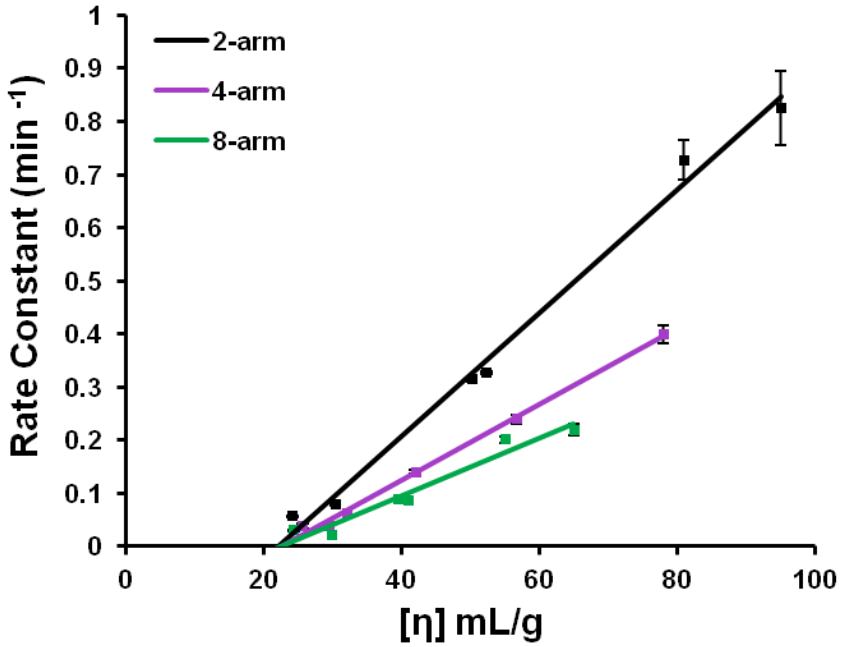

Figure 4.11. Comparison of rate constant against intrinsic viscosity, [η], of varying architectures. Rate constants plotted (data points) are averages of two sonication experiments. Error bars represent the maximum and minimum rate constants obtained experimentally.

4.5 Solid-State Tests

4.5.1 Tensile Tests

Next we set out to investigate the reactivity of branched architectures in the solid state. As has previously been shown by Beierrman et al., the glass transition temperature, T_g, can play a significant role in the mechanochemical reactivity of mechanophore linked polymers.[13] Specifically, spiropyran linked PMMA was found to be unreactive toward force stimuli when pulled in tension at room temperature. Lowering the T_g by plasticizing with solvent was found to be important to observing mechanochromic behavior of these polymers. Accordingly, the T_g the 2-arm, 4-arm, and 8-arm PMA polymers in this work were measured by DSC to investigate any differences. No significant differences in T_g were observed. It is important to note that adequate drying of the polymers (at 50 °C under high vacuum for 24 hrs) was needed to achieve consistent results. While small amounts of solvent trapped in the polymer may not have any effect on solution-based mechanochemistry experiments due to the high dilution, that effect could be significant in solid state experiments, effectively softening the samples.

Polymers were tested in the solid state by molding into dog-bone specimens adequate for the experimental apparatus.[4] A unique experimental setup was created by Beiermann et al. to pull the specimens in tension at a desired strain rate while simultaneously collecting fluorescence from the samples.[8] A graphical representation of the experimental is provided in Figure 4.12.

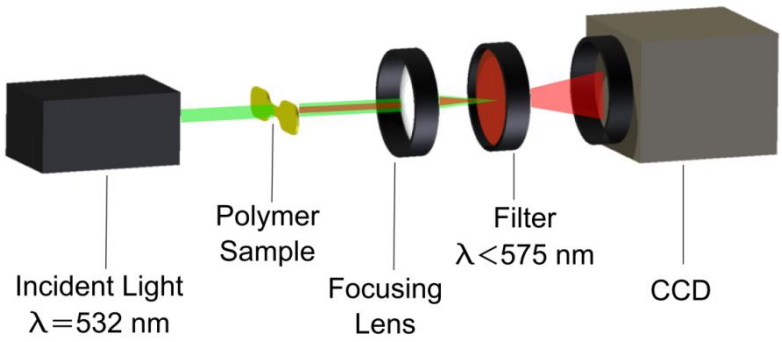

Figure 4.12. Representation of the experimental setup for tensile experiments.

Three strain rates ($d\lambda/dt$) were chosen to test as strain rate has shown to be a significant factor in mechanochemical activation.[8] Figure 4.13a shows the fluorescence as a function of stretch ratio for each type of polymer at the fastest strain rate. Stretch ratio is defined as the current length of the sample divided by the initial length. Here no significant difference in activation was observed between different

architectures, in stark contrast to solution based experiments. As the strain rate was decreased (Figure 4.13b and 4.13c) a significant difference was observed for the different architectures. An increase in fluorescence was observed at lower stretch ratios for branched polymers than linear polymers. Additionally, higher levels of fluorescence were attained for branched polymers in general. The solid state measurements are summarized in Figure 4.14 and show that activation of 2-arm polymers is significantly affected by strain rate while branched polymers are relatively unaffected by strain rate. The mechanical behaviors of the different architectures were similar and no trend was observed. Additionally, there was no observed correlation between molecular weight and activation (above 100 kDa).

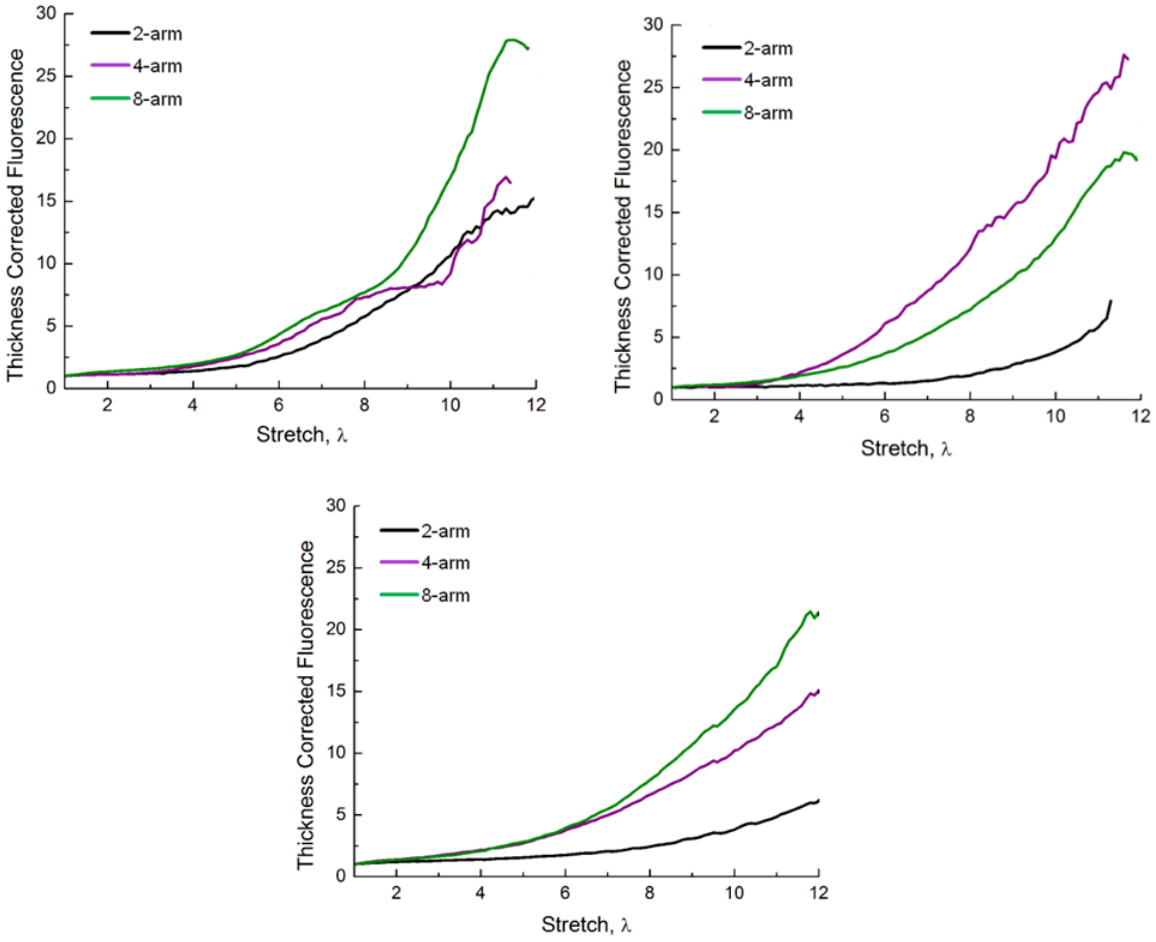

Figure 4.13. Representative normalized fluorescence curves for linear, 4-arm and 8-arm SP-linked PMA tested in tension at deformation rates ($d\lambda/dt$) of a) 0.004 s^{-1}, b) 0.02 s^{-1} and c) 0.10 s^{-1}.

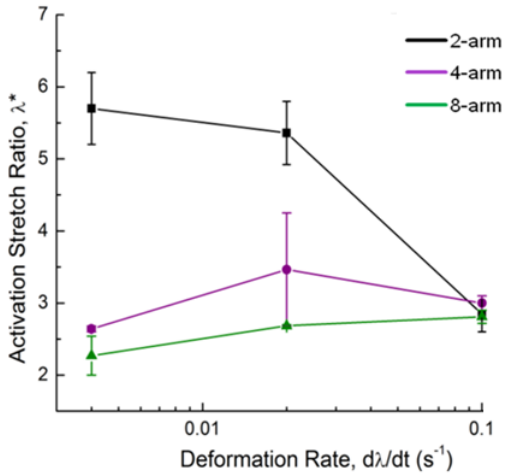

Figure 4.14 Stretch ratio at the activation point, λ*, for each architecture plotted as a function of deformation rate. The data shows a deformation rate dependence of the 2-arm polymers while 4-arm and 8-arm polymers are relatively unaffected by deformation rate.

4.6 Conclusions

4-arm and 8-arm star PMA containing a single spiropyran at their core were successfully synthesized by SET-LRP. Polymer molecular weight, size, and intrinsic viscosity were characterized with GPC-MALS. All polymers studied displayed photochromic and mechanochromic properties in solution and solid-state. Solution based experiments utilizing an ultrasonication flow cell showed that branched polymers are less efficient than linear polymers in force transduction for activating mechanophores at the core. The various polymer architectures were tested in solid-state tensile stretching experiments where fluorescence of the activated mechanophores was monitored as a function of strain. The results indicate that activation in 2-arm polymers is largely affected by strain rate while activation in branched polymers is not significantly affected by strain rate. As the strain rate is decreased branched polymers exhibit activation at much lower strains than linear polymers. These results suggest that it is possible to adjust the time scale of mechanophore response in both solution and solid-state applications by adapting the architecture of the polymer.

The data provided in this chapter combined with the evidence provided in Chapter 3 point to the conclusion that chain length is the property that most affects mechanophore activation under ultrasound conditions. Attempts to over-engineering a polymer's structure and topology could prove ineffective if activation under ultrasound is the main objective. However, in solid-state applications, where the chain entanglement threshold has been crossed, there exists a great opportunity to explore various structural parameters of the polymers and optimize the polymer's ability to transmit force to the mechanophore. Retarding chain slippage events that lead to relaxation appears to be a useful approach to maximizing

mechanophore response in the solid state. Finally, perhaps there exists a general architectural motif or mechanistic approach for these types of polymers that would eliminate the need for plastic deformation before mechanophore activation or allow mechanophore activation for brittle polymers.

4.7 Detailed Procedures

Unless otherwise stated, all starting materials were obtained from commercial suppliers and used without purification. Anhydrous acetonitrile was obtained from Acros (Acroseal, 99.9%). Cu(0) powder (99%, 1-5 μm) and Me_6TREN were purchased from Sigma-Aldrich. Silica gel 60 (230-400 mesh) was purchased from Silicycle. Acrylate monomers were filtered through basic alumina to remove the inhibitors prior to use and kept under an argon atmosphere. Cu(0) powder was sonicated in DMSO in a Fisher Scientific Tabletop Ultrasonic Cleaner, model FS-20D (3/4 gal tank), 40kHz, with a max input power of 80W. All synthetic reactions and sonication experiments were performed under argon atmosphere.

Analytical gel permeation chromatograph (GPC) analyses were performed with a Waters 1515 Isocratic HPLC pump, a Waters (2998) Photodiode Array Detector, a Waters (2414) Refractive Index Detector, a Wyatt miniDAWN Treos light scattering detector, a Wyatt ViscoStar viscometer, Waters (2707) 96-well autosampler, and a series of 4 Waters HR Styragel columns (7.8 X 300mm, HR1, HR3, HR4, and HR5) in THF at 30 °C. DnDc was acquired using Astra software 100% mass recovery methods and averaged over several samples. A value of 0.055 was used for all analyses.

UV-Vis spectra were recorded using a Shimadzu UV-2401PC. Standard quartz cells and standard quartz flow cell cuvettes with a path length of 10 cm used were purchased from Starna Cells. UV irradiation of samples dissolved in acetonitrile or MEK was performed with a Model UVG-11 Mineralight lamp (short wave UV – 254 nm or long wave UV-365 nm).

Ultrasound experiments were performed on a Vibra Cell 505 liquid processor with a ½" diameter solid probe from Sonics and Materials. The distance between the titanium tip and bottom of the Suslick cell was 1 cm. The Suslick cells were made by the School of Chemical Sciences' Glass Shop at the University of Illinois. PTFE tubing was used to circulate the solvent. A peristaltic pump from equipped with a Masterflex L/S PTFE-tubing pump head was purchased from Cole-Parmer. A Neslab CC 100 immersion cooler equipped with a Neslab cryotrol temperature controller was purchased from Thermoscientific.

4.7.1 Detailed Synthetic Procedures

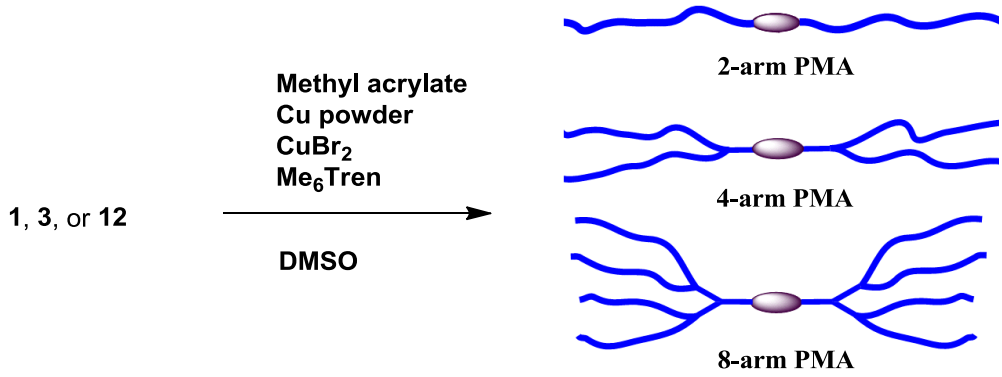

Scheme 4.1. General reaction components of SET-LRP to produce linear and star PMA.

Table 4.2. Conditions used for SET-LRP

Polymer Type	Initiator (eq)	Cu(0) (eq)	$CuBr_2$ (eq)	Me_6Tren (eq)	DMSO (vol)	Monomer (vol)
2-arm PMA	1.0	2.0	0.05	2.1	0.5 mL	1.0 mL
4-arm PMA	1.0	2.0	0.1	2.1	0.25 mL	1.0 mL (slight excess)
8-arm PMA	1.0	2.0	0.5	2.6	0.25 mL	1.0 mL (excess)

4.7.2. General Procedure for Polymer Synthesis

Cu(0) (2.44 mg) was weighed on analytical balance and then added to a 20 mL scintillation vial. DMSO (0.5 ml) was added to the vial and the mixture was sonicated in a sonicator bath for c.a. 1 min. An aliquot of 0.25 mL (containing 1.22 mg Cu(0), 0.0192 mmol, 2 equiv) was removed and added to a 10 mL Schlenk flask equipped with a teflon stir bar. $CuBr_2$ (1.72 mg) was added to 2 mL of DMSO and allowed to dissolve. An aliquot of 0.25 mL was removed (containing 0.215 mg $CuBr_2$, 0.000961 mmol, 0.1 equiv) and added to the Schlenk flask. Me_6TREN (5.40 μL, 0.0202 mmol, 2.1 equiv) was measured with a microliter syringe and transferred to the Schlenk flask. Monomer (1.00 mL, 11.1 mmol, 1154 equiv) was added. Lastly, the initiator (6.27 mg, 0.00961 mmol, 1 equiv) was added to the flask. The flask was immediately sealed with a ground glass stopper, secured with copper wire, and three freeze-pump-thaw cycles were applied to remove dissolved oxygen. The flask was backfilled with argon and was allowed to stir in a water bath for 2 h at room temperature. The polymerization was opened to air, 10 mL of THF were added, and the polymer filtered through a pad of basic alumina and silica. After solvent was removed *in vacuo*, a highly concentrated mixture of polymer in THF was precipitated by dropwise

addition to stirring cold methanol. The resulting polymer was collected and dried under high vacuum at 50 °C.

A typical polymerization for 8-arm polymers contained the following amounts: 4.45 mg initiator (**12**) (0.002 mmol, 1 equiv), 0.254 mg Cu powder (0.004 mmol, 2 equiv), 0.220 mg $CuBr_2$ (0.00100 mmol, 0.5 equiv), 0.600 μL Me_6Tren (0.00520 mmol, 2.6 equiv), 0.25 mL DMSO, and 1 mL of methyl acrylate (excess).

Table 4.3. Reaction times for 8-arm PMA syntheses

Reaction Time (min)	M_w (kDa)
25	201
35	284
50	410
60	450
75	555
90	658

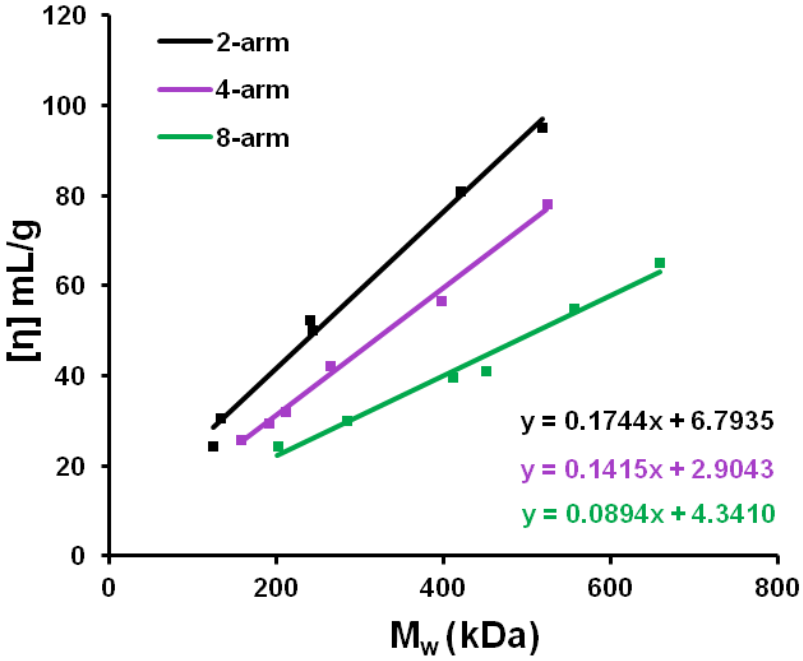

Figure 4.15. Intrinsic viscosity as a function of molecular weight (M_w) for all polymers.

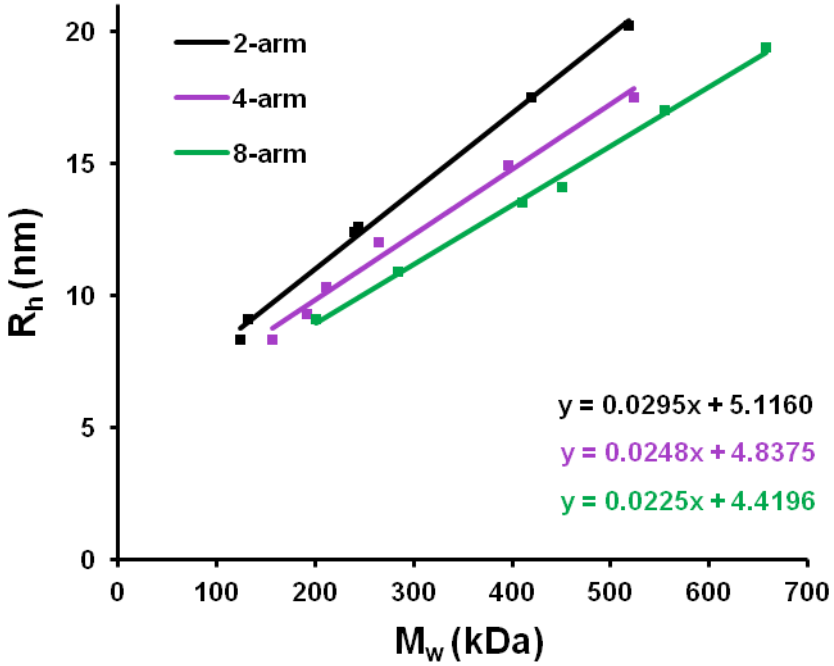

Figure 4.16. Hydrodynamic radius (R_h) as a function of molecular weight (M_w) for all polymers.

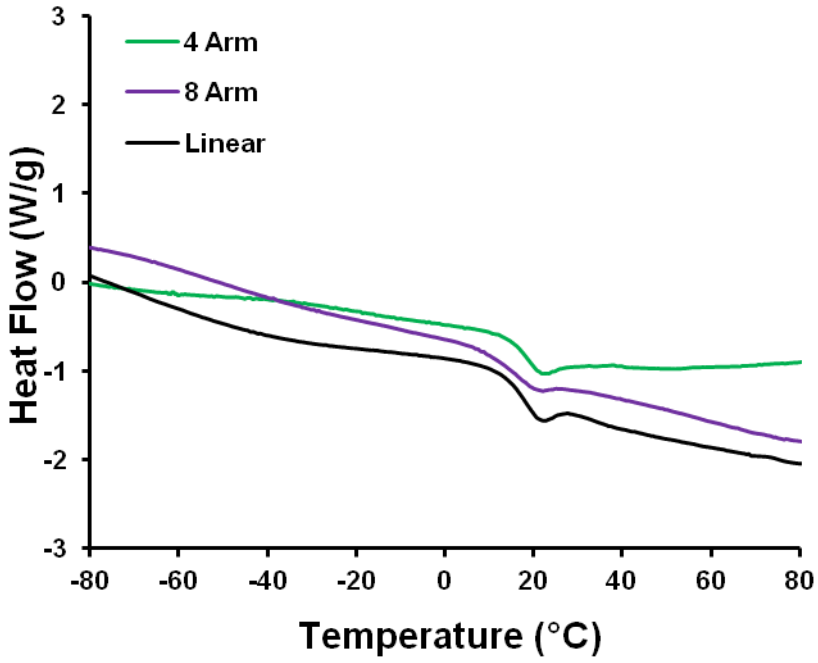

Figure 4.17. Representative DSC traces of linear and star PMA showing glass transitions. Each type of polymer displayed a T_g of 12-13 °C.

4.7.3 General Procedure for Sonication Experiments

The sonication apparatus was assembled as shown in Figures 3.32-3.34 of Chapter 3. Polymer dissolved at a concentration of 1 mg/ml in acetonitrile was transferred to an oven-dried Suslick cell, which was placed into the collar and screwed onto the probe. An argon line, an inlet (to return solvent to the Suslick cell) and an outlet (to draw solvent from the Suslick cell) tube were each placed into the three arms of the Suslick cell, respectively. Argon was sparged through the system for 30 min prior to any sonication runs, as well as during the run itself. Following this, the Suslick cell was lowered into the acetone bath for 5 min prior to sonication. Longer cooling times resulted in the solution being so cold that water would condense on the cuvette. After 5 min of cooling, the UV-Vis was started followed immediately by starting sonication. The whole system was kept in the dark during the entire experiment.

Table 4.4. Temperatures of acetone bath for sonication experiments.

Instrument Amplitude (%)	Power Intensity (W cm^{-2})	Acetone Bath Temperature (°C)	Temperature of Solvent in Suslick Cell (°C)
35%	10.7	-18 °C	3-5 °C

4.7.4. Kinetic analysis

Kinetic analysis was conducted in the same manner as discussed in section 3.5.7 of Chapter 3.

Table 4.5. Measured rate constants of 2-arm PMA in acetonitrile at 3-5 °C, 1 mg/ml. Each value is an average of two sonication experiments.

M_w (kDa)	Rate Constant (min^{-1})
518	0.825
419	0.7279
243	0.316
240	0.3275
132	0.07845
124	0.0569

Table 4.6. Measured rate constants of 4-arm PMA in acetonitrile at 3-5 °C, 1 mg/ml. Each value is an average of two sonication experiments.

M_w (kDa)	Rate Constant (min^{-1})
523	0.35
396	0.24
264	0.1405
211	0.0625
191	0.03805
157	0.0384

Table 4.7. Measured rate constants of 8-arm PMA in acetonitrile at 3-5 °C, 1 mg/ml. Each value is an average of two sonication experiments.

M_w (kDa)	Rate Constant (min^{-1})
658	0.22
555	0.2015
450	0.08615
410	0.0881
284	0.02165
201	0.03065

Table 4.8. Threshold values (x intercepts) of regression lines in Figures 4.8-4.11.

	Threshold Values			
Polymer Type	**M_w (kDa)**	**R_h (nm)**	**η**	**Average Chain Weight (kDa)**
2-arm	88	7.7	21.9	43.4
4-arm	138	8.2	22.5	33.2
8-arm	197	8.9	22.4	24.9

Table 4.9. Slopes of regression lines in Figures 4.8-4.11.

	Slopes			
Polymer Type	**M_w (kDa)**	**R_h (nm)**	**η**	**Average Chain Weight (kDa)**
2-arm	.0020	0.069	.012	.0041
4-arm	.0010	.039	.0072	.0039
8-arm	.0048	.021	.0054	.0038

4.7.5. Control Experiments

A branched control compound was made by polymerizing **13** under SET-LRP conditions. This control polymer was sonicated at identical conditions to the mechanically active polymers. Figure 4.18 shows the UV-Vis absorbance values collected at various time intervals of a 1 hour sonication experiment followed by post-sonication UV-activation (365 nm for 5 min). The absorbance values obtained during the sonication experiment show very little change and no appreciable merocyanine peak while post-sonication UV-activation resulted in significant change in the spectrum which is attributed to the presence of the merocyanine.

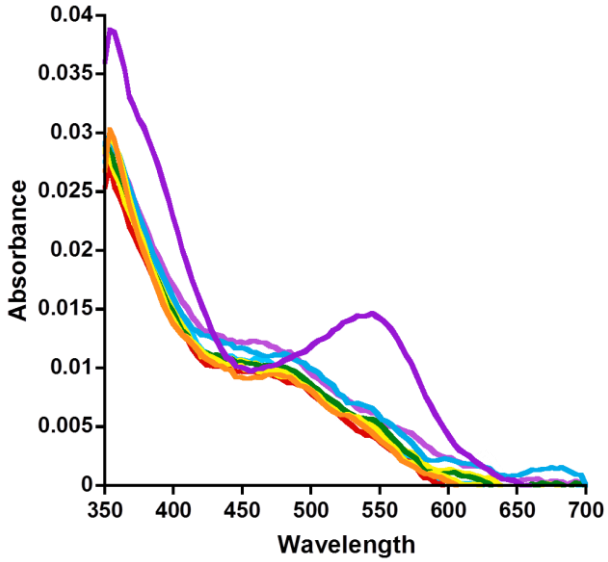

Figure 4.18. UV-Vis absorption spectra of branched control PMA during sonication in acetonitrile at 10.7 W cm^{-2} power intensity. 10 spectra were collected over the course of 1 hour. No significant change is observed. Top purple spectra = absorption spectrum of post-sonication polymer irradiated with 365 nm light for 5 min showing that the spiropyran is UV active.

4.7.6. Solid-state sample geometry

Polymer samples were molded in closed molds with dimensions shown in Figure. 4.19. Two parallel plates heated to the temperature above the polymer T_g applied a pressure to the closed mold. Poly(methyl acrylate) (T_g = 12 °C) was molded at 71 °C (160 °F) for ten minutes at applied pressure of approximately 0.4 MPa (60 psi). Samples were then allowed to cool at room temperature for one hour before removing from the mold.

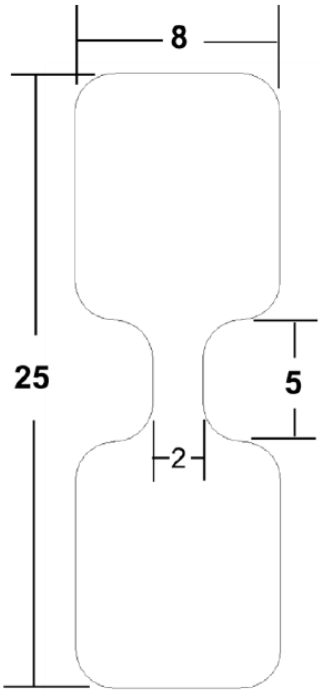

Figure 4.19. Sample dimensions for SP-linked PMA. All dimensions are in mm.

4.7.7 Tensile Testing Protocol[8]

All polymer samples in this study were tested in tension using a custom uniaxial load frame from IMAC Motion Control Corporation. Two opposing screw driven actuators applied an identical displacement to each side of polymer sample such that the center of the sample remained in the field of view for optical studies. Load in the polymer sample was detected using a 5-lb Honeywell Sensotec Load Cell (Model 31) attached to one of the actuators. Displacement of the actuators was controlled through NI LabVIEW. The load frame was oriented horizontally on an optical table. Unless otherwise specified, samples were irradiated with green light (λ = 532 nm) for 10 minutes at RT prior to testing in order to drive the mechanophores predominantly to the SP form. For monotonic tensile testing, the load frame was displacement-controlled and applied stretch rates were 0.10 s^{-1}, 0.02 s^{-1}, or 0.004 s^{-1}. For stress relaxation

testing, samples were loaded at a relatively high deformation rate (0.10 s^{-1}) then held at a constant amount of deformation, and the optical and mechanical response was monitored over time.

4.8 References

(1) Striegel, A. M. *J. Biochem. Biophys. Methods* **2003**, *56*, 117-139.

(2) Xue. L.; Agarwal, U. S.; Lemstra, P. J. *Macromolecules* **2005**, *38*, 8825-8832.

(3) Potisek, S. L.; Davis, D. A.; Sottos, N. R.; White, S. R.; Moore, J. S. *J. Am. Chem. Soc.* **2007**, *129*, 13808.

(4) Davis, D. A.; Hamilton, A.; Yang, J.; Cremar, L. D.; Van Gough, D.; Potisek, S. L.; Ong, M. T.; Braun, P. V.; Martínez, T. J.; White, S. R.; Moore, J. S.; Sottos, N. R. *Nature* **2009**, *459*, 68.

(5) Brantley, J. N.; Wiggins, K. M.; Bielawski, C. W. *Science* **2011**, *333*, 1606-1609.

(6) Brantley, J. N.; Konda, S. S. M.; Makarov, D. E.; Bielawski, C. W. *J. Am. Chem. Soc.* **2012**, *134*, 9882.

(7) Brantley, J. N.; Wiggins, K. M.; Bielawski, C. W. *Polym. Int.* **2013**, *62*, 2-12.

(8) Beiermann, B. Ph.D. dissertation. University of Illinois at Urbana-Champaign, **2013.**

(9) Angot, S.; Murthy, K.S.; Taton, D.; Gnanou, Y. *Macromolecules* **1998**, *31*, 7218-7225.

(10) Radke, W.; Gerber, J.; Wittmann, G. *Polymer* **2003**, *44*, 519-525.

(11) Ghosh, K.; Moore, J. S. *J. Am. Chem. Soc.* **2011**, *133*, 19650-19652.

(12) Davis, D. Ph.D. dissertation. University of Illinois at Urbana-Champaign, **2010.**

(13) Beiermann, B. A.; Davis, D. A.; Kramer, S. L. B.; Moore, J. S.; Sottos, N. R.; White, S. R. *J. Mater. Chem.* **2011**, *21*, 8443.

Chapter 5 – Interfacial Activation of Mechanophores

5.1 Introduction

The various polymers investigated in this thesis have demonstrated how changing the polymer architecture connected to the mechanophore can significantly alter the response of the mechanophore. Up to this point, homogenous polymer systems have been explored. In this chapter, a discussion will ensue of progress towards developing a mechanochemically active composite of heterogenous architecture. The fact that each new mechanophore designed and experimentally demonstrated can have a unique chemical response lends itself to targeting that response for a specific application. A specific engineering application where damage sensing mechanophores could find particular use is within fiber-reinforced composites.[1] Damage induced within these composites is typically delamination of the fiber from the matrix material. Detecting the damage at such a small scale, potentially without the aide of a spectrometer or advanced analytical equipment could prove useful. Here, a system has been designed to introduce a spiropyran, a proven color-generating and fluorescent mechanophore, at the interface of a glass fiber and matrix and investigate potential damage sensing properties when the material is subjected to fiber delamination conditions. Specific questions to be addressed: 1) Can damage be observed in the form of color or fluorescence in the area of delamination? 2) Is the mechanophore required to be covalently attached to the fiber and matrix or can frictional forces induce the desired mechanochemistry?

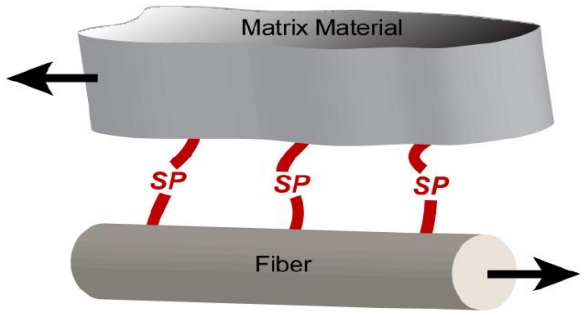

Figure 5.1 Graphical representation of a spiropyran mechanophore at the interface of a fiber and matrix in a fiber reinforced composite. Arrows indicate potential shear forces that are hypothesized to transmit to the mechanophore and give indication of delamination.

5.2 Compounds Investigated

Here we targeted coupling a carboxylic acid functionalized spriropyran with amine functionalized glass fibers. This coupling has shown to be a robust method for surface functionalization.[2] The putative mechanophore **17** and control **18** were synthesized by similar protocols outlined in Chapter 2. The structure of the compounds used for these investigations is given in Figure 5.2. As discussed in Chapter 2, carboxylic acid functionalized spiropyrans were synthesized to be amenable to surface immobilization.[3,4] Potential attachment points to the fiber and matrix were kept the same as mechanophores in homogenous polymer systems.

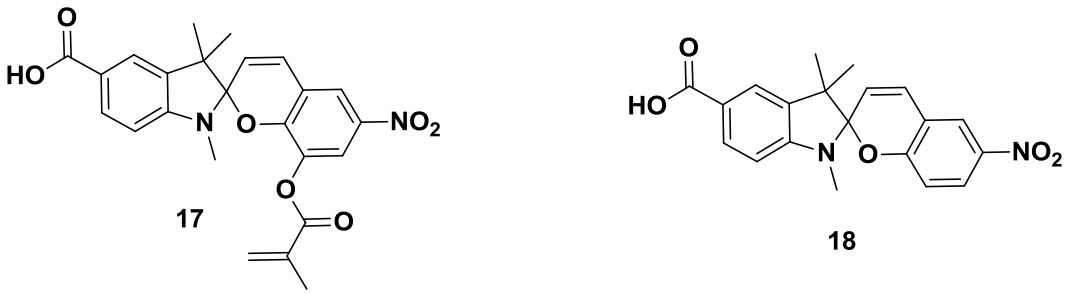

Figure 5.2. Structures of the spiropyrans used for surface-functionalization of glass fibers. Mechanophore 17 contains a methacrylate group for connection to a PMMA matrix with the control lacks this functionality.

Mechanophore **17** and control **18** were analyzed by UV-Vis spectroscopy in the open and closed states. Both compounds displayed photochromism with λ_{max} of 554nm (mechanophore) and 563nm (control) in ethanol (Figure 5.3) at identical concentrations. Additionally, the mechanophore shows a higher absorption than the control.

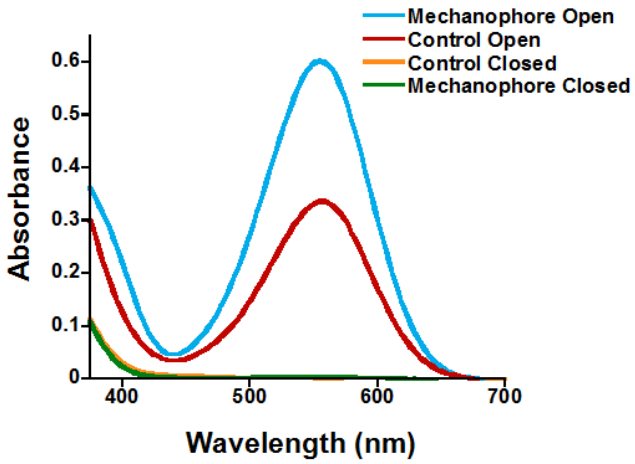

Figure 5.3 UV-Vis spectra of **17** and **18** in the open and closed states in ethanol at identical concentrations.

Measuring the rate of reversions can give a relative measure of the stability of the spiropyran and merocyanine forms for each compound. As shown in Figure 5.4, the mechanophore displays a much slower rate of reversion than the control. These measurements suggest the merocyanine form of the mechanophore is long-lived and therefore could potentially be useful as a damage sensing mechanophore in a composite. However, it also suggests that the merocyanine of the control is short-lived and may not be an adequate control compound as it is dissimilar to the mechanophore. For example, if the control compound is activated during solid state tests and fades from the merocyanine to the spiropyran on a time scale faster than our measurements, the ring-opening might not be observed. As will be discussed in the following sections, the exact opposite of this behavior was observed in the final composites.

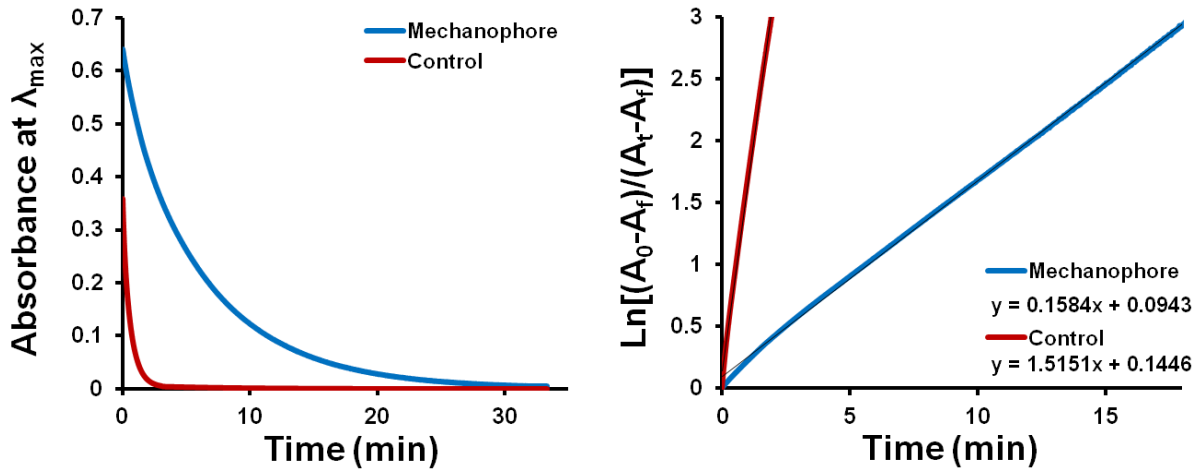

Figure 5.4. Thermal reversion of mechanophore and control compounds in EtOH at room temperatures

5.3 Composites

5.3.1 Surface Functionalization

Mechanophore and control spiropyrans were subjected to carbodiimide coupling conditions to attach them to glass fibers shown in Figure 5.5. Mechanophore **17** or control **18** was dissolved in tetrahydrofuran (THF) with ethylcarbodiimide hydrochloride (EDC). E-glass fibers, 16 μm in diameter (Owens Corning 158B-AA-675) with a proprietary aminopropylsilane (APS) sizing were functionalized with either spiropyran by stirring in the solution for 72 hours. Fibers were removed from the solution, rinsed with water and THF, soaked in THF for 4 hours, and rinsed again with THF and water to wash away unbound spiropyran to the fiber surface. Fibers were dried in a 35°C oven for 12 hours to remove remaining solvent.

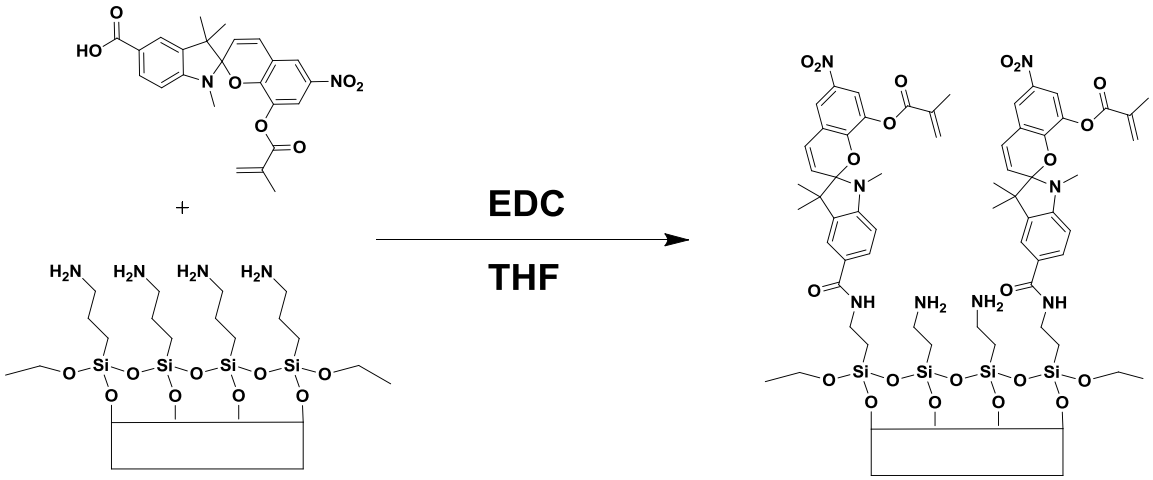

Figure 5.5. Surface functionalization of amino functionalized glass fibers with carboxylic acid functionalized spiropryans.

5.3.2 Composite Synthesis

Synthesis of the linear PMMA matrix was performed via a free radical polymerization initiated with benzoyl peroxide (BPO) and N,Ndimethylaniline (DMA). Methyl methacrylate (MMA) (1 mL, 9.39 mmol, 1 equiv.) and BPO (15 mg, 0.0619 mmol, 0.00662 equiv.) were combined in a scintillation vial, flushed with argon, and sealed with a septum. Ethyl phenylacetate (EPA) (0.4 mL, 2.51 mmol, 0.267 equiv.) was added to the solution to lengthen the working time during polymerization. Once the BPO was fully dissolved, DMA (6 μL, 0.0473 mmol, 0.00506 equiv.) was injected into the scintillation vial.

The two potential modes of force that could give rise to ring-opening of a spiropyran at the interface are a direct tensile stress that should stretch the mechanophore **17** by the fiber pulling away from the matrix. The second potential mode of activation could be a frictional force of the matrix interacting

with the fiber. Several types of samples were synthesized to understand the origin of spiropyran ring-opening at an interface and whether tensile stress is required (covalent attachment of the spiropyran to both the fiber and the matrix) or if frictional force is sufficient (covalent attachment of the spiropyran to the fiber but not the matrix).

The different types of samples are given in Table 5.1 will be described here. Type 1 samples contains the mechanophore 17 at the interface and covalently attached to the glass fiber through an amide bond and covalently attached to a PMMA matrix. Type 1 should be amenable to tensile stress and potentially frictional forces after delamination. Type 2 samples contain the mechanophore 17 covalently attached to the fiber through an amide bond. The matrix in type 2 samples is epoxy. Therefore, the spiropyran should not covalently attach to the epoxy matrix and should not be amenable to tensile stress. However, type 2 samples could be amenable to frictional forces. Type 3 samples contain the same components as type 1, but the synthetic steps were varied. First, the glass fiber was subjected to surface functionalization with the mechanophore 17, however, the reaction conditions lacked the carbodiimide needed to produce the amide bond. Any spiropyran on the surface might be due to an electrostatic attraction of the amine and the carboxylic acid. These samples were thoroughly washed the same as other types before adding the PMMA matrix. Type 3 samples were prepared to give indication if any spiropyran present on the surface of other types is due to an electrostatic interaction and not a covalent bond. If no spiropyran is present on the surface of the fibers, then type 3 samples, in principle, should not give rise to fluorescence. If any spiropyran remains on the surface after washing the fibers, these molecules could, in principle, attach to the PMMA matrix and be amenable to frictional forces. Type 4 samples contain no spiropyran. The amine functionalized fibers were directly treated with MMA to create a PMMA matrix around the unfunctionalized fiber. Type 4 samples should not exhibit fluorescence due to the lack of spiropyran. Type 5 samples contain the control **18** covalently attached to the surface of the fiber through an amide bond but should not be attached to the PMMA matrix as it lacks the functionality for covalent attachment to the matrix. Type 5 samples should not be amenable to tensile stresses but could be sensitive to frictional forces.

Table 5.1 Types of samples investigated with corresponding spiropyran, matrix, and attachment type.

Sample Type	Spiropyran	Polymer Matrix	Spiropyran Attachment
1	17	PMMA	Fiber and Matrix
2	17	Epoxy	Fiber
3	17	PMMA	Matrix
4	None	PMMA	N/A
5	18	PMMA	Fiber

Fibers used in each type of composite were tested for fluorescence prior matrix application. The fibers were kept in the dark and irradiated with UV light (365 nm) and their fluorescence spectra was recorded as shown in Figure 5.6. As expected, type 1 and 2 samples gave rise to similar fluorescence, indicating the presences of the spiropyran on the surface. These samples exhibit a broad peak centered around 590 nm .Type 3 samples gave no appreciable fluorescence indicating either no spiropryans on the surface due to electrostatic interactions or that any spiropyrans were removed from the surface during the washing procedure. Type 4 samples gave rise to minimal fluorescence as expected. Type 5 samples, which contain the control spiropyran, **18**, gave rise to a large intensity of fluorescence but with a dissimilar peak shape to types 1 and 2. The sharp peak is centered around 580 nm. This peak shape and blue shift can potentially be attributed to H-aggregate formation, an orderly plane-to-plane stacking of the spiropyran molecules.[5]

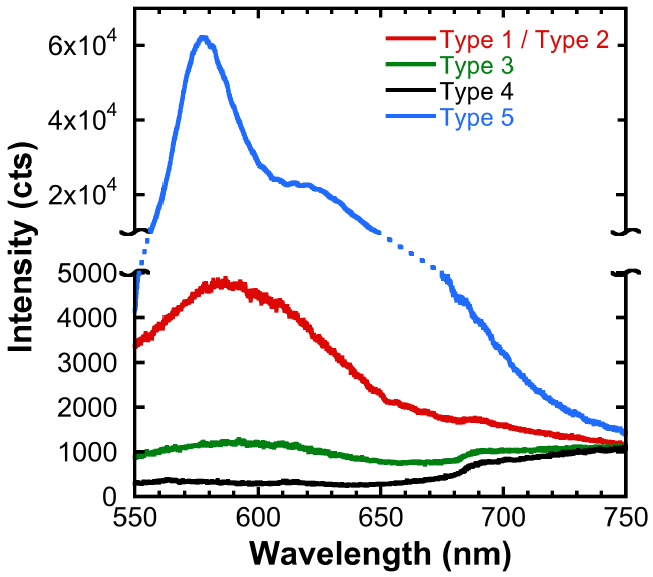

Figure 5.6 Fluorescence spectra of fibers of different types without matrix application.

5.4 Testing

Composite testing was conducted was tested as outlined by Kingsbury.[6] Here, the composites were subjected to fiber pullout tests where the matrix was held stationary and the fiber was pulled in tension (Fig 5.7). During testing the stress increased until interfacial debonding, at which point the stress decreased sharply. Fluorescence measurements were conducted *in-situ* by a Raman microscope.

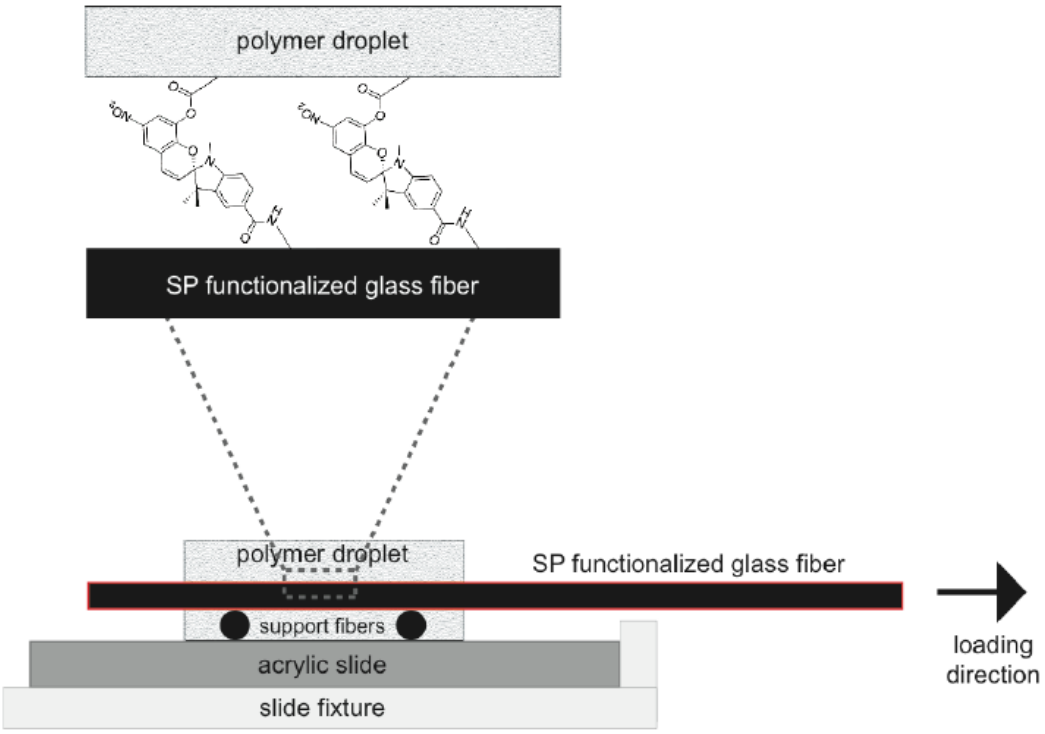

Figure 5.7. Side-view schematic of an active single fiber sample subjected to a pullout test.

The results of fiber pullout tests are shown in Figure 5.8. Type 1 samples exhibit a much higher fluorescence signal than types 2-4. The only difference between type 1 and 2 is the covalent attachment to the polymer matrix. According this comparison mechanophore 17 is amenable to activation at an interface only through tensile stress and not frictional forces. However, it is unknown the frictional forces generated by the epoxy is the same as PMMA. Comparison a Type 1 and Type 5 samples gave unexpected results. Both types give rise to fluorescence. However, the type 5 samples gave rise to a much higher fluorescence signal than type 1. There are several possibilities to account for these data. First, the concentration of spiropyran on the surface of the fibers is unknown. The higher signal could be due to a higher concentration of spiropyran on the surface in type 5 samples. Second, the spiropyrans, **17** and **18,** maybe too dissimilar electronically to compare. The UV-Vis absorption and fluorescence spectras gave a different λ_{max} for each compound, suggesting a slightly different electronic behavior. Perhaps the control **18**, should be functionalized with an acetate group at the 8 position instead of hydrogen to mimic the methacrylate group on **17** to make it closer to the mechanophore electronically. A third possibility is the ability of the compounds to align on the surface. The peak shape of the fluorescence spectrum of type 5 samples suggested a potential H-aggregate structure in the open form. It is possible that this type of

alignment is preferential and any frictional activation induces further spiropyran-to-merocyanine conversion to maintain the alignment.

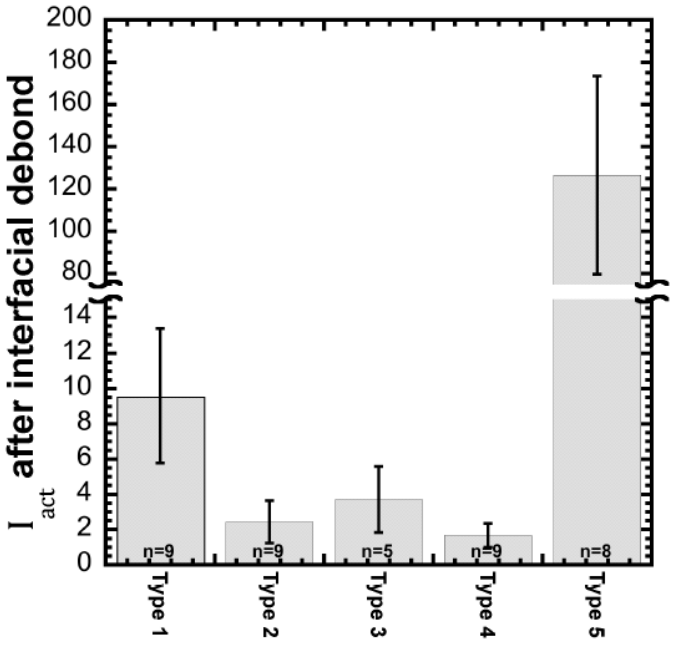

Figure 5.8 Average fluorescence intensity of each type of sample after interfacial debonding.

5.5 Conclusions

A putative spiropyran mechanophore and control were developed to test interfacial activation as a method for inducing mechanochemistry. Fibers were functionalized with spiropyrans and incorporated into a polymer composite in various configurations to understand activation at an interface. The results suggest that mechanophore **17** is required to be covalently attached to both the fiber and the matrix for activation to occur. However, activation of the control (type 5) samples indicated that frictional force can induce ring-opening. The uncertainties in the differences of the composites at the molecular level do not allow us to definitively conclude the origin of the fluorescence signals. Perhaps the control spiropyran needs to more closely resemble the putative mechanophore (**17**) in both structure and electronics. The control compound could conceivably contain an acetate group at the 8 position instead of a hydrogen. This acetate group could, potentially, more closely mimic the sterics and electronics of the methacrylate at the 8 position of the putative mechanophore **17**.

5.6 Detailed Procedures

The functionalized fiber was loaded in tension at 0.5 μμm/sec with a Physik Instrument M-230.10S linear actuator until interfacial debonding was achieved. Load was monitored using a Honeywell Sensotec (150 g) load cell. Load and displacement were collected and correlated using a LabView program. During interfacial testing, the load increased until complete interfacial debond, at which point the load dropped quickly before plateauing to a frictional load value. Crosshead displacement was determined directly from the linear actuator. *In situ* fluorescence spectra were collected during interfacial loading using a Horiba LabRAM HR Raman spectroscopy imaging system. An excitation beam of 532 nm was incident upon the sample, focused on the surface of the fiber embedded in the polymer matrix. Wavelengths of 550-750 nm were collected at regular intervals during interfacial loading and a shutter was used to block the excitation laser between spectra collection to minimize the effects of photobleaching. Figure 5.8 shows an image of a single fiber microbond specimen in the custom load frame on the stage of the Raman spectroscope.

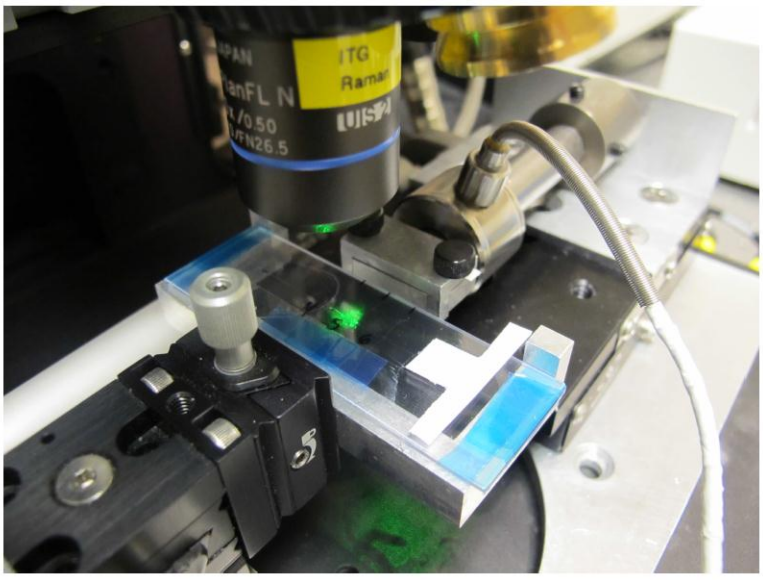

Figure 5.9 Single fiber microbond specimen in custom fixture under Raman spectroscope.

5.7 References

(1) Thortenson, E. T.; Chou, T-W. *Advanced Materials*, **2006**, *18*, 2837-2841.

(2) Rosario, R.; Gust, D.; Hayes, M.; Jahnke, F.; Springer, J.; Garcia, A. A. *Langmuir*, **2002**, *18*, 8062-8069.

(3) Gorelik, S.; Hongyan, S.; Lear, M. J.; Hobley, *J. Photochem.and Photobiol. Sci*. **2010**, *9*, 141-145.

(4) Rosario, R.; Gust, D.; Hayes, M.; Springer, J.; Garcia, A. A. *Langmuir* **2003**, *19*, 8801-8806.

(5) Rösch, U.; Yao, S.; Wortmann, R.; Wurthner, F. *Angew. Chem. Int. Ed*. **2006**, *45***,** 7026-7030.

(6) Kingsbury, C. Ph.D. dissertation. University of Illinois at Urbana-Champaign, **2012.**